

Modeling of Beam Down Solar Concentrator and Final Optical Element Design

By
Vikas Kumar

A Thesis Presented to the
Masdar Institute of Science and Technology
in Partial Fulfillment of the Requirements for the
Degree of
Master of Science
in
Mechanical Engineering

© 2015 Masdar Institute of Science and Technology

All rights reserved

Abstract

The Beam-Down Optical Experiment (BDOE) is a unique Concentrated Solar Power (CSP) pilot project currently operated by Masdar Institute and located at the Masdar Institute Solar Platform at 25.44204 N 54.61677 E in Abu Dhabi. The plant is a point focusing Fresnel system of 33 alt-az tracking heliostats which uses a second complement of fixed tower-mounted mirrors to redirect the solar radiation back down towards the ground, hence the name “Beam Down”. The benefits of this plant potentially include a more thermally efficient solar receiver located at ground level for easier operations and maintenance and decreased parasitic energy consumption and thermal and fluid pumping losses. To this end the Masdar Institute/MIT collaborative project Concentrated Solar Power on Demand Demonstration (CSPonD Demo), is developing a direct absorption molten salt solar receiver combined to the thermal energy storage system. This thesis was part of this project. The main objective of the thesis was the investigation of a final optical element (FOE) design that, coupled with the BDOE, provides high concentration and optical efficiency for the CSPonD and various other types of receiver. The first step in FOE design is developing an accurate, flexible, and well documented model of existing BDOE optics. A Monte Carlo ray-tracing model of the BDOE has been developed using a structured model configured, where appropriate, with the aid of scripts that produce Scheme descriptions of optical components in precise locations and orientations. Optical losses by cosine factor, blocking, shading, central reflector spillage and absorption and optical imperfections of the heliostat and central reflector facets are characterized. It is shown that for a molten

salt direct absorption receiver a conical final optical element (FOE) is slightly better than a compound parabolic concentrator and that a faceted cone is almost as good. The reasons for these unexpected result are:

- 1) The optical configuration of the Masdar BDOE provides a nearly radial and somewhat converging angular distribution at the FOE inlet.
- 2) Better angular distribution incident on the molten salt surface (FOE outlet), and also a uniform distribution at the outlet of the cone.

The property of uniform FOE outlet flux helps to prevent hot spots that can cause molten salt degradation.

CPC and conical surfaces are reasonable but not necessarily optimal profile choices for the FOE design. A near optimal profile-of-revolution FOE that is better than either the CPC or the cone is developed for the MI-MIT's CSPonD Demo molten salt receiver.

This research was supported by the Government of Abu Dhabi to help fulfill the vision of the late President Sheikh Zayed Bin Sultan Al Nahyan for sustainable development and empowerment of the UAE and humankind.

Acknowledgments

I would like to thank my research advisor Dr. Peter Armstrong for accepting me as his student. I wish to thank him sincerely for his support, guidance and for correction of the thesis.

I am grateful to Dr. Nicolas Calvet, who has encouraged and given me the opportunity to work in his project CSPonD Demo.

I would like to thank Dr. Benjamin Grange for his insightful comments, and fruitful discussions.

I would like to thank Marwan Mokhtar whose previous master thesis has inspired my current work. I would like to extend my gratitude to Dr. Marco Stefancich, and Dr. Matteo Chiesa, because of their previous collaboration with Dr. Peter Armstrong in LENS group lay the foundation of my master's thesis.

Special thanks to Alberto, Azhar, Pairoj, Miguel, and Saad for making my stay in Masdar Institute especially unforgettable, thank you for everything.

Vikas Kumar,

Masdar City, May 28 2015

Contents

Abstract	iii
Contents	vii
List of Tables	ix
List of Figures	x
Nomenclature	xiv
Abbreviations	xvi
1. Introduction	1
1.1. Motivation	1
1.2. Problem Definition and Objectives	3
1.3. Description of the Beam Down Concentrator	4
1.3.1. Heliostats	4
1.3.2. Central Reflector	8
2. Beam Down Geometrical Model	11
2.1. TracePro	11
2.1.1. Geometry of the element	12
2.1.2. Optical property	13
2.1.3. Source definition	13
2.2. Beam Down Model Definition	18
2.2.1. Basic definition	18
2.2.2. Creating Scheme macro file (.scm) using Matlab	26
2.3. Problem Decomposition using ray vector file	29
2.4. Results of BDOE Ray Trace Analysis	30
2.4.1. Evolution of flux at different elevations	30
2.4.2. Central ray convergence plane at different heights (6, 7 & 8 m)	35
2.4.3. Optical efficiency	37
3. Final Optical Element	45
3.1. Final Optical Element	45

3.2. CPC	46
3.3. CONE.....	49
3.4. Results	50
3.4.1. CPC.....	50
3.4.2. CONE.....	52
3.4.3. CSPonD's FOE	53
3.5. Summary	56
4. Generalized Shape Optimization	63
4.1. Methodology	65
4.2. Optimization of cone (CSPonD)	66
5. Conclusion And Future Work.....	68
5.1. Conclusion.....	68
5.2. Future Work	69
Appendix A: Canting Angle	72
Appendix B: Canting Error.....	80
Appendix C: Reflectivity Measurements and Models	84
Appendix D: Raytrace-number of rays	91
Appendix E: Thermal Loss Model.....	95
Bibliography	98

List of Tables

Table 1. Geometry of 100kW pilot plant as built for $Z_{CRC} = 2$ m	24
Table 2 Recommended Average Days for Months and Values of n by Months[24]...	41
Table 3 DNI, Azimuth and Zenith with respect to Solar time	50
Table 4. CPC output flux (kW).....	51
Table 5. Net useful flux (kW).....	51
Table 6 Cone output flux (kW).....	53
Table 7. Flux (kW) entering molten salt (CPC).....	54
Table 8. Flux (kW) entering molten salt (cone).....	54
Table 9 Flux entering molten salt/output of CPC	55
Table 10 Flux entering molten salt/output of cone	55
Table 11. Net useful flux (kW) entering molten salt (CPC).....	56
Table 12. Net useful flux (kW) entering molten salt (cone).....	56
Table 13. Optimized CPC vs Cone	57
Table 14 Optimized cone vs 6 Faceted cone optical perfomance.....	60
Table 15. Cone optimization for CSPonD receiver with $Z_{CRC} = 6000\text{mm}$ and outlet radius = 350mm.	67
Table 16. Canting angle (degree) of A, B and C type HS	74
Table 17 Mean , standard deviation and Median of canting error	83
Table 18 Summary of HS and CR reflectivity	84
Table 19. Measured reflectivity of CR; each value is average of the five points shown in Figure 66.	84
Table 20. Reflectivity of HS at two incidence angles.....	86

List of Figures

Figure 1 Beam Down system concept with Final Optical Element depicted at utility scale	4
Figure 2. Layout of the BDOE heliostats field.	5
Figure 3. Heliostat facet and bank sizes [17]	6
Figure 4 Basis of ganged 3-bank heliostat design [17].....	7
Figure 5. Heliostat inclination angle (on axis canting)	8
Figure 6. Central reflector top view	9
Figure 7. Central reflector facet canting angle.....	10
Figure 8. TracePro's insert menu, promitive solid dialog box (thin sheet)	12
Figure 9. Grid Source example, grid steup	15
Figure 10. Grid Source example, beam setup	16
Figure 11. Grid Source example, polarization	16
Figure 12. Grid Source example ,wavelength.....	17
Figure 13. Heliostat layout.....	19
Figure 14. TracePro objects representing BDOE HS field and CR platform (top view)	20
Figure 15. TracePro heliostat reference geometry	22
Figure 16 Central reflector canting trigonometry	23
Figure 17. Central rays with CR canting adjusted for Central Ray Convergence heights of 0, 2 and 3 m above original target.	25
Figure 18. Beam Down TracePro model showing ray data plane at 10m	30
Figure 19. Beam down TracePro model with (virtual) flux mapping planes at different heights	31
Figure 20 Flux distribution in plane at 6 m height while BDOE central ray convergence point (CR canting) is at 6-m height.....	31

Figure 21 Flux distribution in plane at 6.5m height while BDOE central ray convergence point (CR canting) is at 6 m height.....	32
Figure 22 Flux distribution in plane at 7m height while BDOE central ray convergence point (CR canting) is at 6m height	32
Figure 23 Flux distribution in plane at 7.5m height while BDOE central ray convergence point (CR canting) is at 6m height	33
Figure 24 Flux distribution in plane at 8m height while BDOE central ray convergence point (CR canting) is at 6m height	33
Figure 25. Flux distribution in plane at 10 m height while BDOE central ray convergence point (CR canting) is at 6m height	34
Figure 26. Irradiance map, normalized with respect to peak irradiance in the central ray convergence plane at 5m.....	35
Figure 27 Paths of central ray reflecting from control mirror facet centers	35
Figure 28 Flux distribution in plane at 6 m height while CRC point Z_{CRC} (CR canting) is set to 6 m height.	36
Figure 29 Flux distribution in plane at 7 m height while CRC point Z_{CRC} (CR canting) is set to 7 m height.	36
Figure 30 Flux distribution in plane at 8 m height while CRC point Z_{CRC} (CR canting) is set to 8 m height.	37
Figure 31 Blocking analysis plane	39
Figure 32 Illustration of blocking	39
Figure 33 BDOE's cosine, shading, blocking, spillage efficiency of CR and HS reflectance vs zenith angle	40
Figure 34 Shading Efficiency throughout the year on monthly average day	41
Figure 35 Zenith angle vs Solar time throughout the year on monthly average day ...	42
Figure 36 Azimuth angle vs Solar time throughout the year on monthly average day	42
Figure 37 Surface plot of shading efficiency with respect to Zenith and Azimuth	43
Figure 38 Surface plot of spillage efficiency with respect to Zenith and Azimuth	43
Figure 39 Optical overall efficiency until CR vs zenith and azimuth.....	44
Figure 40. Net power collected as a function of receiver radius. Total incident flux and thermal loss are also shown.	46
Figure 41. Characteristic transmission efficiency 2D and 3D CPC.....	47
Figure 42. Construction of ideal 3D-CPC [34].....	48
Figure 43. TracePro insert menu, reflector dialog box showing CPC parameters	49

Figure 44. Scheme of cone and CPC showing entrance diameter, d_1 , exit diameter d_2 , half acceptance angle and axial length.....	50
Figure 45 Angles of incidence and refraction in media [24]	53
Figure 46 (a) CPC (b) cone output flux distribution at 12pm.....	58
Figure 47 (a) CPC (b) cone output flux distribution at 10 AM	59
Figure 48 Cone (left) and 6 faceted cone (right) Inlet Flux at 12 pm.....	61
Figure 49 Cone (left) and 6 faceted cone (right) Output Flux at 12 pm	61
Figure 50 Cone (left) and 6 faceted cone (right) Inlet Flux at 10 am	62
Figure 51 Cone (left) and 6 faceted cone (right) Output Flux at 10 am.	62
Figure 52 Common feature of FOE Element.....	64
Figure 53. TracePro 2D interactive optimizer general setup	66
Figure 54 CSPonD demo final FOE assembly design and manufactured FOE.....	69
Figure 55 Identification of heliostat facets.	73
Figure 56 Frame mounting angle (shaft tilt)	75
Figure 57 Flux intercept at CRC plane	75
Figure 58 CRC plane flux distribution at 12pm (June) with no shaft tilt.	76
Figure 59 CRC plane flux distribution at 12pm (June) with shaft tilt	77
Figure 60 CRC plane flux distribution at 10 AM (June) with no shaft tilt.....	78
Figure 61 CRC plane flux distribution at 10 AM (June) with shaft tilt.....	79
Figure 62. Heliostat A1 facet tilt measurement (handwritten numbers) along with required values	81
Figure 63. Close-up of left top corner in Figure 62	82
Figure 64 Cumulative distribution of canting error values in degrees N=1419	83
Figure 65. Central reflector identification numbers. Non-integer facets are the inactive facets for which there is currently no heliostat	86
Figure 66. CR facet reflectance measurement positions.....	86
Figure 67 HS mirror Incident angle of BDOE for entire year (N = 221364)	88
Figure 68 HS and CR mirror reflectnace defination example	88
Figure 69 TracePro response to HSmirror reflectivity property	89
Figure 70 SCHOTT B270 optical prperty	89
Figure 71 back silver reflectivity example.....	90
Figure 72 Reflectivity response in Tracepro of Schott B270 + back silver 95%	90
Figure 73 Flux distribution in target plane at 6m height with full BDOE (3 million rays)	92

Figure 74 Flux distribution in target plane at 6m height with full BDOE (12 million rays).....	93
Figure 75 Flux distribution in target plane at 6m height with full BDOE (27 million rays).....	94

Nomenclature

A	Area of receiver aperture	m^2
d_1	Inlet diameter of FOE	mm
d_2	Outlet diameter of FOE	mm
Gr	Grashof number	
h_c	Convection heat transfer coefficient	$\text{W m}^{-2} \text{K}^{-1}$
h_{rec}	Receiver height	mm
h_{HS}	Heliostat control mirror elevation at reference position	mm
h_r	Linearized radiation heat transfer coefficient	$\text{W m}^{-2} \text{K}^{-1}$
k	Thermal conductivity	W m K^{-1}
L	Characteristics length	m
Nu	Nusselt number	
n_m	Refractive index of medium $m = 1$ or $m = 2$	
$\hat{n}_{k,i}$	Unit normal of each facet, $k = 1:33, i = 1:43$	
Pr	Prandtl number	
\dot{Q}_u	Net useful power output of the receiver	W
$\dot{Q}_{\text{incident}}$	Incident solar power on the receiver aperture	W
Re	Reynolds number	
$R_y(\theta)$	Counterclockwise rotation matrix around the y-axis	
$R_z(\theta)$	Counterclockwise rotation matrix around the z-axis	
\hat{s}	Unit Sun position vector	
\hat{r}_k	Unit reflected vector	

T_{pm}	Mean plate temperature	K
T_{sky}	Effective sky temperature	K
U_L	Overall heat loss coefficient	$\text{W m}^{-2} \text{K}^{-1}$
u_e	Wind speed	m s^{-1}
Z_{CRC}	Elevation of Central Ray Convergence point	mm
ϵ	Emissivity	
σ	Stefan-Boltzmann constant	$5.6704 \times 10^{-8} \text{ W m}^{-2} \text{ K}^{-4}$
ϕ	Solar azimuth angle	rad
ν	Kinematic viscosity	$\text{m}^2 \text{ s}^{-1}$
θ_{azi}	Azimuth angle of the heliostat	rad
θ_{ele}	Elevation angle of the heliostat	rad

Abbreviations

Titech	Tokyo Institute of Technology
MES	Mitsui Engineering and Shipbuilding
BDOE	Beam-Down Optical Experiment
HS	Heliostat
CR	Central Reflector
CSP	Concentrated Solar Power
CSPonD	Concentrated Solar Power on demand
FOE	Final Optical Element
DNI	Direct Normal Irradiation
LEC	Levelized Energy Cost
MPT	Mean Plate Temperature
Wspd	Wind Speed
Stdev	Standard Deviation
CRC	Central Ray Convergence

CHAPTER 1

Introduction

1.1. Motivation

Solar energy is by far the most abundant source of energy on Earth. However, the terrestrial average solar flux is low, non-uniform and intermittent. Its potential is best exploited in areas with relatively high and uninterrupted insolation. The UAE lies in what is known as the "sun-belt", the middle region of the globe that is most exposed to the sun. To reach Abu Dhabi's goal of getting 7% of its electricity from renewable resources by 2020 [1], solar power is therefore a reasonable option.

Solar energy is energy produced by the Sun in the form of heat and light. It can be harnessed using mainly solar thermal and photovoltaic technologies.

Concentrating solar power (CSP) systems use combinations of mirrors or lenses to concentrate direct beam solar radiation in order to reach high temperature heat in a system with low thermal losses (i.e. high thermal efficiency). High temperature leads to more efficient forms of useful energy for conversion of heat to electricity or fuels by various technologies. The term 'concentrating solar power' is often used synonymously

with ‘concentrating solar thermal power’. CSP has emerged as a competitive technology with respect to conventional power technologies. Unlike photovoltaic solar technologies, CSP offers the possibility of supplying reliable dispatchable power through integration of relatively inexpensive thermal storage systems [2][3], or through hybrid operation with existing or purpose-built fossil-fueled plants, therefore, offering firm generation capacity suitable for peak or even base load operation [1].

Electricity generation from CSP installations increased from 436 MW to 3,425 MW from 2008 to 2013. Major contributors to this capacity are Spain and USA.

Shams 1, located in UAE, is among world’s largest concentrated solar power plants and the first of its kind in the Middle East. It is a joint project between Masdar (60%), Total (20%), and Abengoa Solar (20%). Shams 1 was first operated at its nameplate capacity of 100 MW in first quarter of 2013 [4].

Although central tower technology is less established than parabolic trough technology, its can operate at higher energy conversion efficiency and consequently lower leveled cost of electricity (LCOE) are expected [1]. Central tower technologies’ uncertainties in cost, performance and technical risk are mainly due to the lack of commercial central receiver project experience [5]. GemaSolar owned by Torresol Energy (60%) Sener and (40%) Masdar, was the first commercial molten salt power tower. The largest commercial tower plant is Ivanpah Solar Power Facility (377 MW net) in USA which was completed in 2014 [6].

Commercialization of tower technology clearly helps in cost reduction and lowering project risks, however, it is expected that 48% of the cost reduction in tower plants will come from research and development [5]. Therefore there is a need of accelerated advances in areas such as CSP optics, heliostat construction, high temperature

receivers, conversion cycles, solar fuels, storage systems, heat transfer fluids, heat rejection technologies, flux measurement, resource assessments, etc. It is therefore essential to build up the necessary R&D infrastructure and develop our expertise in the field, to be able to address local and global technology problems facing the development and implementation of CSP [7].

1.2. Problem Definition and Objectives

The Masdar Beam-Down Optical Experiment (BDOE) was proposed and designed by Tokyo Institute of Technology (Titech). Titech led the consortium (Cosmo Oil, Mitsui Engineering and Shipbuilding (MES), Konica-Minolta) in charge of building the pilot plant. The main objectives of this project were to test several design concepts that can reduce overall cost of this type of CSP system, verify a numerical code (TSUBAME-sol) developed by Titech and ultimately investigate the feasibility of scaling a beam down CSP plant to significantly higher capacities (20 MW) [8]. Ganged-type heliostats, central reflector design and beam down optics are the main differences from conventional CSP tower designs [9] [10] [11].

Now (since late 2012) the BDOE is operated by Masdar Institute and used for research and development of CSP components and TES systems. To better understand its performance, an optical model is needed which can predict its output in conjunction with different kinds of receivers. For example, the CSPond Demo [12] will use a single-tank molten salt thermal energy storage arrangement which also acts as a direct volumetric receiver. An optical model is needed to estimate the input flux and find an optimal optical design for this kind of receiver.

A more general objective is the investigation of final optical element (FOE) designs that, coupled with the BDOE as shown in Figure 1, can provide high concentration and optical efficiency for various types of receivers [13][14][15]. The first step in FOE

design is developing an accurate, flexible, and well documented model of existing BDOE optics.

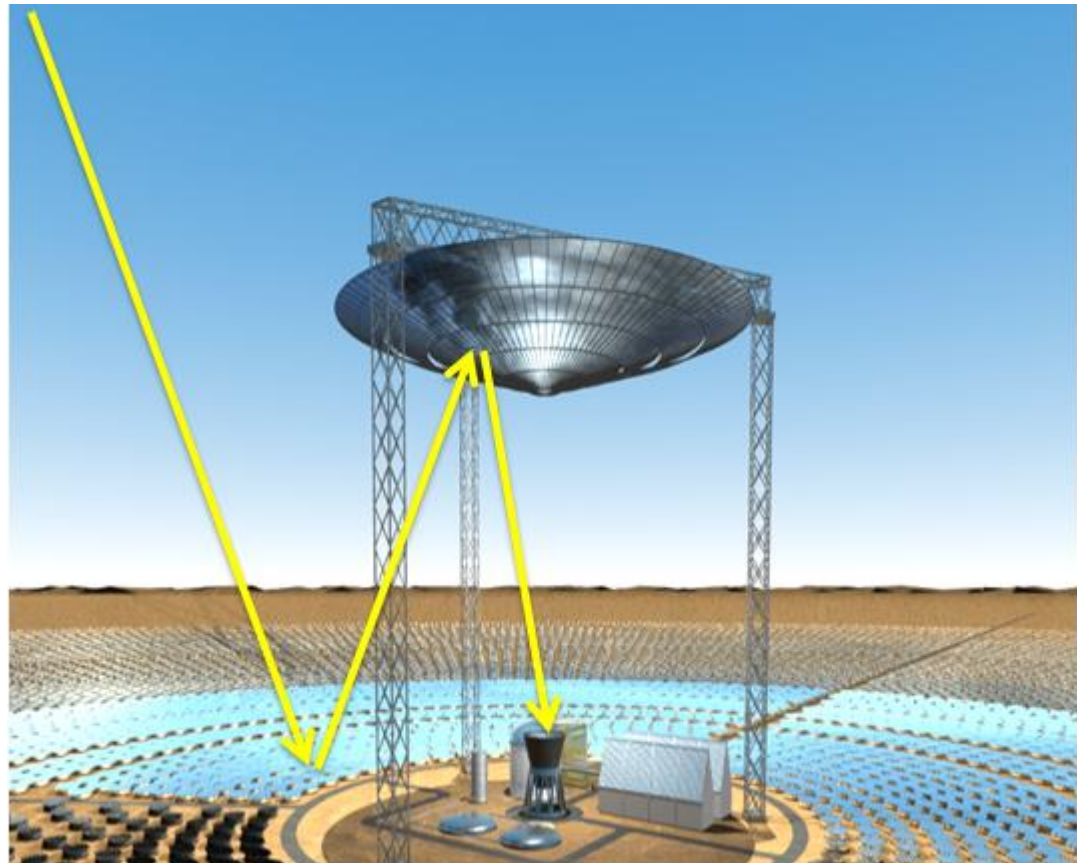


Figure 1 Beam Down system concept with Final Optical Element depicted at utility scale

1.3. Description of the Beam Down Concentrator

1.3.1. Heliostats

Heliostats layout

According to “Optical design of 100 kW pilot plant” TiTech report, the main purpose of building the small scale 100 kW (thermal output) plant was to verify TSUBAME-sol, a general purpose solar ray concentration simulator, which was applied for beam down systems with multi-ring reflector as well as tower top systems [8]. The 100 kW plant was required to be designed so that enough data for designing 20-200 MW commercial plants and Beam Down multi-tower systems could be obtained [16].

Therefore, the heliostat configuration of the 100kW BDOE had the following requirements:

- I. To verify the variation in heliostat performance over a wide range of radial positions, it was required to allocate the heliostats in all sides around the center.
- II. The heliostats were arranged at different distances from center (in rings A, B and C) to verify variation in heliostat performance.

The layout comprises three concentric circles having ratio of radii of 2:3:4 approximately. There are 33 heliostat (Figure 2) and these are uniformly distributed in every direction, except where the structural columns of the BDOE would block the reflected radiation.

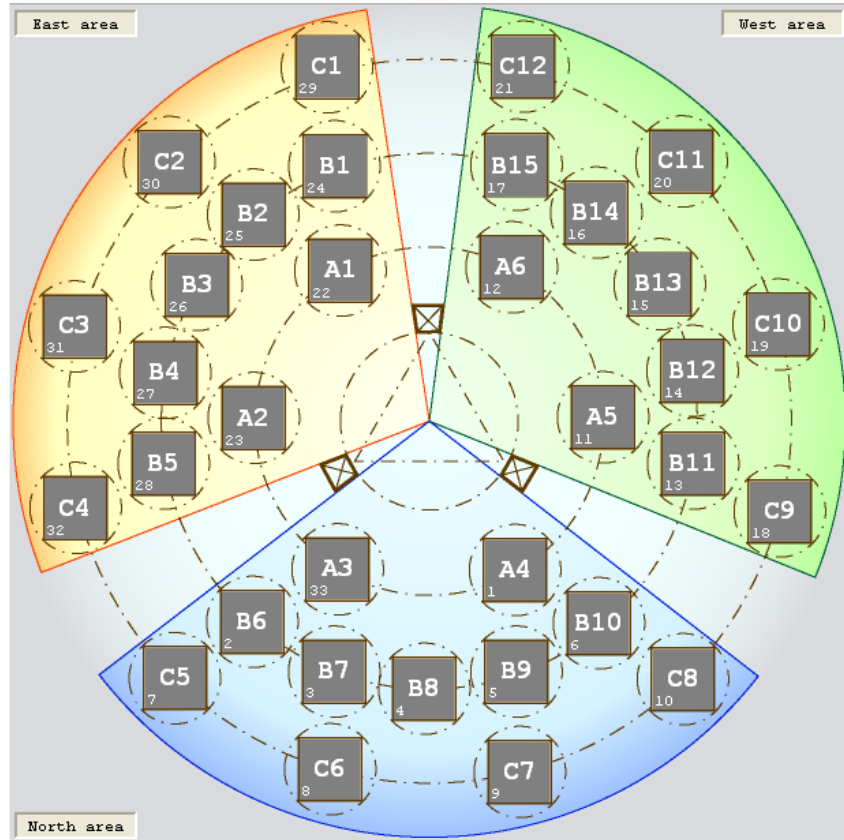


Figure 2. Layout of the BDOE heliostats field.

Heliostat Size

In the beam down concentration system, a heliostat facet size of 0.45 m x 0.45 m was chosen to have a feasible and effective concentration system at small scale. There are 7 columns in facet array of the heliostat (HS), hence width is 0.45 m x 7=3.15 m. There are 6 rows in facet array i.e. total $6 \times 7 = 42$ facet mirrors in one heliostat (Figure 3). The total mirror area becomes $0.45 \text{ m} \times 0.45 \text{ m} \times 42 \times 33 = 280.665 \text{ m}^2$.

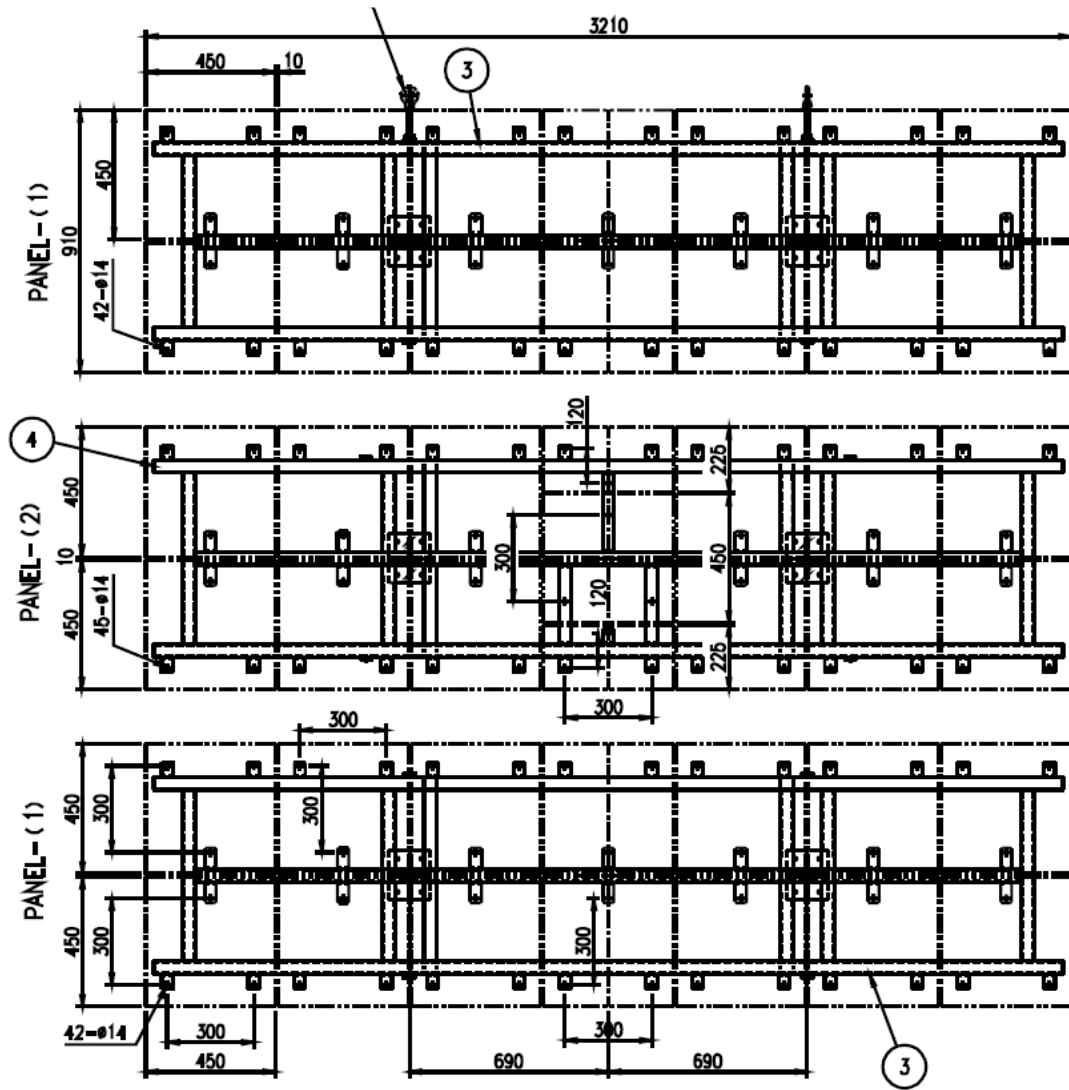


Figure 3. Heliostat facet and bank sizes [17]

Basis of heliostat design

Each HS has three banks (panels). Each bank has 14 facet mirrors arranged in 2 rows and 7 columns. When tracking the azimuth of the sun, banks are rotated around azimuth tracking axis. When tracking elevation of the sun each bank rotates about its own horizontal shaft, using just one motor (ganged type feature) by linking the three shafts as shown in Figure 4 [18].

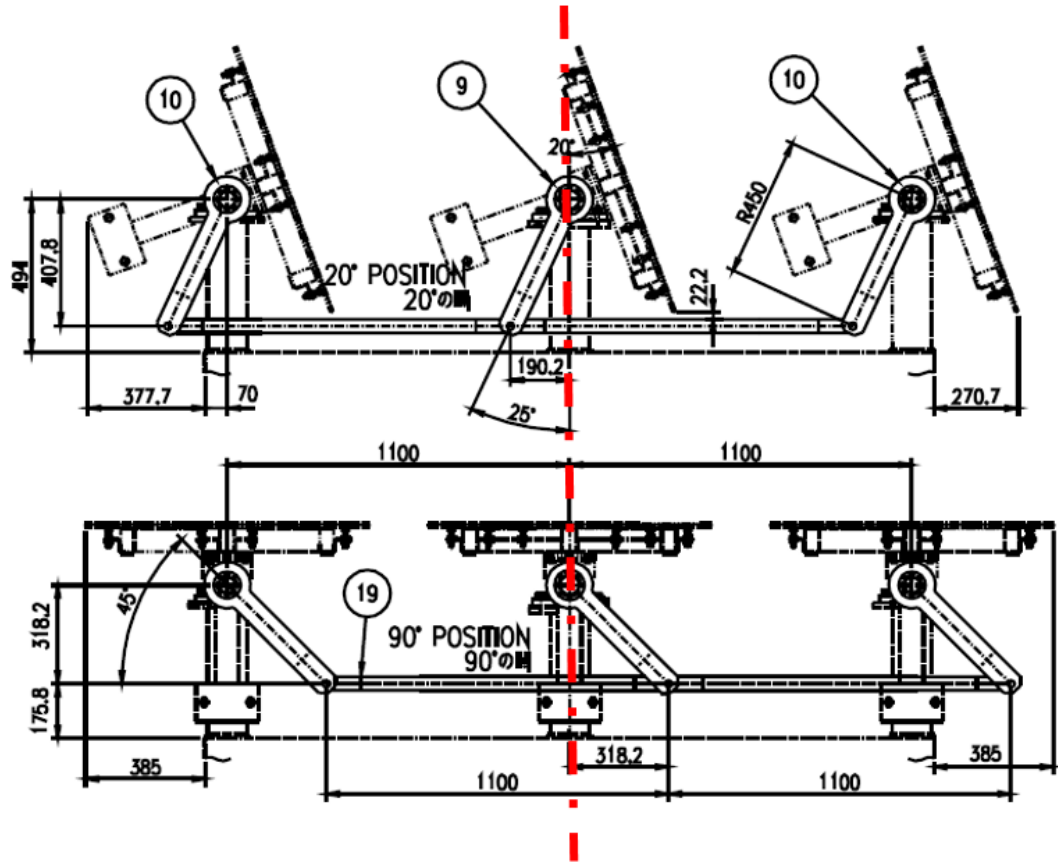


Figure 4 Basis of ganged 3-bank heliostat design [17]

Inclination angle of facet mirrors

The each facet of the heliostat has an inclination or canting angle. The normal lines drawn through the centers of each facet meet at one point “A”. The distance from a heliostat to the point “A” is set as twice of the distance from the heliostat to the upper focus (Figure 5). By doing this, the solar rays would reach the highest concentration, approximately at the upper focus, this is called on axis canting [19].

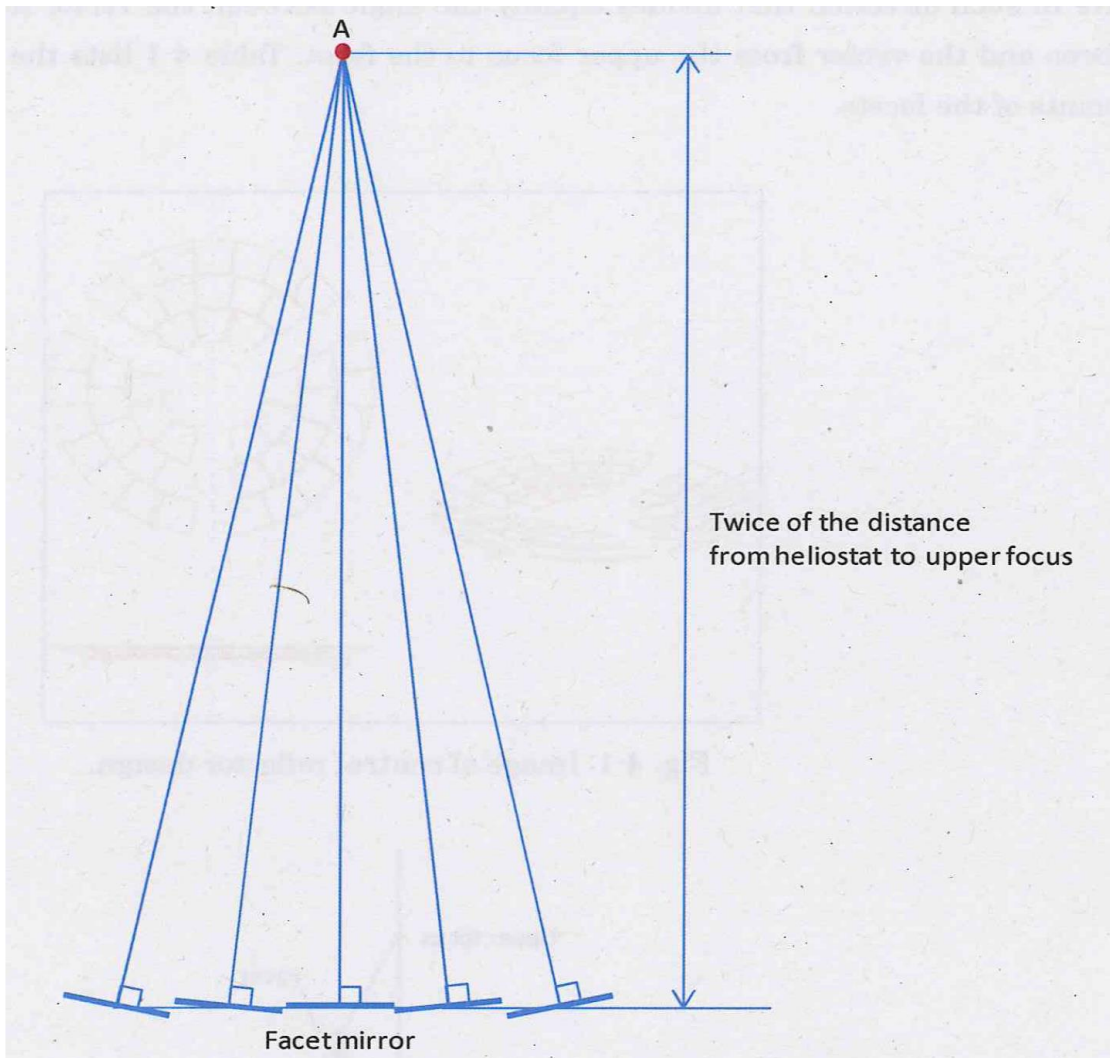


Figure 5. Heliostat inclination angle (on axis canting)

1.3.2. Central Reflector

Design of Central Reflector

The BDOE has a multi-ring type of faceted central reflector (CR) as Figure 6 shows. Each ring is composed of several facets and each facet mirror accepts most of the light reflected from one heliostat. Since there is one CR facet per heliostat the three-ring arrangement of heliostats is echoed in a three-ring arrangement of the CR facets.

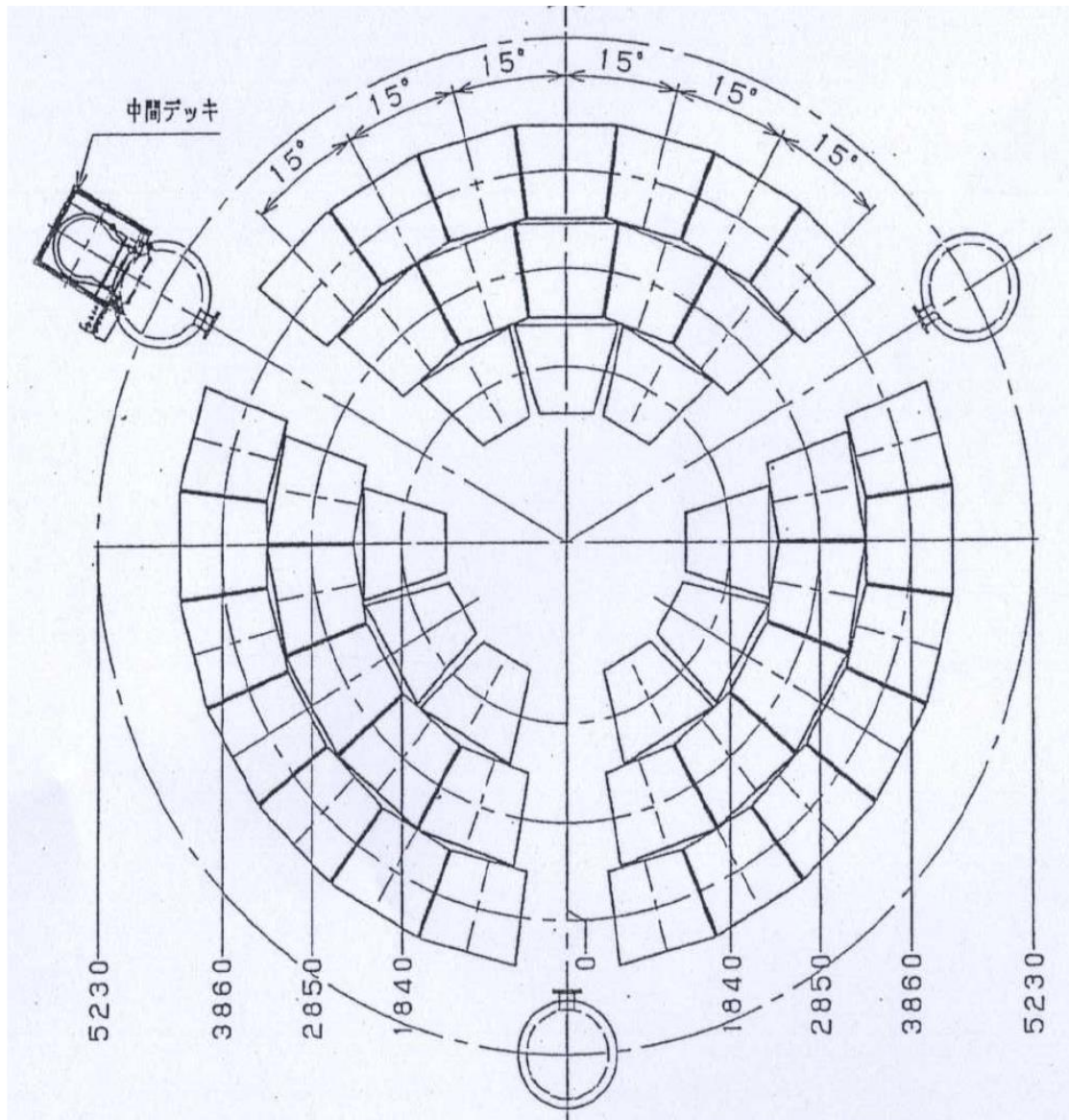


Figure 6. Central reflector top view

All the normal vectors of the CR facets are in a direction that divides the angle equally between the vector from facet to central ray convergence point (defined in Figure 7) and the vector from the upper focus which passes through the CR facet in question and continues downward to the corresponding HS central facet.

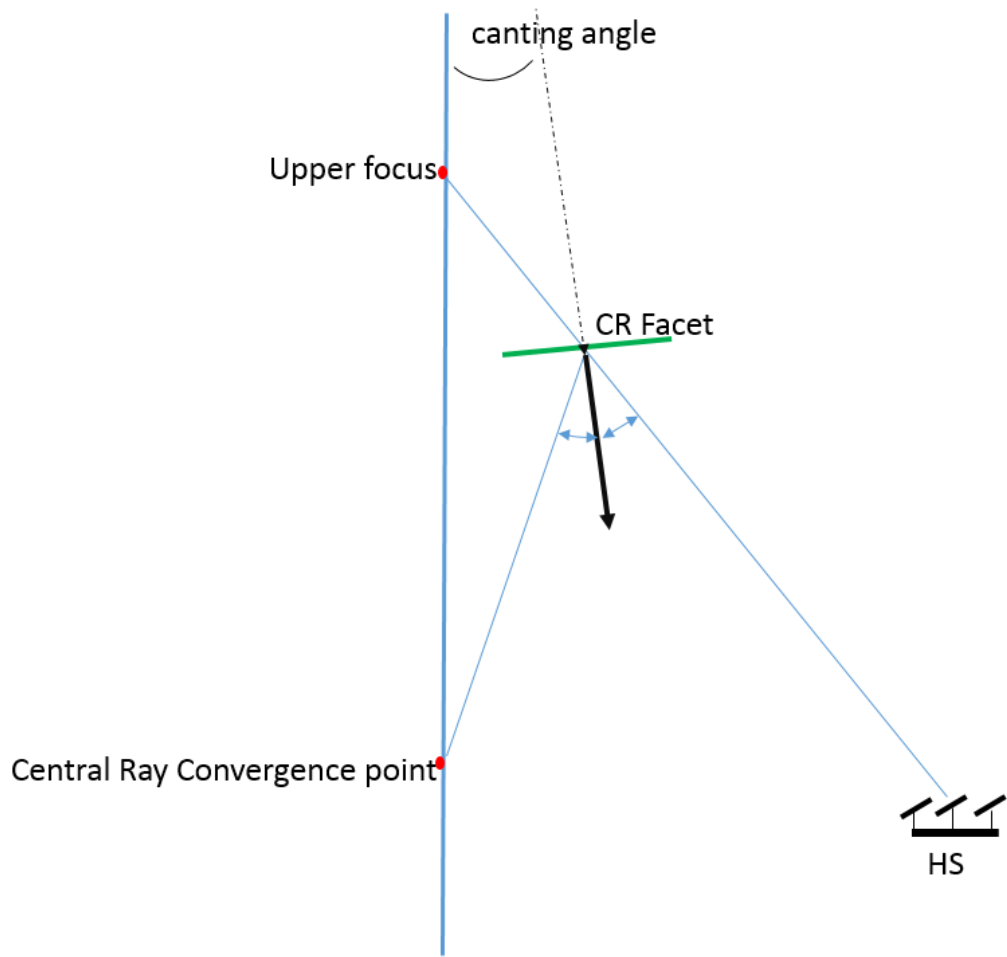


Figure 7. Central reflector facet canting angle

CHAPTER 2

Beam Down Geometrical Model

2.1. TracePro

TracePro is a ray tracing program for optical analysis of solid models first developed under a NASA SBIR contract [20]. TracePro traces rays using “Generalized Ray Tracing”. This technique allows us to launch rays into a model without making any assumptions as to the order in which objects and surfaces will be intersected. At each intersection, individual rays can be subject to absorption, reflection, refraction, diffraction and scatter [21].

As the rays propagate along different paths throughout the solid model, TracePro keeps track of the optical flux associated with each ray.

TracePro has built-in interfaces for compound parabolic concentrator (CPC) and cone objects which are absent from many solar ray tracing software packages [22]. TracePro includes the Scheme programming language [21], a flexible macro language for

manipulating views, editing geometry, and writing macro programs, including looping and branching.

Scheme, is a dialect of the LISP language developed at MIT [21][23]. LISP is used most often for artificial intelligence applications. An advantage of the Scheme language for software developers is easy extensibility. TracePro is designed so that everything that can be done in TracePro's interactive user interface can be done through a Scheme command or macro. Scheme code produced by TracePro's interactive user interface can be examined and modified by the user.

2.1.1. Geometry of the element

Heliostats are made of regular shaped facets, each represented in TracePro as a primitive solid – a thin sheet which is defined using vertices in 3D coordinates (X, Y, Z). The vertex positions are closed and connected by edges. This closed polygon is covered with a surface and made double sided.

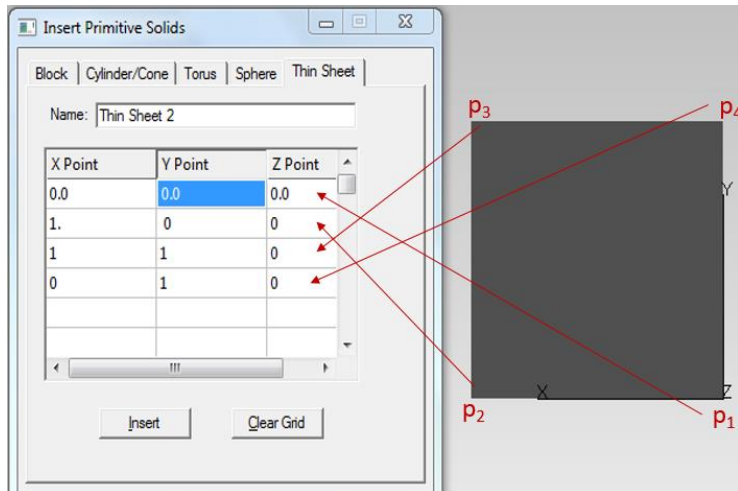


Figure 8. TracePro's insert menu, primitive solid dialog box (thin sheet)

The central reflector mirrors are defined in like manner, but with the geometrical difference of their being trapezoidal, while the HS facets are square or rectangular.

2.1.2. Optical property

Reflectivity of Heliostat and Central Reflector facets, measured and documented by TiTech, are tabulated in Appendix C. HS facets are flat float glass which has very small slope error compared to the facet canting errors documented in Appendix B.

In general reflection of radiation will change with respect to incident angle according to the Fresnel equation (as confirmed by measurements presented in Appendix C) [24]. For the optical simulation results presented in this thesis reflectivity values of 95% and 80% are assumed for the CR and HS mirror respectively.¹

When using a CPC/cone in conjunction with a molten salt receiver there will be reflection loss where the rays enter the salt. To account for this effect refractive index of bulk material must be defined. Molten salt refractive index is 1.42 [21].

2.1.3. Source definition

There are three basic methods in TracePro of generating rays: Grid Source, File Source and Surface Source.

Grid Source is defined as a virtual window to a distant source with parallel rays emanating as if from a window. For a Grid Source, the number of rays and irradiance to be traced should be specified. TracePro launches a grid of rays from this imaginary plane. The Grid parameters establish the size, pattern (circular, rectangular, etc.) and location of the grid. One can think of the grid as a sampling of rays from an infinitely distant source where all rays are collimated or parallel to each other.

¹ Reflectivity could be defined as function of incident angle in TracePro as described in Appendix C.

For example Figure 9 to Figure 12 shown below, show how different properties of a Grid setup are defined in TracePro.

- Grid boundary: “outer radius” of source is 30 m;
- Grid pattern: circular pattern is used, with $n = 1000$ rings, ‘rings’ specify the number of rays being traced, $N = 3 * n * (n - 1) + 1$ (i.e. 2997001 rays), Radiometric units are being used, with 1000 W/m² Irradiance;
- Grid position and orientation: Source is located at $z = 20\text{ m}$, with a specified e.g. normal vector [0.018 0.006 -0.9998], which was calculated using sun position algorithm[25], and up vector [0 1 0] [21].²

² TracePro uses a three-dimensional coordinate system with a global origin and X, Y, Z vectors to indicate directions. Often a plane must be defined to establish how the model will be viewed or how data will be displayed. The orientation of this plane is defined in terms of two direction vectors, the Normal and Up vectors.

The Normal vector is simply the direction Normal to the plane. We can think of planes as our computer screen or a piece of paper in a book laid out flat on a table. The direction perpendicular to the screen or paper is the normal vector.

The Up vector is used to reference the Y direction.

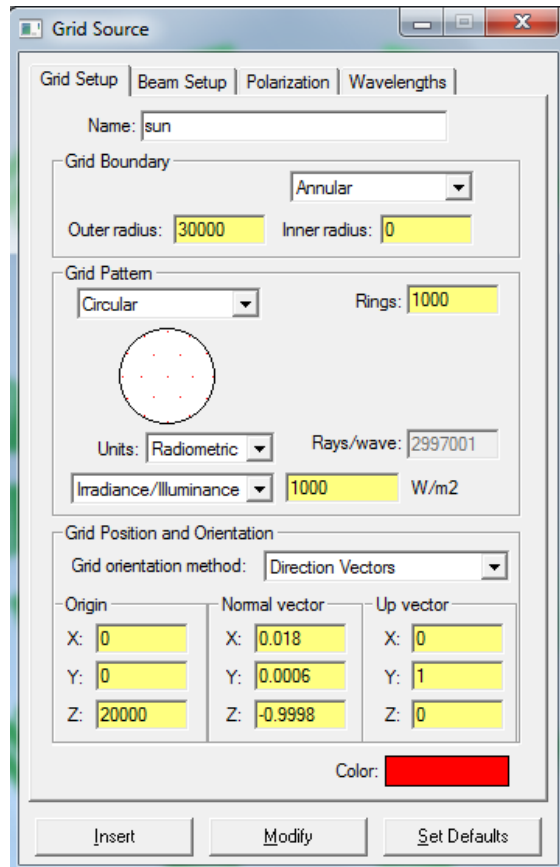


Figure 9. Grid Source example, grid stoup

- Beam Setup: Spatial profile is set to uniform, and angular profile is set to Solar, it is equivalent to a solar disk of 0.26 degree half angle.
- Polarization: Unpolarized ray setting is used to model solar radiation.
- Wavelength³: Wavelength is set to 0.5461 μm .

³ The reflectivity is of course spectrally dependent, but only an average value was available so it was necessary to trace only a single wavelength. The TracePro default value of $\lambda = 0.5461 \mu\text{m}$ was used. Sources can be defined as discrete wavelengths emitter.

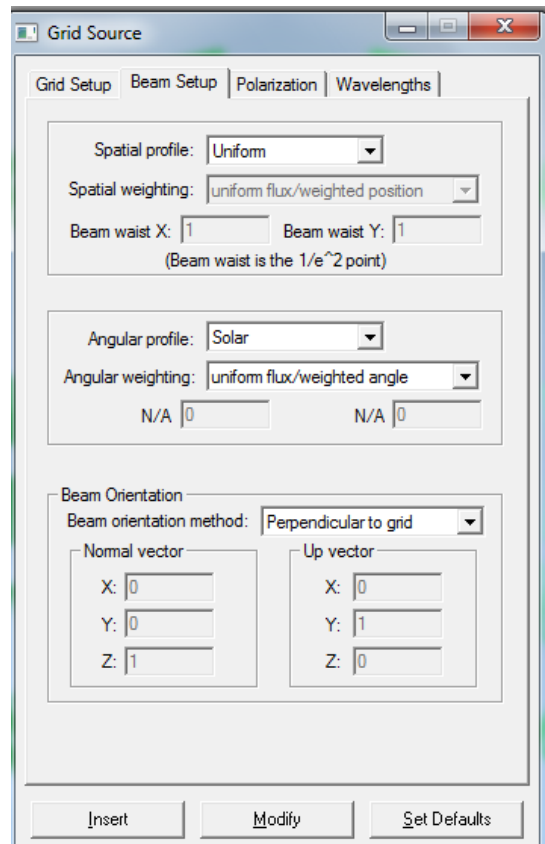


Figure 10. Grid Source example, beam setup

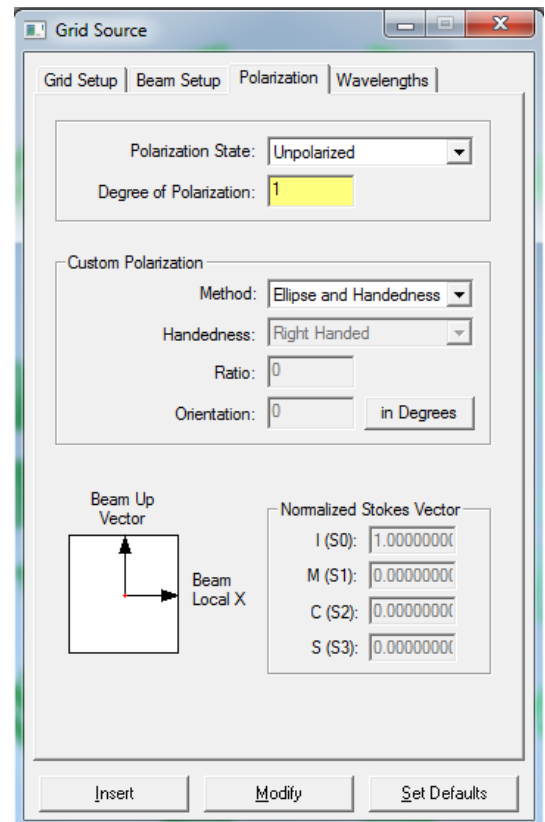


Figure 11. Grid Source example, polarization

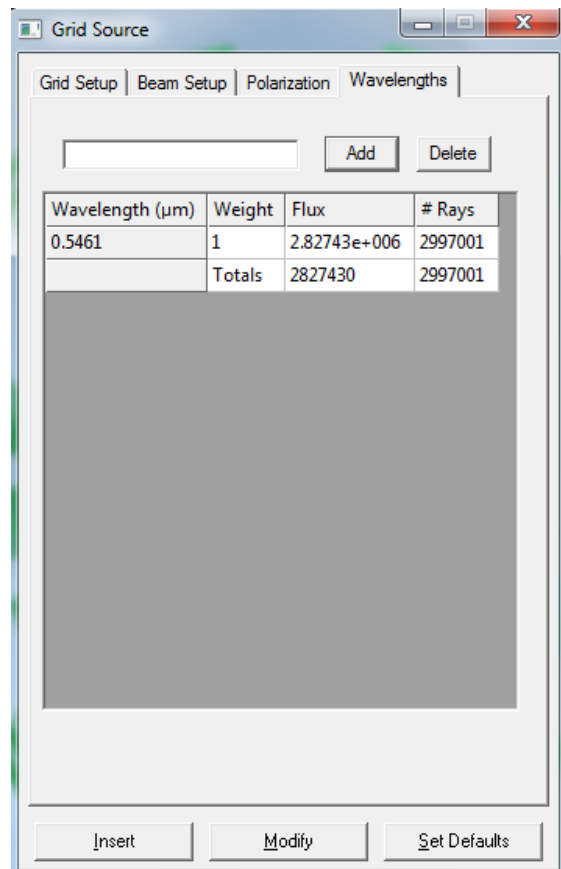


Figure 12. Grid Source example ,wavelength

File Source: A ray file can be inserted into a TracePro model and used as a source. A ray file consists of 7 columns of tabular data, (X,Y,Z) starting positions for each ray, [X Y Z] direction vector for each ray, and a flux (W).

The File Source concept provides the capability to:

- I. Incorporate measured source distribution data from opsira, Radiant Zemax [26], or other source measurement device into a TracePro model,
- II. “Continue” a raytrace by using data incident on one surface to be used as a source in another raytrace or another model, and
- III. Create a source from either theoretical or measured data in another application (e.g. - text editor or spreadsheet).

Regardless of the method used to create the ray file, the resulting File Source is inserted into a model in the same way. Method II is used to create a File source in parametric optimization of CPC and cone (refer section 2.3).

Surface Source: A surface source emits rays in a prescribed angular distribution from one or more surfaces of a solid object in the Model. A surface source is a surface that is designated to emit rays in a raytrace. There are five types of surface source properties in TracePro. Two types can emit discrete wavelengths (flux, irradiance) the two other can emit calculated wavelength distributions (e.g. blackbody or graybody). The fifth type, Surface Source Property, can emit either discrete wavelengths or calculated wavelengths.

2.2. Beam Down Model Definition

2.2.1. Basic definition

Coordinate System

A schematic of the BDOE heliostat field and tower is shown in Figure 13, the origin point of the global coordinate system is taken as the center point at ground level (300mm below top surface of central tower concrete slab). The positive X, Y and Z axes are pointed to north, west and upwards respectively.

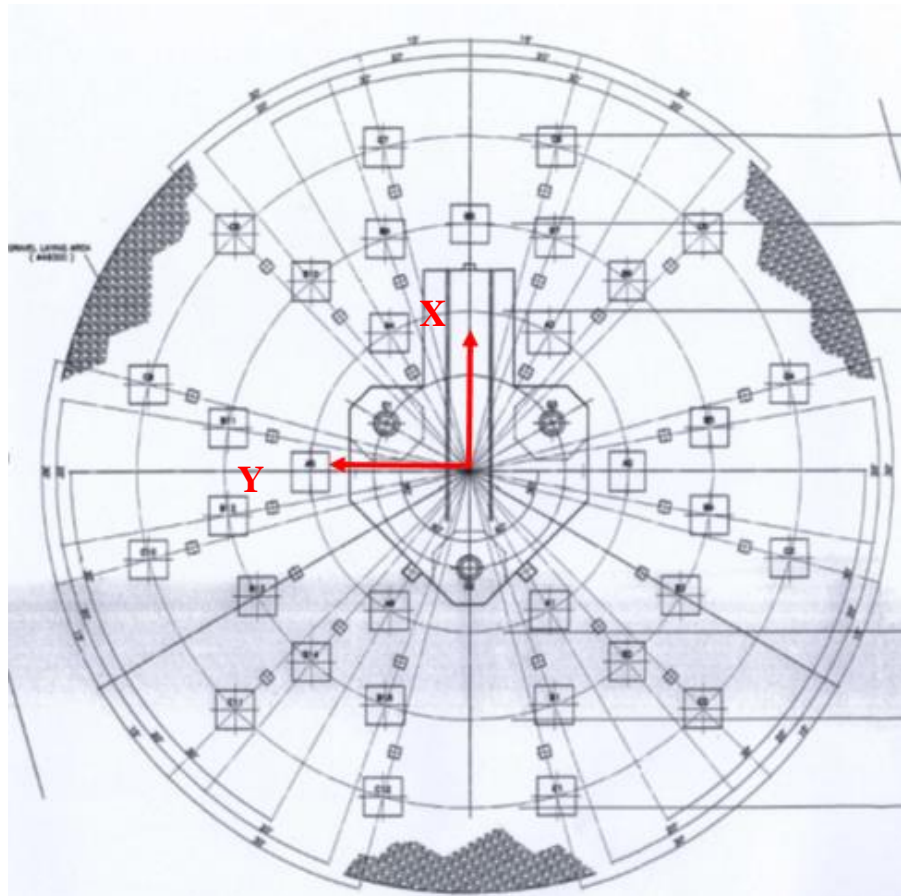


Figure 13. Heliostat layout

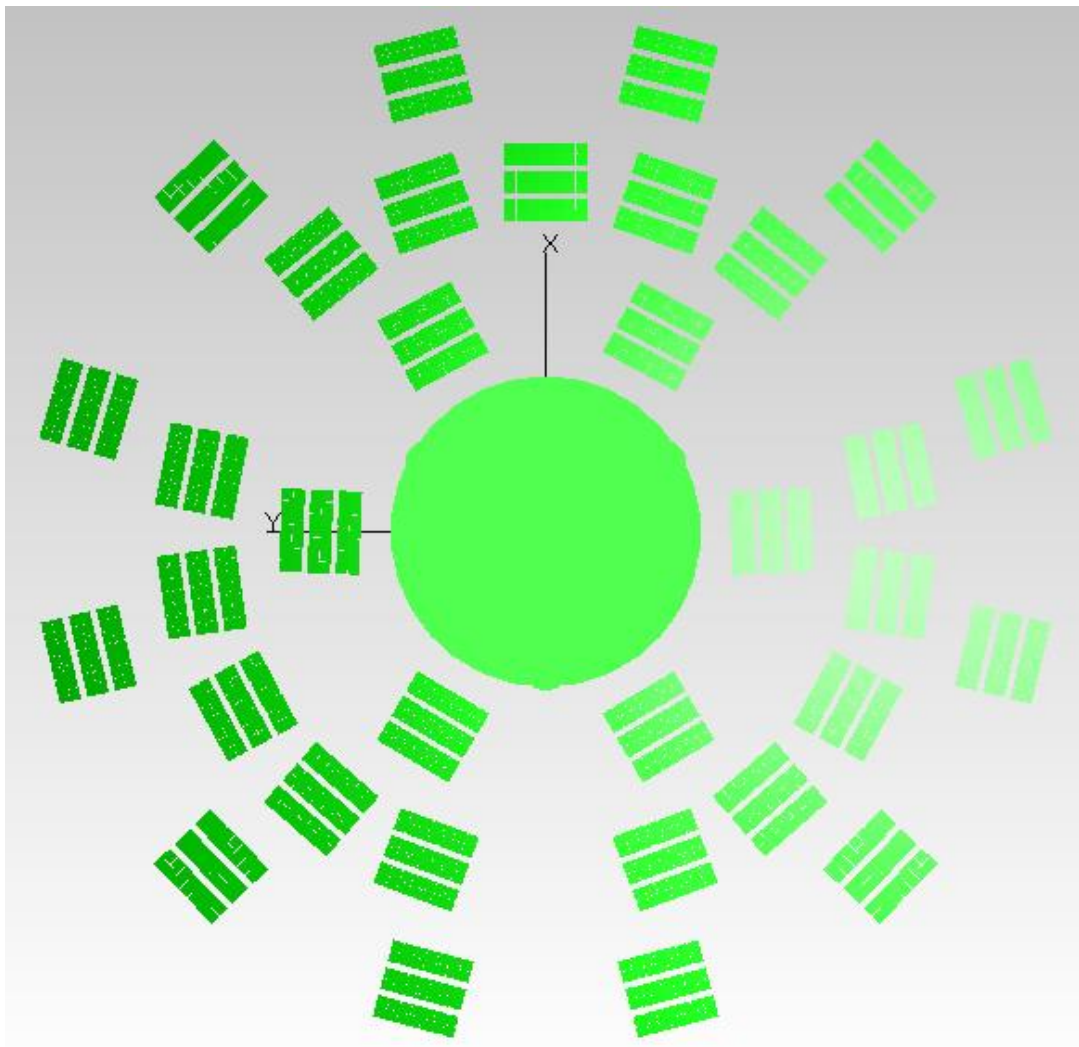


Figure 14. TracePro objects representing BDOE HS field and CR platform (top view)

A reference local coordinate system is used for each heliostat; the local axes (x, y and z) are parallel to the global axes and the origin point is taken at the ground level (same as the global XY plane), where the z axis passes through center of the heliostat (i.e. on the azimuth rotation axis of the heliostat).

The heliostat elevation angle is the angle between the control mirror surface normal and the xy plane, such that when the heliostat is pointing upwards (i.e. horizontal) the elevation angle will be 90° . The azimuth angle is the angle that any of the elevation axes makes with the Y-axis in the XY plane, measured positive clockwise.

Heliostat Definition

Each heliostat has 43 facets (or more precisely 41 full facets and two half facets).

Reflected rays from the central facet, aka control mirror, of each HS are detected by a sunsensor for pointing control. The inclination (canting) angle of every facet is defined with respect to the control mirror (Figure 15). This canting angle has been measured by Tokyo Tech using a special laser measurement tool. The facets are canted to provide the required focal length which is different for each ring (A, B or C) as mentioned in Table 16 (Appendix A).

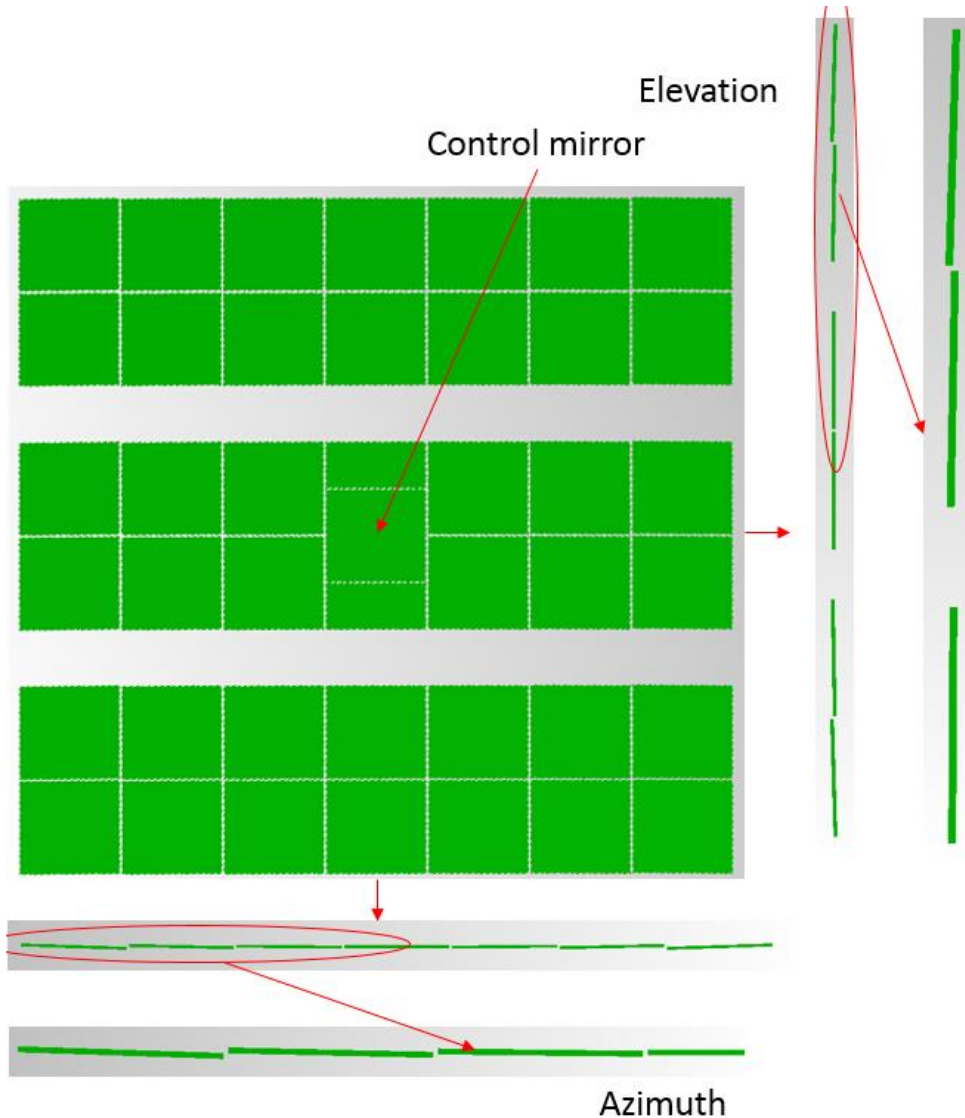


Figure 15. TracePro heliostat reference geometry

Central reflector canting

The Central Ray Convergence (CRC) point is the point on the Z axis, $(X, Y, Z) = (0, 0, Z_{\text{CRC}})$ where the central rays converge (Figure 17). The CRC plane, $Z=Z_{\text{CRC}}$ has the maximum flux, without FOE, for a given aperture. CR canting angles should generally be calculated based on Z_{CRC} nearly equal to the FOE (receiver absent FOE) inlet plane elevation. Consideration of maximum flux within the FOE and angular distribution at the FOE outlet may lead to selection of a CRC point somewhat below or above the FOE

inlet or even to different elevations for the A-, B- and C-ring CRC points, i.e. $Z_{CRC-A} \neq Z_{CRC-B} \neq Z_{CRC-C}$.

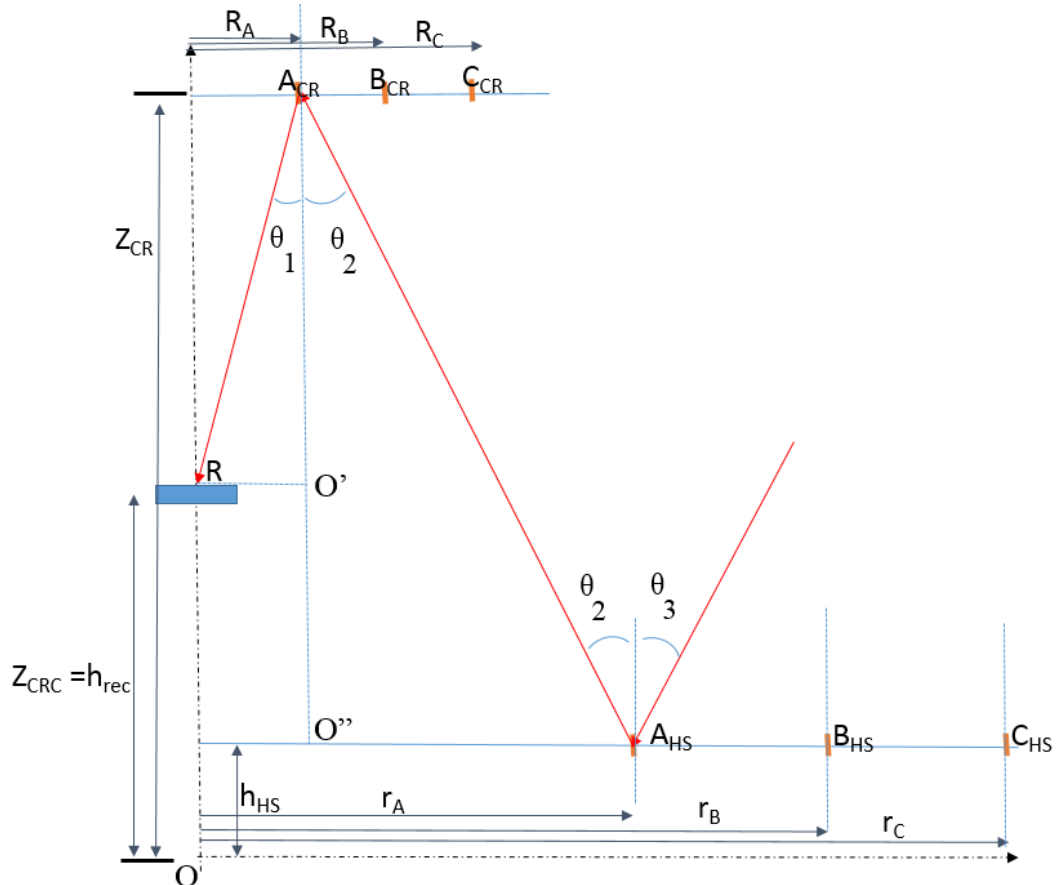


Figure 16 Central reflector canting trigonometry

Figure 16 shows the central ray from an A-ring HS in its vertical radial plane. From triangle $A_{CRC}O'R$ we have,

$$\tan \theta_1 = \frac{R_A}{Z_{CR} - Z_{CRC}} \quad (1)$$

And from triangle $A_{CRC}O''A_{HS}$ we have,

$$\tan \theta_2 = \frac{r_A - R_A}{Z_{CR} - h_{HS}} \quad (2)$$

Once θ_1 and θ_2 are known for the CR of A ring, θ_A can be calculated using the law of reflection.

$$\theta_A = \frac{\theta_1 + \theta_2}{2} \quad (3)$$

Using θ_A the normal vector of a CR in A ring can be easily calculated, similarly θ_B and θ_C , can also be calculated.

Table 1. Geometry of 100kW pilot plant as built for $Z_{CRC} = 2$ m

Parameter	Value(m)		
	A	B	C
CR height H_{CR} (m)	16.0		
HS height h_{HS} (m)		1.516	
Focal point height (m)		20.3	
Radius of CR R_A, R_B, R_C (m)	1.84	2.85	3.86
Radius of HS r_A, r_B, r_C (m)	8.74	13.54	18.34
Focal length f_A, f_B, f_C (m)	20.7	23.2	26.2

For example if $Z_{CRC} = h_{rec} = 6$ m, $\theta_A = 17.95^\circ$, $\theta_B = 26.17^\circ$ and $\theta_C = 33.05^\circ$. Central reflector normal orientation can be calculated using θ_A , θ_B and θ_C . The BDOE CR structure provides each CR facet with a 2-axis mount and means to change CR cantings for any given Central ray convergence height.

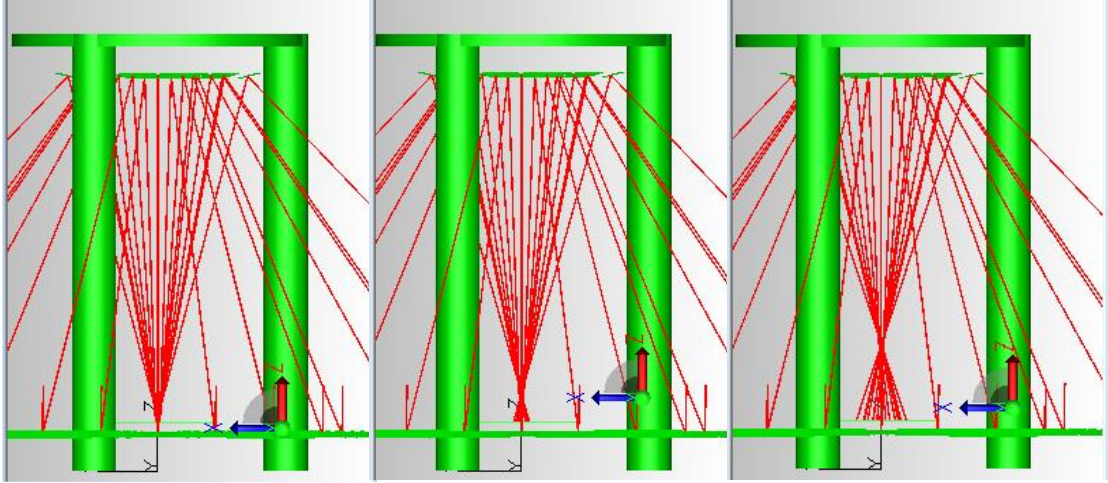


Figure 17. Central rays with CR canting adjusted for Central Ray Convergence heights of 0, 2 and 3 m above original target.

Sun position

Sun position is calculated using the NREL sun position algorithm *sun_position.m* [27] (*sun_position.m* input parameter include latitude and longitude of the BDOE origin, and civil time). The azimuth and zenith angle of sun are used to generate a sun vector which describes sun's position in the global coordinate system. This sun vector is later used to calculate the pointing direction (control mirror normal) of each heliostat.

Sun tracking

Once we have the sun vector and each heliostat's control mirror position, we can calculate the incoming ray incident angle. Similarly we can calculate required reflected ray direction from CR and HS control mirror center points coordinates. Based on incident ray and reflected ray we can calculate required normal of control mirror, this is how heliostat sun tracking works [28].

\hat{s} = Unit Sun vector

\hat{r}_k = reflected ray (unit) vector direction from k^{th} HS control mirror to k^{th} CR

$\hat{n}_{k,i}$ = control mirror normal (unit) vector for k^{th} HS, $i = 19$ ⁴

The incident and reflected ray will lie in the same plane as normal vector, thus:

$$(\hat{s} \times \hat{r}_k) \cdot \hat{n}_{k,19} = 0 \quad (4)$$

And the angle of incidence is equal to angle of reflection, thus:

$$\hat{s} \cdot \hat{n}_{k,19} = \hat{r}_k \cdot \hat{n}_{k,19} \quad (5)$$

$$\|\hat{n}_{k,19}\|_2 = 1 \quad (6)$$

2.2.2. Creating Scheme macro file (.scm) using Matlab

The BDOE has more than one thousand mirror facets. The position and orientation of each facet changes with sun position. To model a system this big and complicated its geometric construction should be automated. TracePro has Scheme macro language associated with it. For making this Scheme file we have written a Matlab script base code which can take BDOE geometry information and produce the Scheme macro file for input to TracePro. (The script could have been written in any other convenient language such as, python, java, VB, C, etc.)

Matlab base code explanation follows:

- 1) Reference geometries of each facet's center position and canting tilt angle, were tabulated in the MS excel (appendix A) for A-, B- and C- ring HS prototypes.
- 2) Facet vertex coordinates are calculated, to define each (A, B, C) heliostat as if placed in the global origin.

⁴ Number of heliostat are 33, k : 1 to 33.

Number of facet in one Heliostat is 43, i : 1 to 43, i= 19 is control mirror facet.

- 3) HS is translated and rotated to its position in the HS layout.
- 4) Similar technique (2-4) is used for each heliostat and each central reflector facet.
- 5) Once the heliostat and CR facets are in their correct reference positions, the HS control mirror facet's home position (center and normal) can be calculated by following:

If p_1 , p_2 , p_3 , and p_4 are vertices of the control mirror such that $p_1=[x_1,y_1,z_1]$,

$p_2=[x_2,y_2,z_2]$, $p_3=[x_3,y_3,z_3]$, and $p_4=[x_4,y_4,z_4]$ then

$$Facet\ center = \frac{(p_1 + p_2 + p_3 + p_4)}{4} \quad (7)$$

$$Normal_{facet} = (p_1 - p_2) \times (p_1 - p_3) \quad (8)$$

$$\hat{n}_{k,19,reference}^5 = \frac{Normal_{facet}}{\|Normal_{facet}\|} = [0\ 0\ 1] \quad (9)$$

- 6) Reflected ray direction can be found by using the HS central facet center coordinates and corresponding CR center coordinates:

$$reflected_{ray} = CR\ center - Control\ mirror\ facet\ center \quad (10)$$

$$\hat{r}_k = \frac{reflected_{ray}}{\|reflected_{ray}\|} \quad (11)$$

- 7) Sun vector is calculated, for given location and time, using the sun position algorithm [25].

⁵ $\hat{n}_{k,19,reference}$ is control mirror facet normal at home position of HS.

8) Using equations 4, 5, 6 and 11 the required normal direction of HS control facet $\hat{n}_{k,19}$ can be calculated. Now HS control mirror normals, $\hat{n}_{k,19,reference}$ need to be rotated to the $\hat{n}_{k,19}$ direction. $\theta_{k,azi}$ and $\theta_{k,ele}$ the angle between $\hat{n}_{k,19}$ and $\hat{n}_{k,19,reference}$.

Since the facets are arranged in three banks with separate elevation axes, it is necessary to rotate each bank separately. The facet centers are given in the local coordinate system of the heliostat, so we will first move them to another coordinate system where the elevation axis of each bank coincides with the y-axis of that coordinate.

If $c_{k,i}$ is the position vector of the center of the i^{th} facet in the heliostat local coordinate and e_1, e_2, e_3 are the vectors pointing to the centers of the elevation axes in the same coordinate system, then the facet centers relative to the elevation axes are given by,

$$c'_{k,i} = c_{k,i} - e_j \quad (12)$$

where i is the facet number from 1 to 43 and, j is the elevation axis number. For $i=1$ to 14 $j=1$, for $i=15$ to 29 $j=2$ and for $i=30$ to 43 $j=3$, Next we rotate these centers around the elevation axes using the y-axis rotation matrix:

$$c'_{k,i} = R_y(\theta_{k,ele} - 90)c'_{k,i} \quad (13)$$

where θ_{ele} represents the elevation angle and the counterclockwise rotation matrix around the y-axis, $R_y(\theta)$, is given by:

$$R_y(\theta) = \begin{bmatrix} \cos(\theta) & 0 & \sin(\theta) \\ 0 & 1 & 0 \\ -\sin(\theta) & 0 & \cos(\theta) \end{bmatrix} \quad (14)$$

The new facet centers are referenced to the heliostat local coordinate system:

$$c_{k,i} = c'_{k,i} + e_j \quad (15)$$

- 9) Now we can set the azimuth angle. Since all facets are rotated on the same azimuth axis (z-axis), the rotation is performed once for each (k^{th}) HS without distinction as follows:

$$c_{k,i} = R_z(\theta_{k,azi}) c_{k,i} \quad (16)$$

where θ_{azi} is the azimuth angle of the heliostat and the counterclockwise rotation matrix around the z-axis, $R_z(\theta)$, is given by:

$$R_z(\theta) = \begin{bmatrix} \cos(\theta) & -\sin(\theta) & 0 \\ \sin(\theta) & \cos(\theta) & 0 \\ 0 & 0 & 1 \end{bmatrix} \quad (17)$$

- 10) Write data to Scheme file. The Scheme file is a text file that carefully obeys the syntax of Scheme programming language as well as the TracePro object description rules. (Note: syntax of Scheme can be found in TracePro's help; recording macros is another way to deduce command macro for each action).

2.3. Problem Decomposition using ray vector file

Beam Down optical states can be captured at any location for a given sun position by a ray data file. The optical state above the FOE inlet plane is particularly useful. The ray data file provides a way of breaking down the problem to perform analysis in stages, in our case by saving ray data at 10m height for FOE optimization. The problem is thus divided into smaller parts; after reflection from HS and CR, ray information incident

on a defined plane can be saved. This saved ray data file can be used to define a source (refer section 2.1.3, and Figure 18) for further analysis of the final optical element.

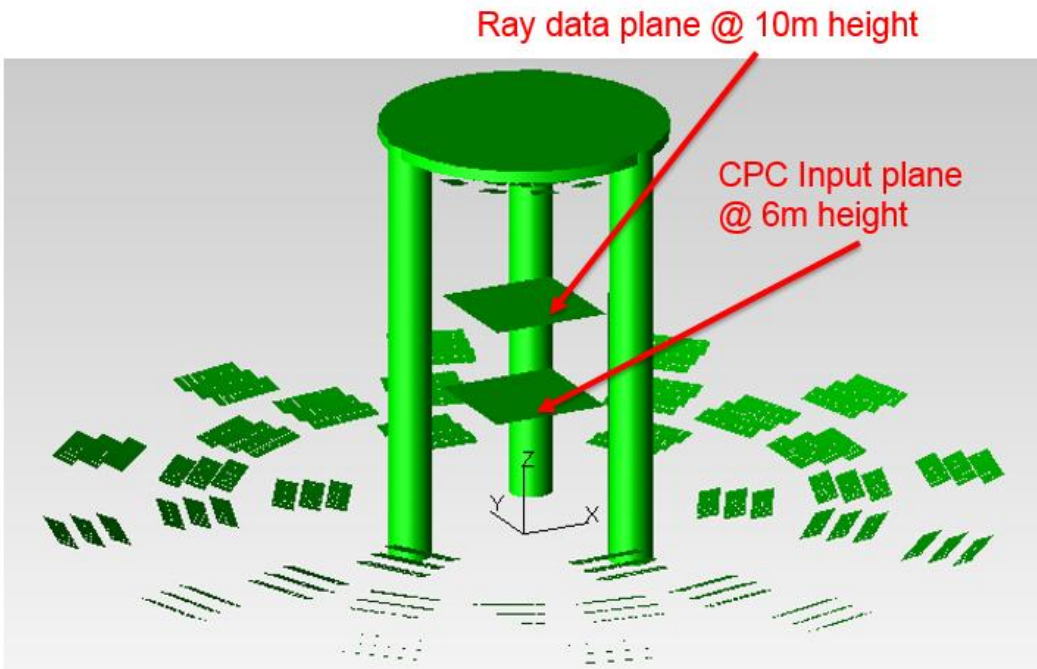


Figure 18. Beam Down TracePro model showing ray data plane at 10m

2.4. Results of BDOE Ray Trace Analysis

2.4.1. Evolution of flux at different elevations

When CR canting is set for any particular receiver height, flux distributions for different elevations should be checked. For example CR canting can be set to $Z_{CRC} = 6$ m and flux distribution checked for 6, 7, 7.5, 8, and 10 m elevations. To capture these flux distributions virtual planes have been incorporated in model (Figure 19 and Figure 20-Figure 25). Time used for the simulations in this example is 21st of June 2011 at 12:24:04 PM, UTC=+4hr (Zenith angle 1.023, azimuth angle 191.0) and HS canting errors are set to zero.

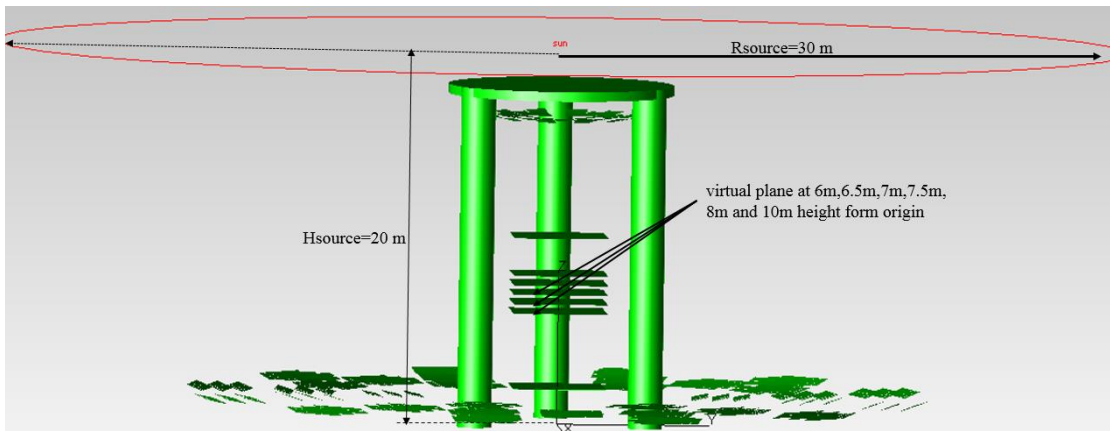


Figure 19. Beam down TracePro model with (virtual) flux mapping planes at different heights

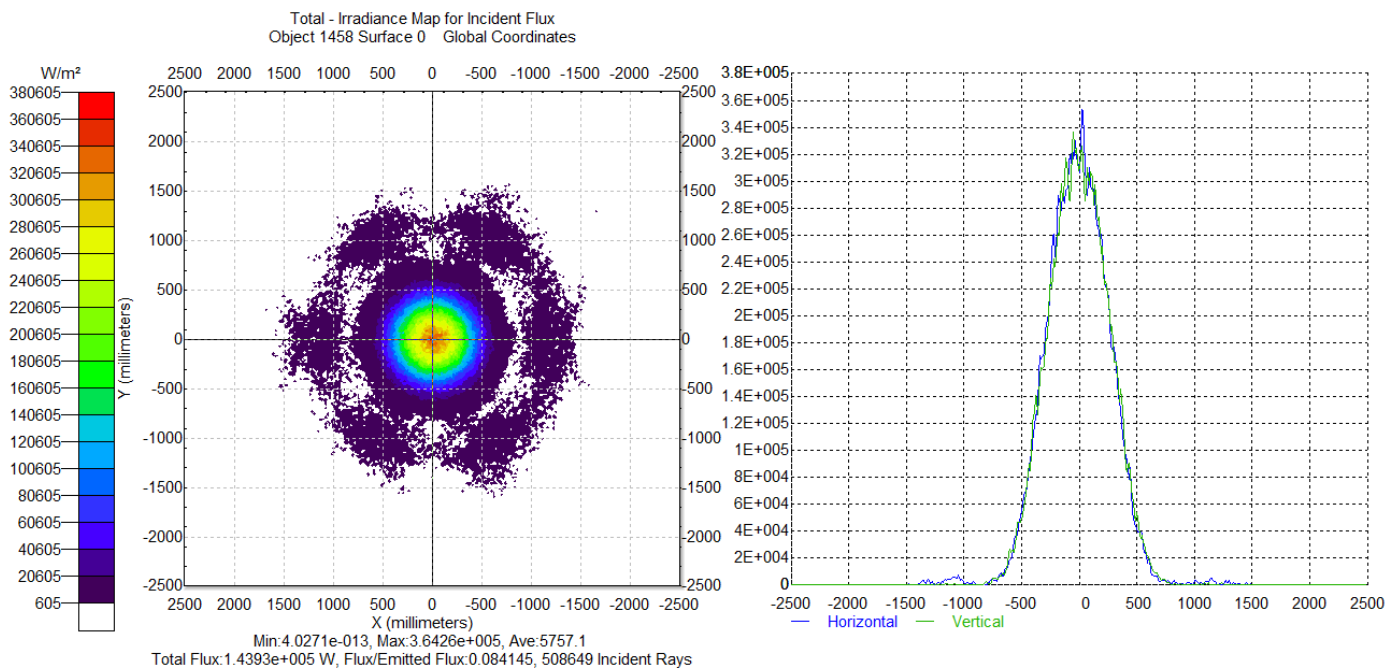


Figure 20 Flux distribution in plane at 6 m height while BDOE central ray convergence point (CR canting) is at 6-m height

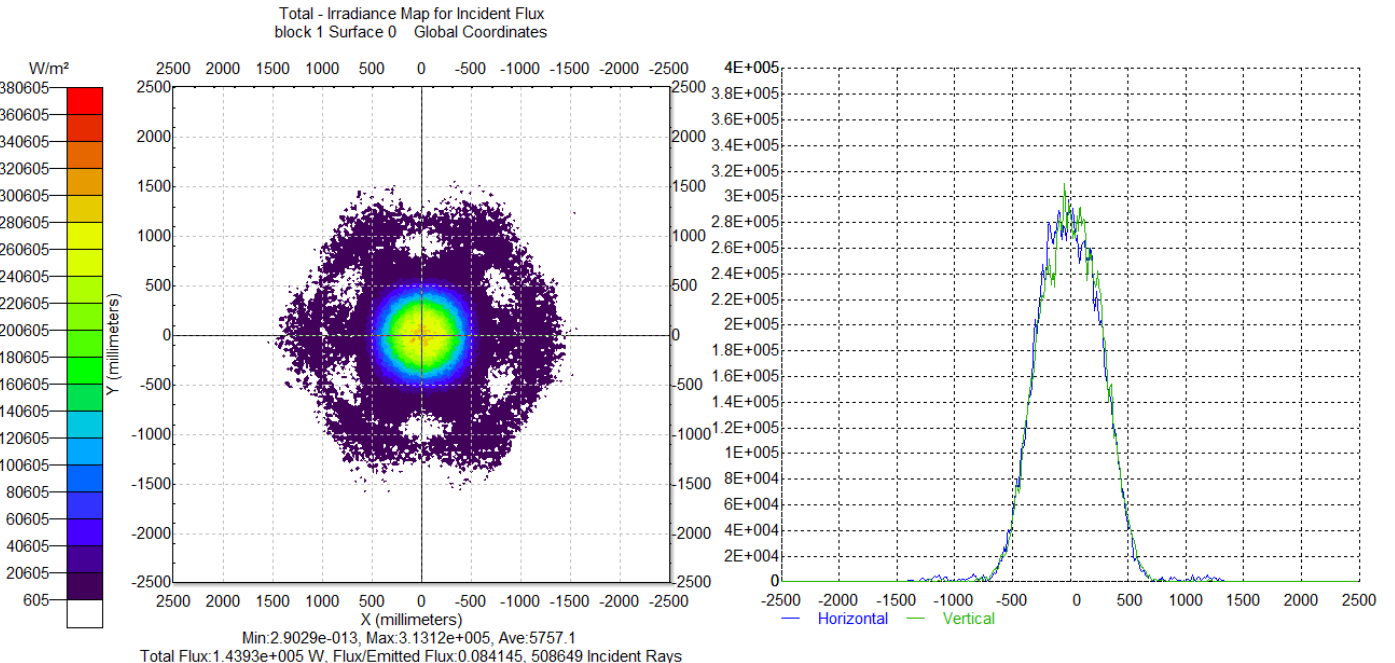


Figure 21 Flux distribution in plane at 6.5m height while BDOE central ray convergence point (CR canting) is at 6 m height

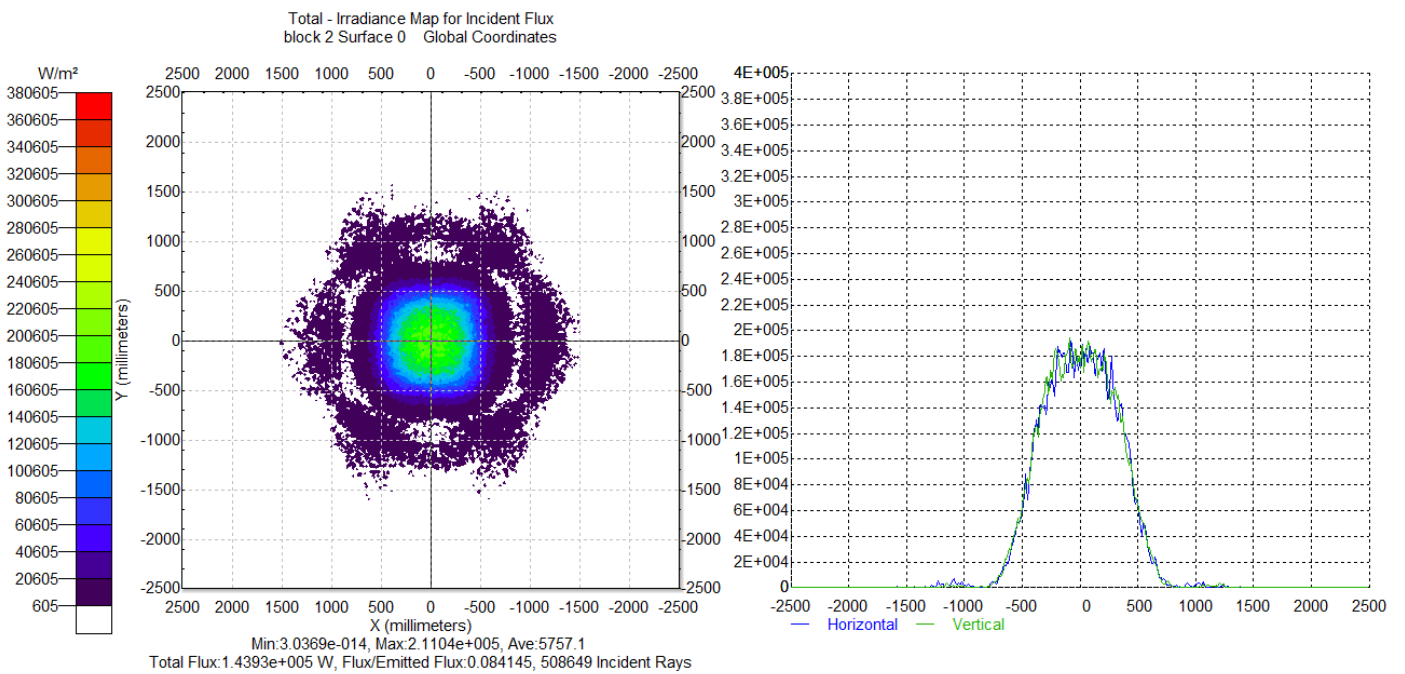


Figure 22 Flux distribution in plane at 7m height while BDOE central ray convergence point (CR canting) is at 6m height

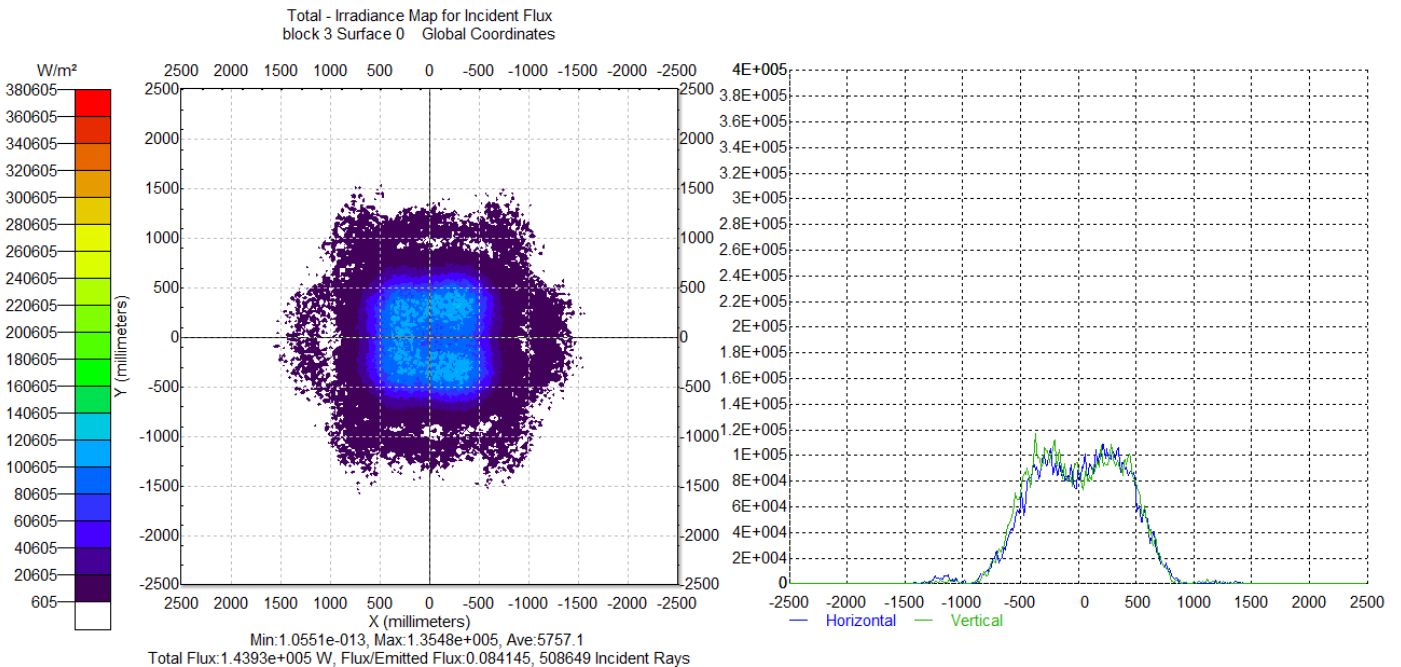


Figure 23 Flux distribution in plane at 7.5m height while BDOE central ray convergence point (CR canting) is at 6m height

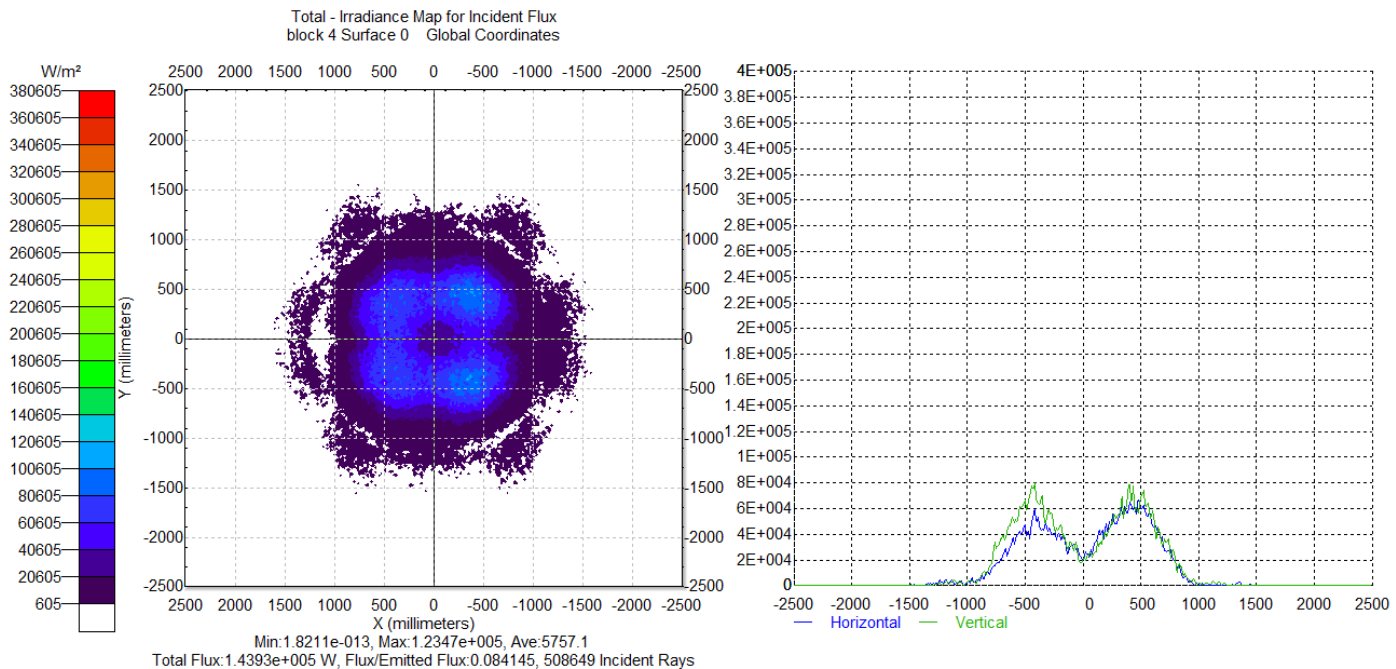


Figure 24 Flux distribution in plane at 8m height while BDOE central ray convergence point (CR canting) is at 6m height

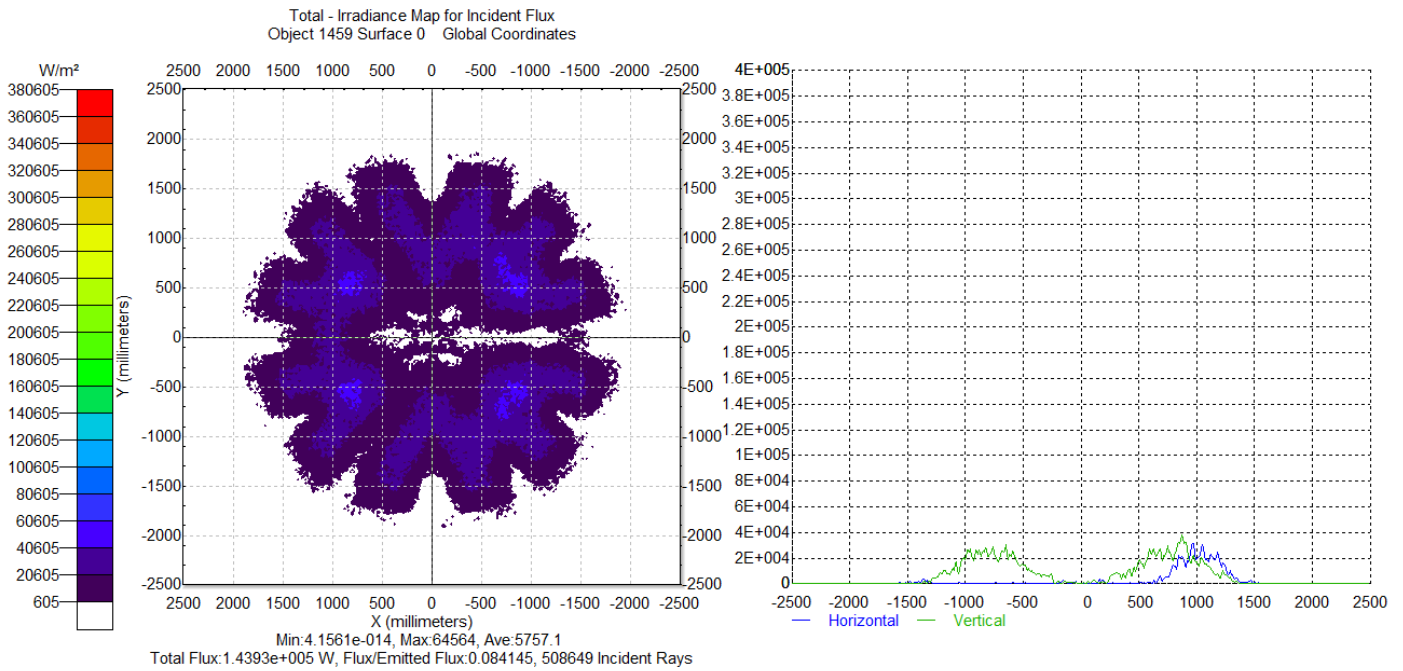


Figure 25. Flux distribution in plane at 10 m height while BDOE central ray convergence point (CR canting) is at 6m height

An alternative way of presenting flux maps on parallel planes is illustrated, for central ray convergence point set to 5 m, in Figure 26.

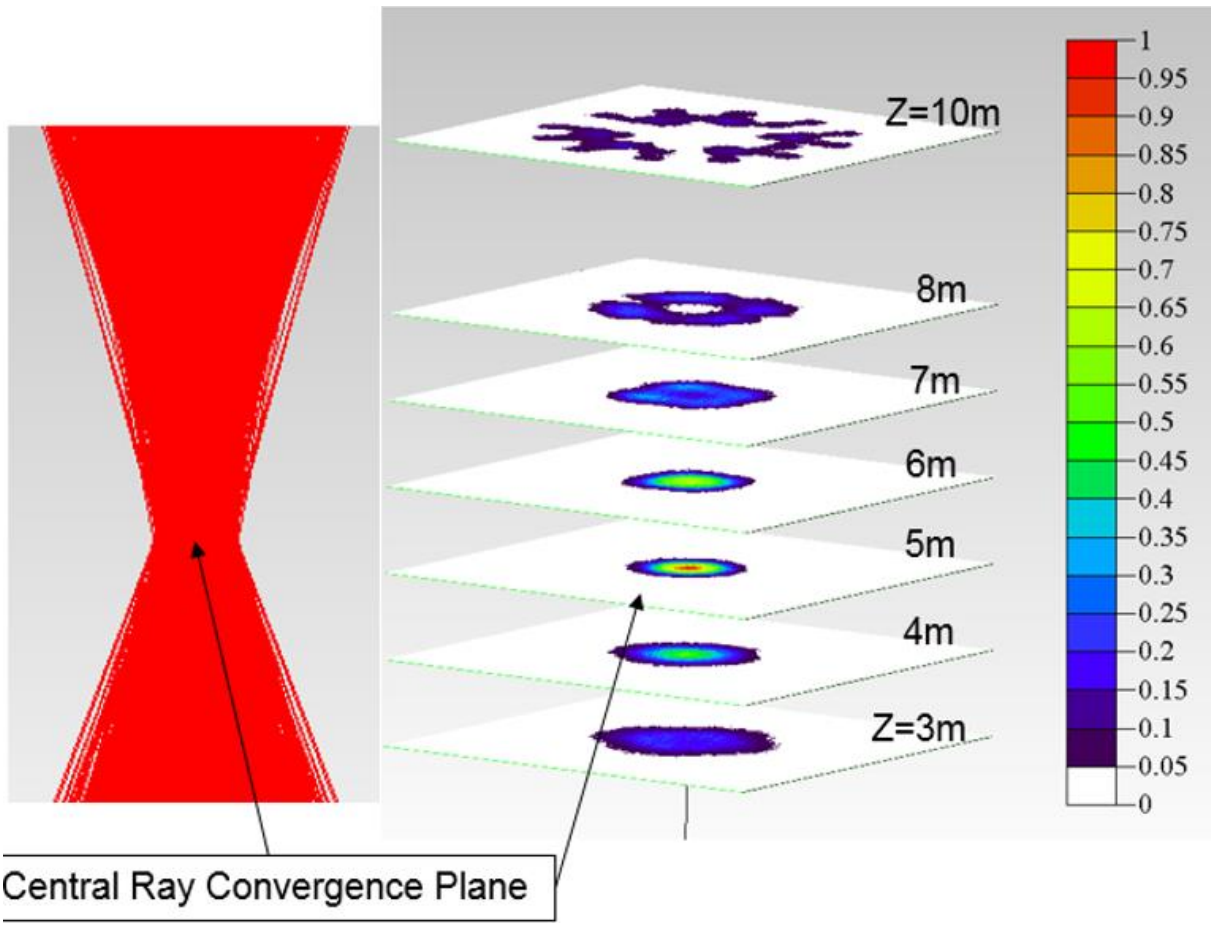


Figure 26. Irradiance map, normalized with respect to peak irradiance in the central ray convergence plane at 5m

2.4.2. Central ray convergence plane at different heights (6, 7 & 8 m)

Analysis for 6, 7 and 8 m target heights has been performed to check flux distribution and angular distribution of rays at different CRC heights (changing CR canting).

Figure 27 shows flux mapping (target) planes at 6, 7 and 8m elevations for illustration, with central ray convergence point at same elevation as target.

Figure 27 Paths of central ray reflecting from control mirror facet centers

Figure 28, Figure 29 and Figure 30 show that, although flux for 6, 7 and 8m CR cantings are similar; 8m CR canting has higher concentration than 7 and 6m cases because, in the former case, the target plane is nearer to A-, B- and C- ring reflected focal planes.

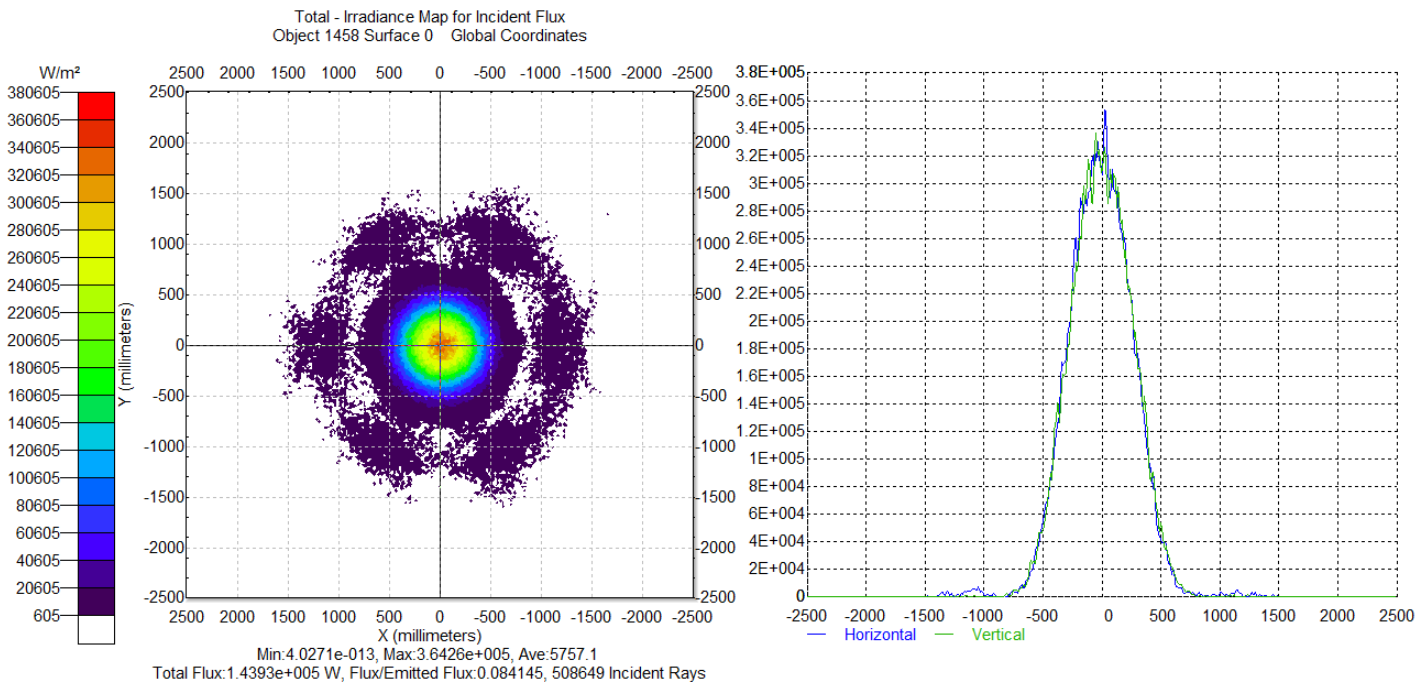


Figure 28 Flux distribution in plane at 6 m height while CRC point Z_{CRC} (CR canting) is set to 6 m height.

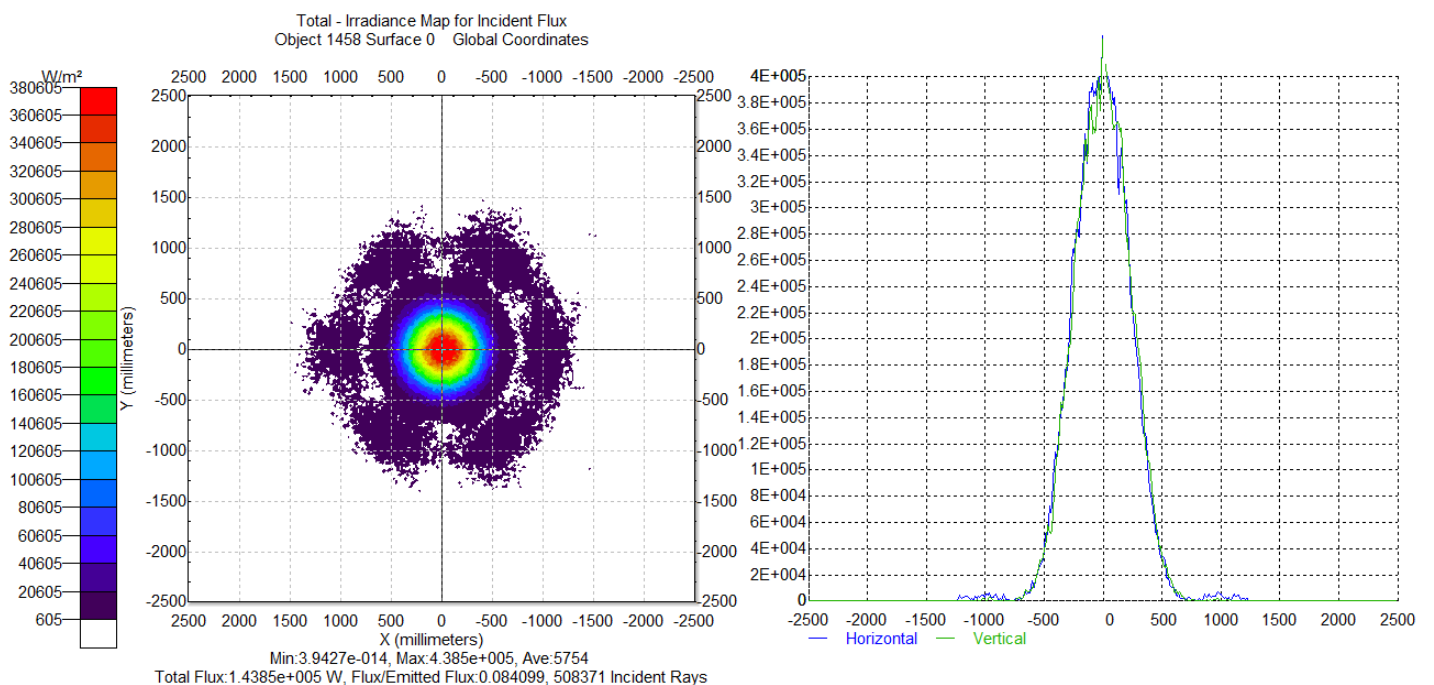


Figure 29 Flux distribution in plane at 7 m height while CRC point Z_{CRC} (CR canting) is set to 7 m height.

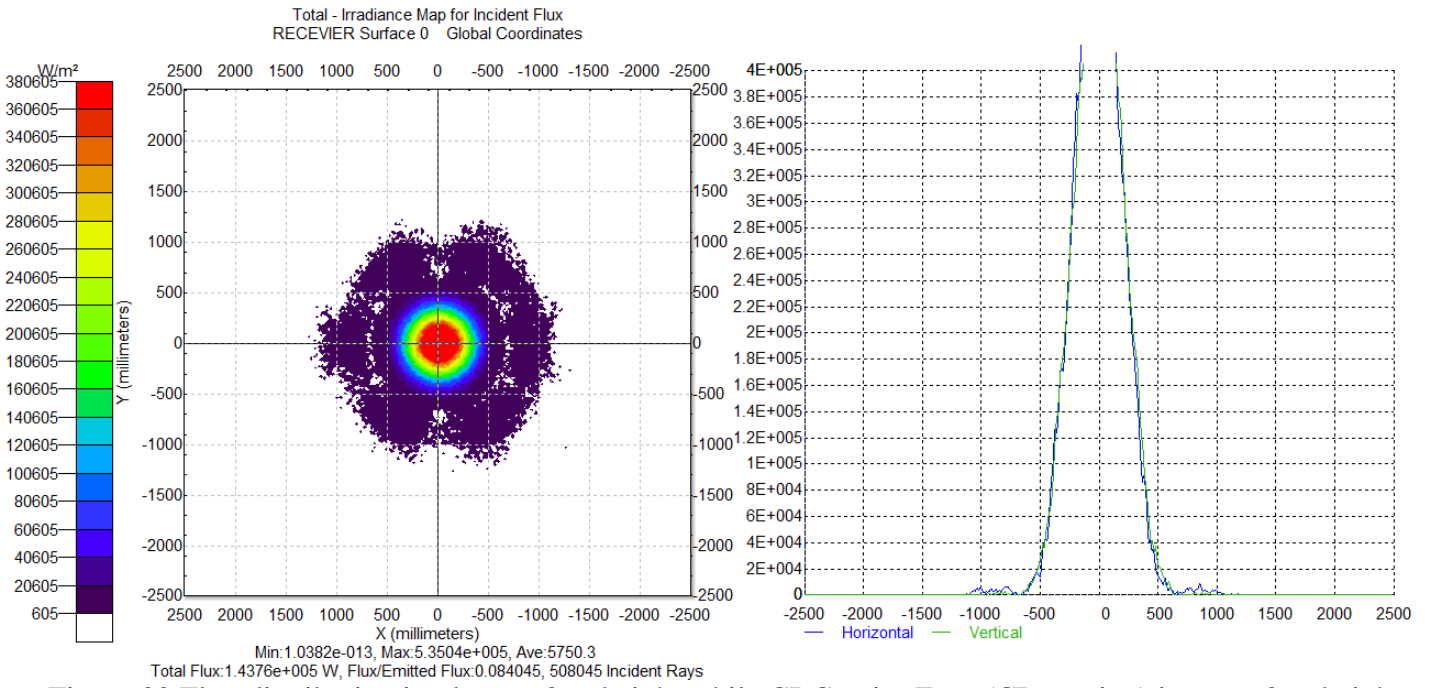


Figure 30 Flux distribution in plane at 8 m height while CRC point ZCRC (CR canting) is set to 8 m height.

2.4.3. Optical efficiency

Cosine factor has been calculated using linear Algebra. Shading, blocking, and spillage at CR [29] have been computed by ray tracing. The results are expressed as transmission factors so that overall optical efficiency is simply a product of transmission factors. For economy of words we refer to a transmission factor as an *efficiency*, of which there are several types, defined as follows.

Cosine efficiency = ratio of aggregate HS facet projected area to total area (no shading)

Shading efficiency = ratio of incident beam radiation with shading to that without,

Blocking efficiency = ratio of radiation reaching CR (blocking) plane to that reflected by all HS facets

Spillage efficiency = ratio of radiation reaching correct CR facets to that reaching CR (blocking) plane.

Cosine Efficiency

If p_1, p_2, p_3 , and p_4 are coordinates of mirror facet vertices, then;

$$\text{normal}_{\text{facet}} = (p_1 - p_2) \times (p_2 - p_3) \quad (18)$$

Projected area is calculated for each facet using following equation;

$$\text{projected area} = \text{normal}_{\text{facet}} \cdot \text{sun vector} \quad (19)$$

$$\text{total projected area} = \sum_{1}^{1419} \text{projected area} \quad (20)$$

$$\text{Cosine efficiency} = \frac{\text{total projected area}}{\text{total area}} \quad (21)$$

Shading Efficiency.

$$\text{Shading efficiency} = \frac{\text{Incident flux on heliostat}}{\text{total projected area} \times \text{DNI}} \quad (22)$$

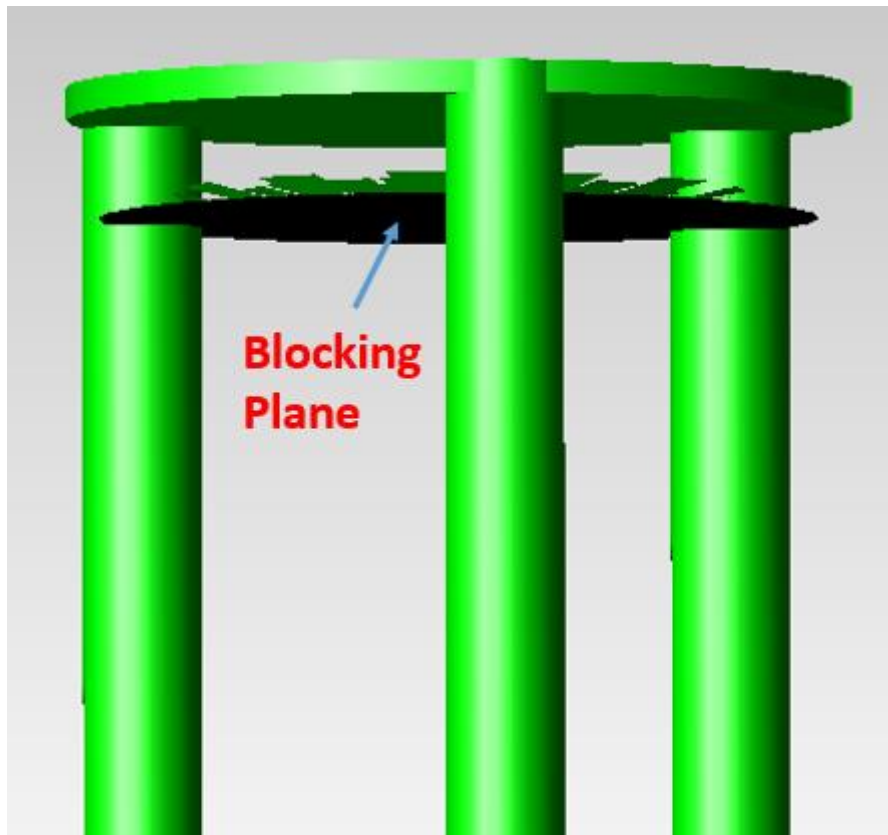


Figure 31 Blocking analysis plane

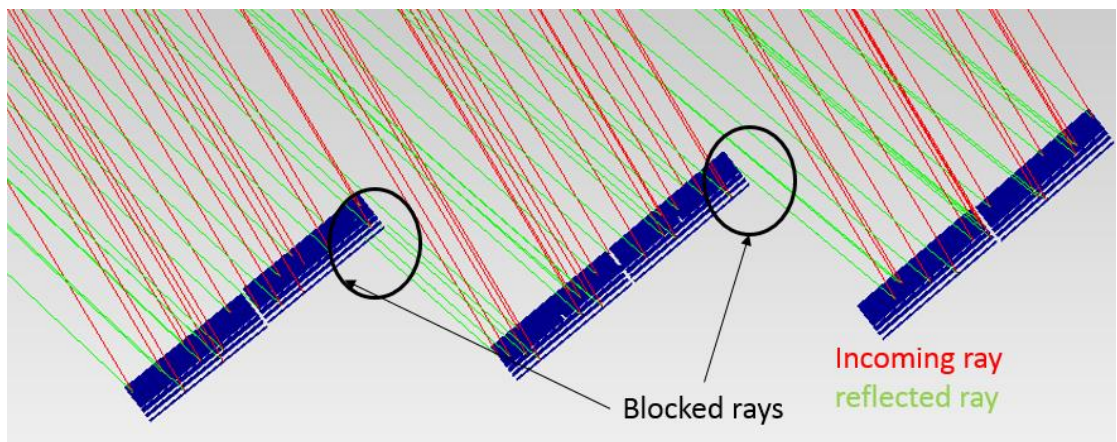


Figure 32 Illustration of blocking

Blocking efficiency.

$$\text{Blocking efficiency} = \frac{\text{Incident flux on blocking analysis plane}}{\text{Reflected flux from heliostat}} \quad (23)$$

Spillage efficiency of CR.

$$\text{spillage efficiency of CR} = \frac{\sum_{i=1}^{33} \text{Incident flux}_{HS_i \rightarrow CR_i}}{\text{Incident flux on blocking analysis plane}} \quad (24)$$

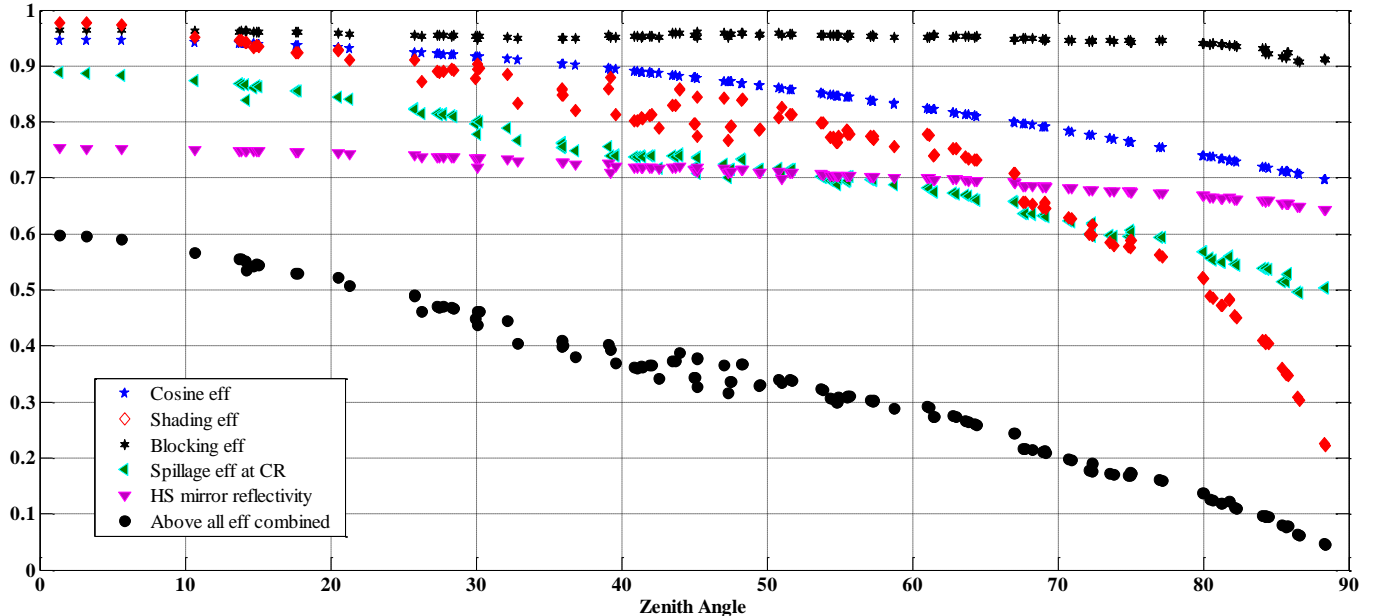


Figure 33 BDOE's cosine, shading, blocking, spillage efficiency of CR and HS reflectance⁶ vs zenith angle

Figure 33 shows that cosine efficiency is a direct function of zenith angle, but other efficiency factors also depend on azimuth angle.

Recommended “average day” of month and corresponding values of n [24] have been used to calculate above mentioned efficiencies. Of the component efficiencies, only shading shows a strong dependence on solar declination as shown in Figure 34.

⁶ HS mirror reflective property (Figure 69) is used to calculate HS reflectance vs zenith angle. HS mirror incident angle has been summarized in Figure 67.

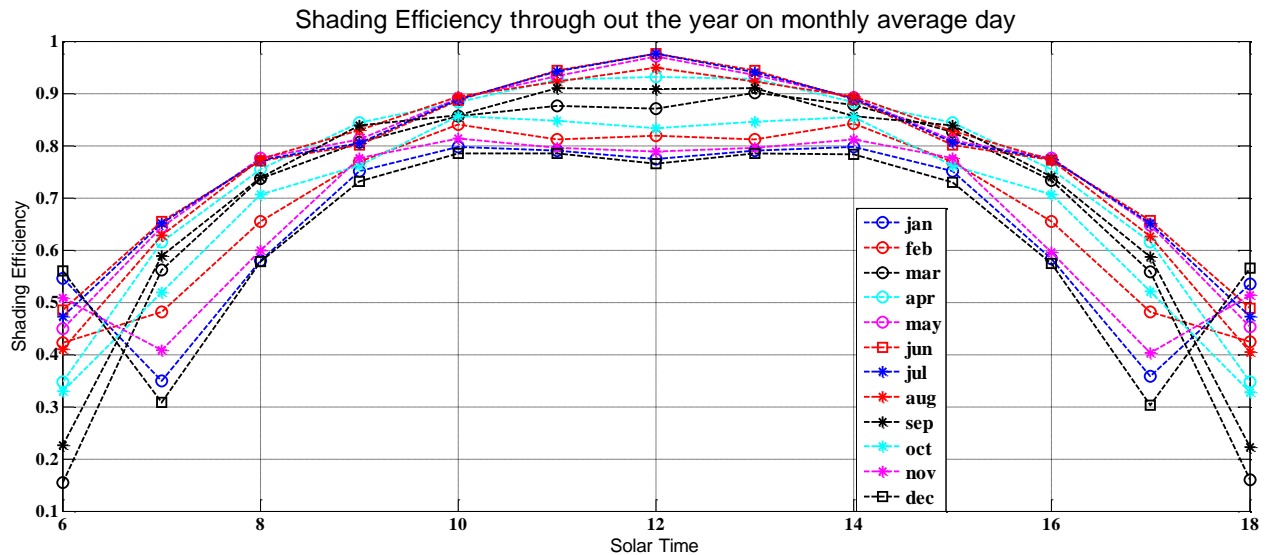


Figure 34 Shading Efficiency throughout the year on monthly average day

Table 2 Recommended Average Days for Months and Values of n by Months[24]

Month	n for i th Day of Month	For Average Day of Month		
		Date	n	δ
January	i	17	17	-20.9
February	$31 + i$	16	47	-13.0
March	$59 + i$	16	75	-2.4
April	$90 + i$	15	105	9.4
May	$120 + i$	15	135	18.8
June	$151 + i$	11	162	23.1
July	$181 + i$	17	198	21.2
August	$212 + i$	16	228	13.5
September	$243 + i$	15	258	2.2
October	$273 + i$	15	288	-9.6
November	$304 + i$	14	318	-18.9
December	$334 + i$	10	344	-23.0

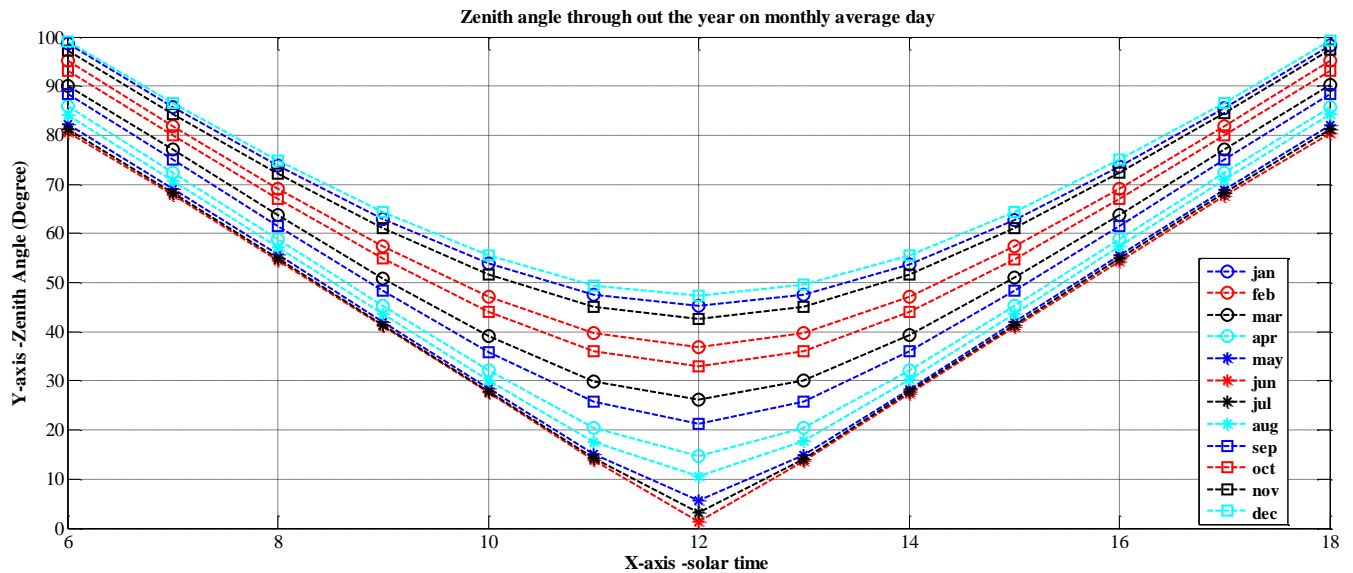


Figure 35 Zenith angle vs Solar time throughout the year on monthly average day

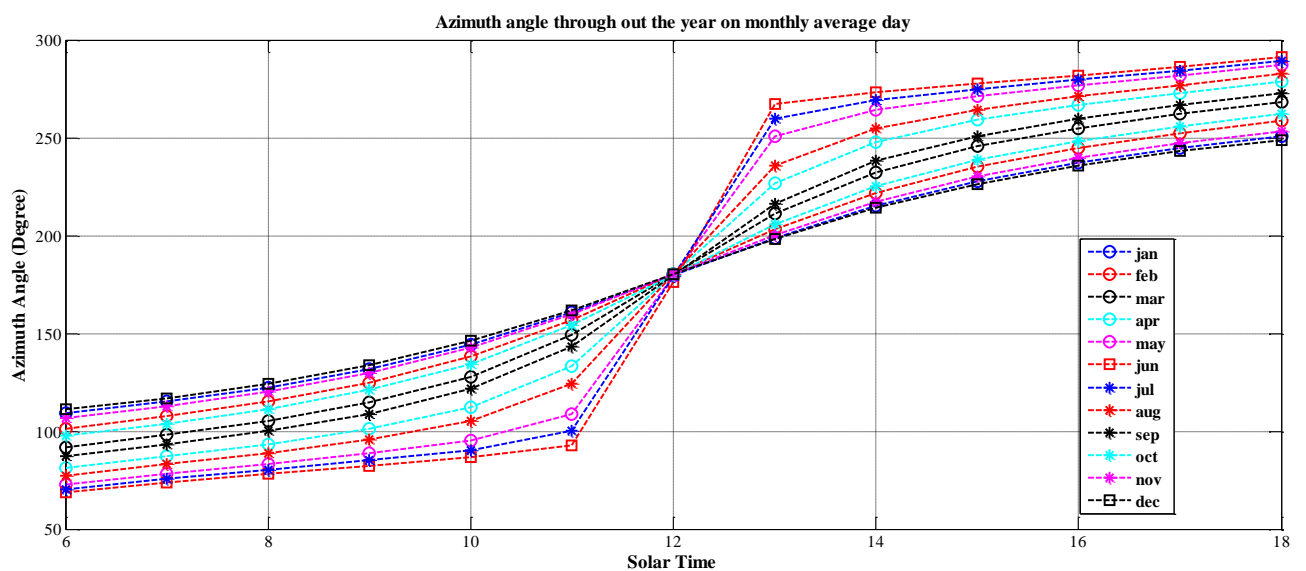


Figure 36 Azimuth angle vs Solar time throughout the year on monthly average day

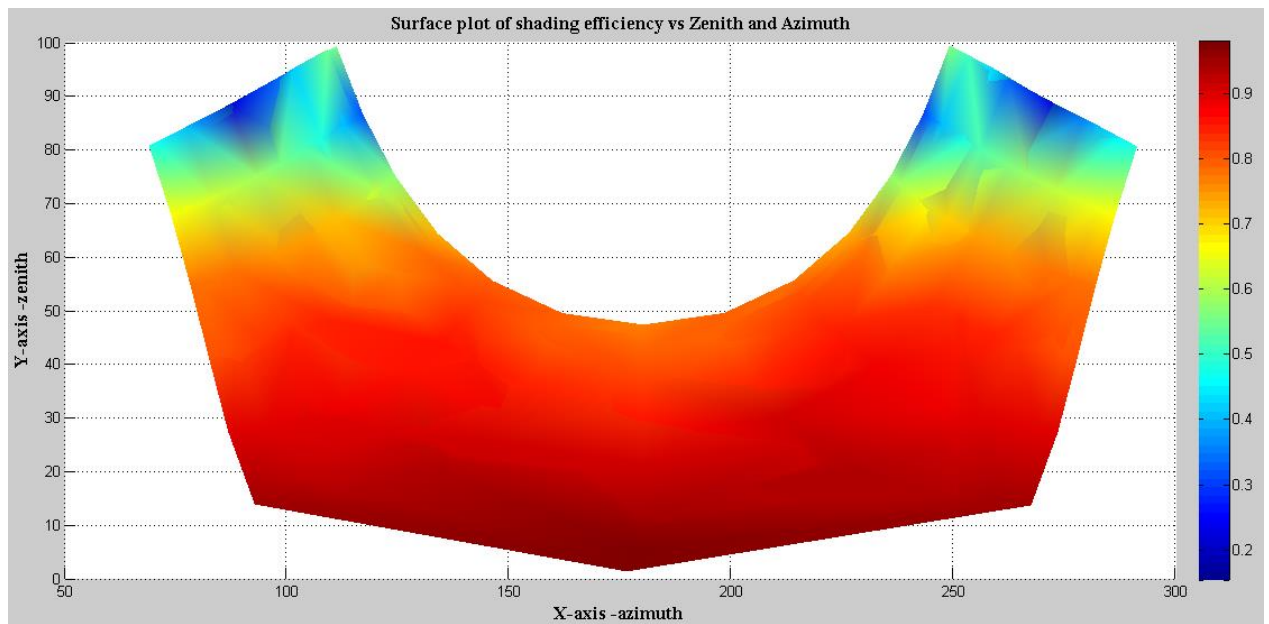


Figure 37 Surface plot of shading efficiency with respect to Zenith and Azimuth

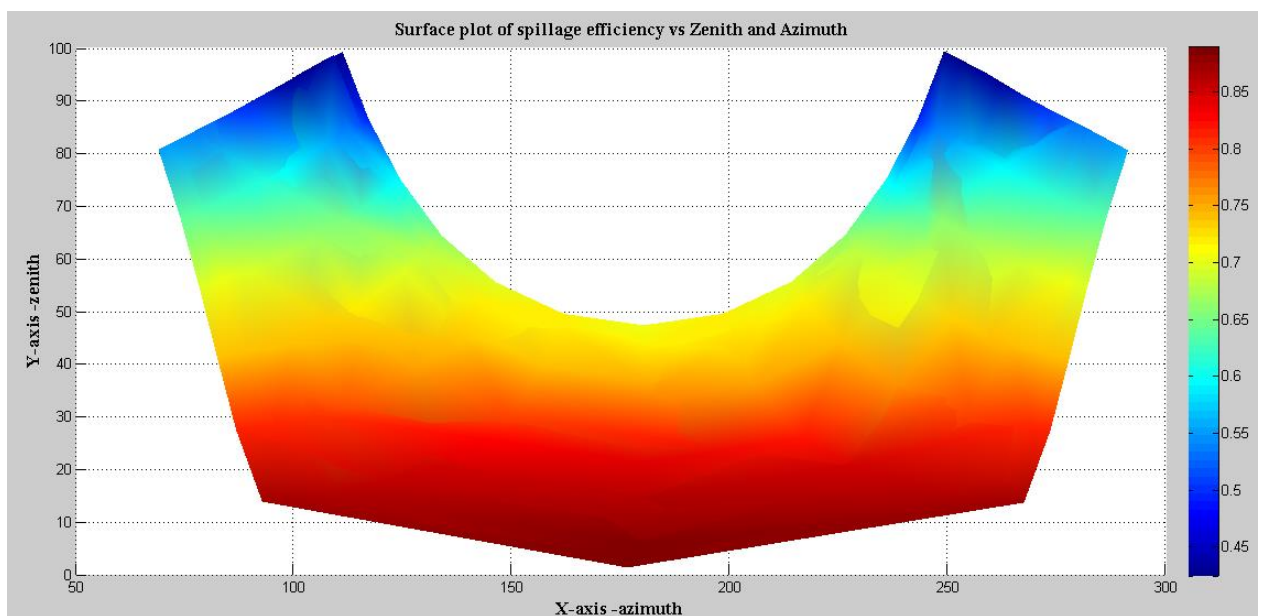


Figure 38 Surface plot of spillage efficiency with respect to Zenith and Azimuth

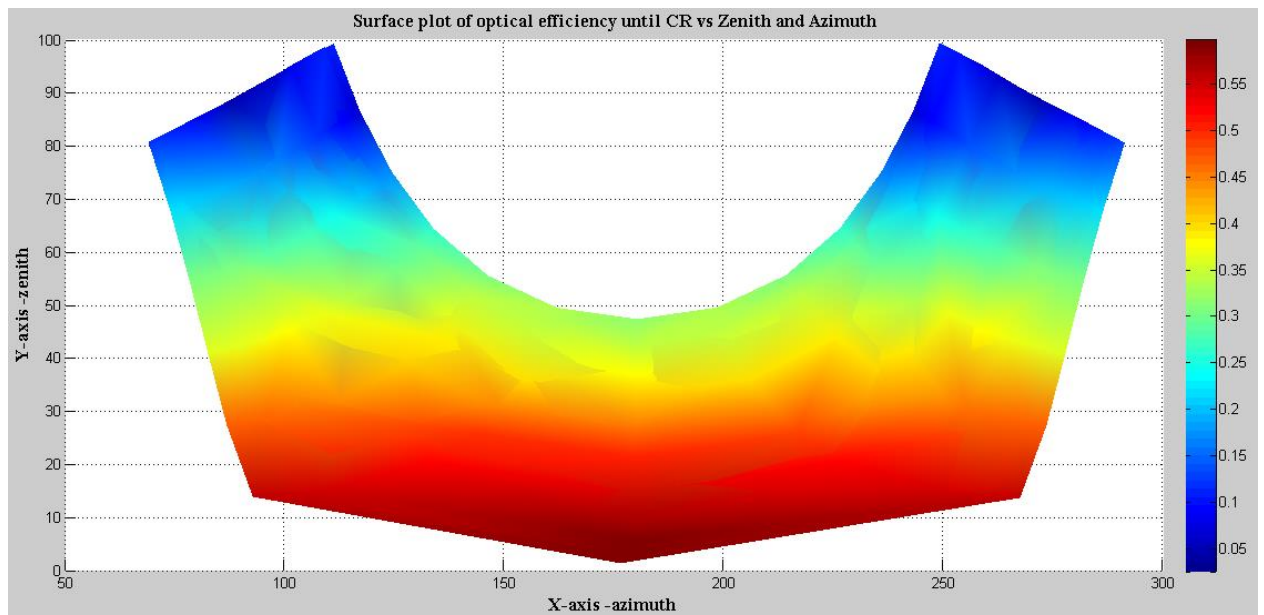


Figure 39 Optical overall efficiency until CR vs zenith and azimuth

CHAPTER 3

Final Optical Element

In this chapter optical analysis of final optical elements (CPC and cone) have been performed in context of BDOE. The angular distribution of flux leaving the FOE is important, in the case of a direct molten salt receiver, because when entering into molten salt, radiation will have reflection losses arising from change in refractive index between light transmitting media [24]. In the CSPond project, to avoid local hot spots that can cause salt degradation, a reasonably homogenous flux distribution is also required.

3.1. Final Optical Element

Figure 40 shows flux intercepted, thermal loss (refer appendix E) and net useful flux as functions of receiver size without FOE. Loss increases and average flux density decreases as receiver aperture radius increases. The purpose of a final optical element is to concentrate light/radiation on to a smaller aperture, which results in higher concentration and lower loss, therefore more net useful flux [30].

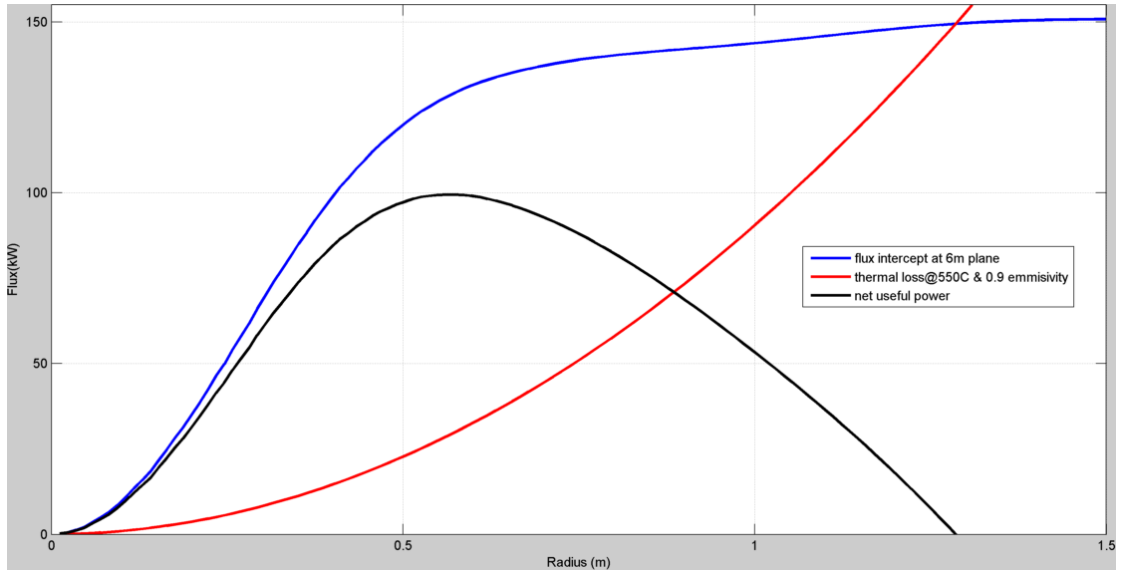


Figure 40. Net power collected as a function of receiver radius. Total incident flux⁷ and thermal loss are also shown.

3.2. CPC

The basic idea of non-imaging optics is to relax the constraints of point-to-point mapping which are required in imaging optics but which are not essential if one's goal is only to collect as much light as possible. This in turn permits the design of optical systems that achieve or closely approach the maximum geometric concentration permitted by physical conservation laws for a given angular field of view [31].

The compound parabolic concentrator (CPC) is the prototypical “ideal” nonimaging light collector invented by Roland Winston (1974) [32][33].

The 2-D CPC is a reflective concentrator with a tilted axis parabolic profile. The 2-D CPC is characterized by a step-like transmission efficiency allowing the efficient collection of light from 0° to a maximum angle, called the acceptance angle. For an incident collimated beam which makes an angle with the axis lower than acceptance angle the transmission efficiency is theoretically 100%. For a 3D CPC the cut off is not

⁷ No shaft tilt condition

abrupt as shown qualitatively in Figure 41. The roll-off shape depends on the distribution of skew rays entering the 3-D CPC.

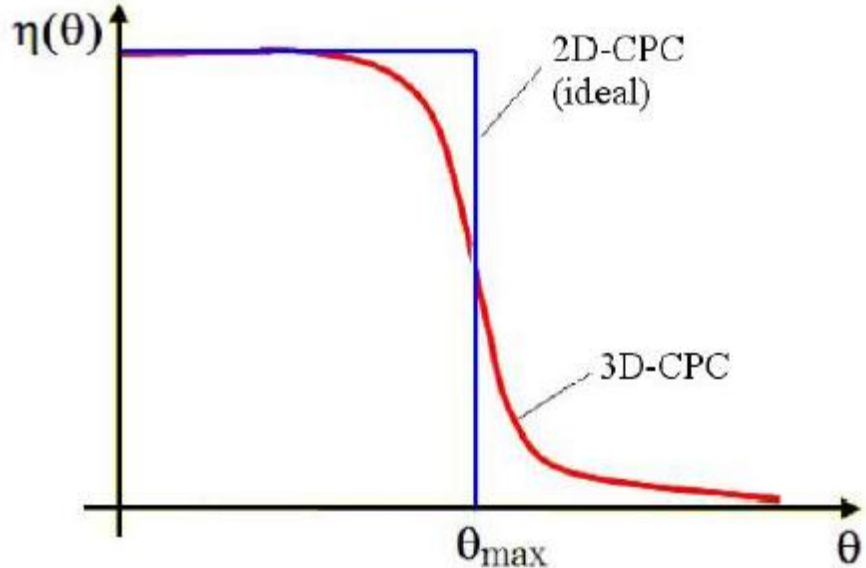


Figure 41. Characteristic transmission efficiency 2D and 3D CPC

3D-CPC geometry is characterized by the following parameters: a_{in} = inlet radius; a_{out} = outlet radius; L = length; θ = acceptance (or tilt) angle; and f = focal length of the parabolic profile. A conventional 3D-CPC is completely determined by two of the above five parameters, related by the following basic relationships:

$$f = a_{out}(1 + \sin \theta) \quad (25)$$

$$a_{out} = a_{in} \sin \theta \quad (26)$$

$$L = \frac{(a_{in} + a_{out})}{\tan \theta} \quad (27)$$

Only 2 parameters need to be fixed to fully define a 3D-CPC. The dimension of Inlet radius, with a_{in} and acceptance angle θ can be fixed. (With respect to BDOE, acceptance angle has physical significance, as BDOE max half angle could be calculated corresponding to the reflected rays from the C ring of CR, refer section 2.2.1)

The construction of a CPC is carried out, with reference to Figure 42 as follows [34]:

- 1) Draw a parabola P_1 , with focal length f , focal point at F_1 ,
- 2) Rotate the parabola with respect to F_1 axis perpendicular to parabola by angle θ_{acc} .
- 3) Consider curve above the point of intersection of P_1' and x axis, i.e. point F_2 . F_1F_2 is outlet radius.
- 4) Now the curve should be rotated with respect to perpendicular bisector of F_1F_2 .

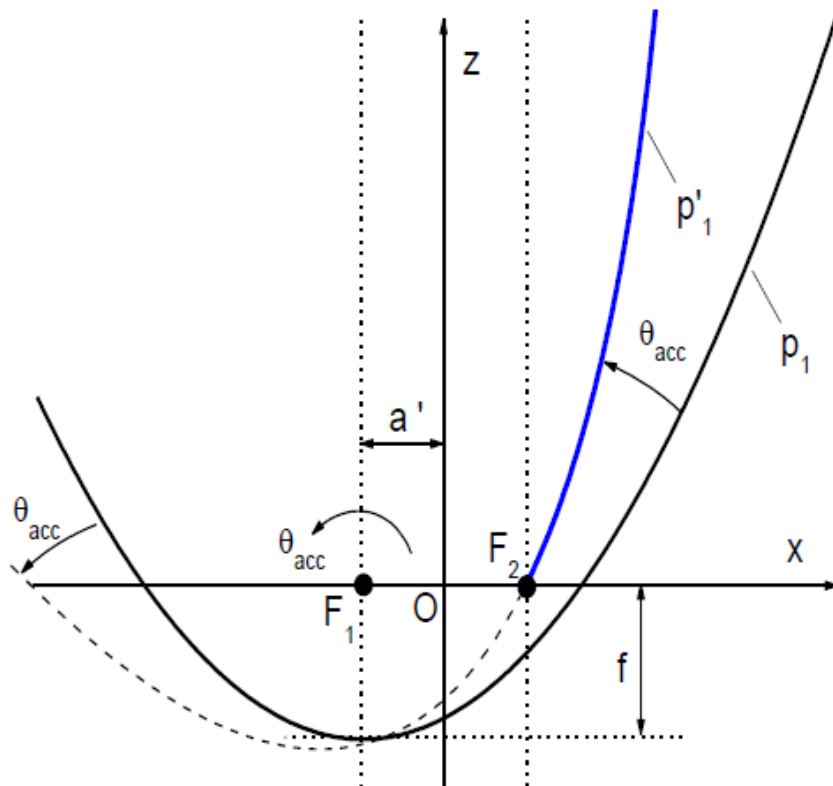


Figure 42. Construction of ideal 3D-CPC [34]

In TracePro terminology “lateral focal shift” is outlet radius, “axis tilt” is acceptance angle. If back length is set to zero then “front length” is length of CPC.

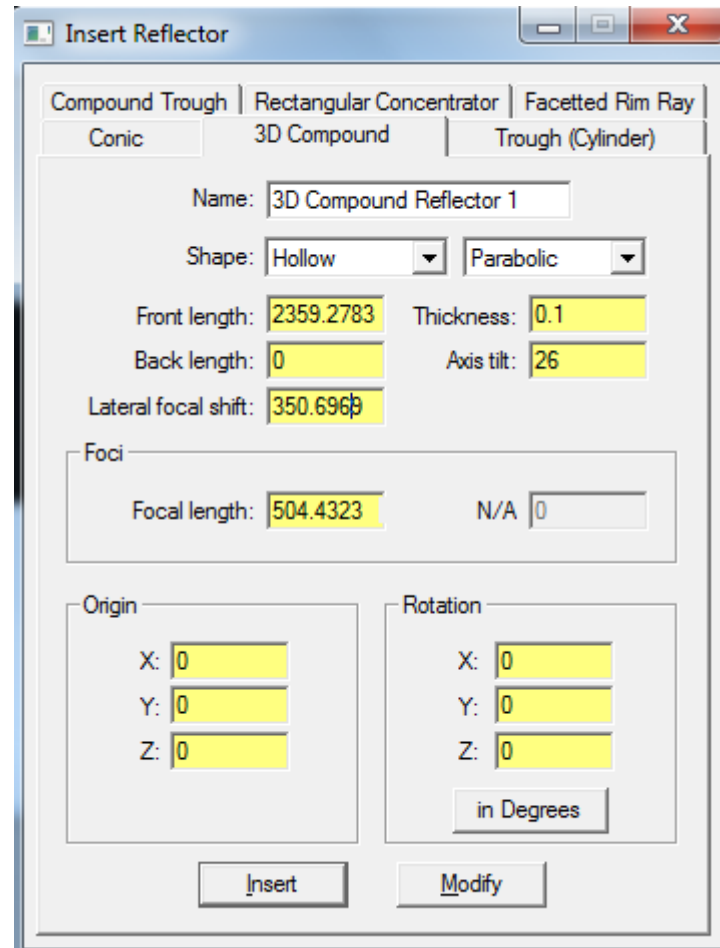


Figure 43. TracePro insert menu, reflector dialog box showing CPC parameters

3.3. CONE

Practical considerations, mainly easier and cheaper manufacturing, lead to alternative FOE geometries such as a faceted cone or compound cones, as a substitute for the 3-D CPC. A single-segment conical approximation to the CPC is shown in Figure 44 [35].

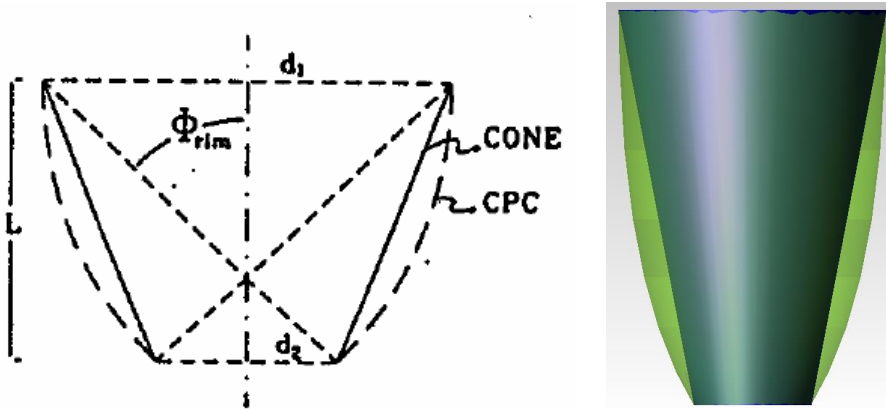


Figure 44. Scheme of cone and CPC showing entrance diameter, d_1 , exit diameter d_2 , half acceptance angle and axial length

3.4. Results

3.4.1. CPC

Table 4 reports CPC output with a central ray convergence point plane of 6m. The main purpose of this calculation is to find the ranges of inlet radius and half angle which give higher output. From the Table 4 it is clear that output flux doesn't change much with increasing inlet radius above 800mm. Reflectivity used here for CPC and cone is 95%.

Table 3 DNI, Azimuth and Zenith with respect to Solar time

Time	12 PM	10 AM	7 AM
Zenith angles (degree)	1.03	27.41	67.60
Azimuth angles (degree)	178.10	85.89	73.42
DNI(W/m ²)	796.0	724.5	140.0

Table 4. CPC output flux (kW)

		Inlet Radius (mm)						
		500	650	800	950	1100	1250	1400
12PM								
Half Angle (°)	24	116.5	130.4	134.1	135.3	137.3	139.9	141.6
	25	117.7	131.8	135.5	136.4	138.1	140.4	141.9
	26	118.0	132.2	135.8	136.7	138.3	140.5	142.0
	27	118.2	132.3	136.0	136.8	138.4	140.6	142.2
	28	118.4	132.5	136.1	136.9	138.5	140.8	142.3
10AM								
Half Angle (°)	24	75.0	89.6	95.7	97.6	98.9	101.0	103.5
	25	75.6	90.5	97.0	99.2	100.5	102.5	104.9
	26	75.9	90.8	97.4	99.7	101.1	103.2	105.5
	27	76.1	91.0	97.6	99.9	101.4	103.5	105.8
	28	76.4	91.4	98.1	100.6	102.2	104.4	106.9
7AM								
Half Angle (°)	24	6.9	8.4	9.1	9.4	9.5	9.8	10.2
	25	7.0	8.5	9.3	9.5	9.7	10.0	10.3
	26	7.0	8.6	9.3	9.6	9.7	10.0	10.4
	27	7.0	8.6	9.3	9.6	9.8	10.0	10.4
	28	7.0	8.6	9.3	9.6	9.8	10.0	10.4

Table 5 reports the net useful power. To calculate the net useful power, thermal loss is subtracted from optical power gain. Optical power gain is defined as:

$$\text{Power gain} = \text{CPC output flux} * \alpha; \alpha^8 = 0.95,$$

Thermal loss model (refer appendix E) is applied for a 600°C receiver, and the radiative and convective losses are calculated with regard to the CPC exit aperture area.

Table 5. Net useful flux (kW)

⁸ Absorptivity of the receiver in solar spectrum is assumed = 95%.

	Inlet Radius (mm)							
	500	650	800	950	1100	1250	1400	
12PM								
24	109.3	121.6	124.0	123.8	124.2	124.9	124.6	
25	110.3	122.8	125.1	124.5	124.4	124.7	124.0	
26	110.6	122.9	125.2	124.4	124.1	124.2	123.3	
27	110.6	122.9	125.0	124.2	123.7	123.7	122.6	
28	110.7	122.9	124.9	123.9	123.3	123.1	121.9	
10AM								
24	69.9	82.8	87.5	88.0	87.7	87.9	88.3	
25	70.4	83.6	88.5	89.2	88.8	88.8	88.8	
26	70.5	83.7	88.6	89.3	88.8	88.8	88.6	
27	70.6	83.7	88.5	89.1	88.6	88.4	88.1	
28	70.7	83.9	88.7	89.3	88.8	88.6	88.3	
7AM								
24	5.2	5.7	5.3	4.2	2.8	1.3	-0.3	
25	5.1	5.7	5.2	4.0	2.5	0.8	-1.0	
26	5.1	5.5	4.9	3.6	2.0	0.2	-1.7	
27	5.0	5.3	4.7	3.3	1.5	-0.4	-2.5	
28	4.9	5.2	4.4	2.9	1.0	-1.1	-3.4	

Table 5 also confirms that an inlet radius of 800mm gives close to the maximum output. Therefore for later analysis, inlet radii of 650, 800 and 950mm have been considered.

3.4.2. CONE

Because a cone doesn't have the sharp cutoff angle of a CPC, as was shown in Figure 41, a larger range of half angle has to be checked. Table 4 shows the cone output fluxes versus aperture and acceptance half angle.

Table 6 Cone output flux (kW)

Half Angle (°)	12PM			10AM			7AM		
	Inlet Radius (mm)								
	650	800	950	650	800	950	650	800	950
26	118.7	125.7	129.1	79.4	86.6	90.5	7.4	8.2	8.6
27	122.4	128.9	131.6	82.3	89.5	93.1	7.7	8.5	8.9
28	125.5	131.2	133.5	84.8	91.9	95.3	7.9	8.7	9.1
29	127.7	132.9	135.0	86.8	93.8	97.0	8.1	8.9	9.3
30	129.3	134.3	136.0	88.3	95.3	98.3	8.3	9.1	9.4
31	130.6	135.3	136.6	89.5	96.4	99.3	8.4	9.2	9.5
32	131.6	136.0	137.1	90.4	97.3	100.0	8.5	9.3	9.5
33	132.4	136.4	137.5	91.1	97.9	100.6	8.6	9.3	9.6
34	132.9	136.8	137.8	91.6	98.4	101.0	8.6	9.3	9.6
35	133.2	137.1	138.1	91.9	98.7	101.3	8.6	9.4	9.6

Note: outlet radius increases as inlet radius and half angle increase $a_{out} = a_{in} \sin \theta$

3.4.3. CSPonD's FOE

When radiation passes from medium 1 with refractive index n_1 to medium 2 with refractive index n_2 , reflectivity changes with respect to incident angle according to the Fresnel equation [24].

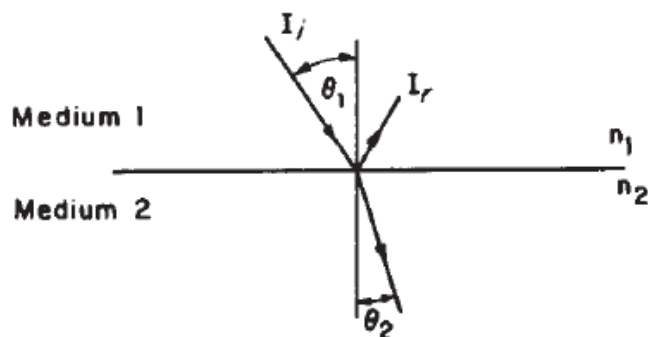


Figure 45 Angles of incidence and refraction in media [24]

Flux entering molten salt is tabulated in Table 7 and Table 8 for CPC and cone.

Table 7. Flux (kW) entering molten salt (CPC)

Half Angle ($^{\circ}$)

	12PM			10AM			7AM		
	Inlet Radius (mm)								
	650	800	950	650	800	950	650	800	950
24	122.4	126.6	128.1	83.7	89.7	91.9	7.9	8.5	8.8
25	124.0	127.9	129.0	84.9	91.0	93.2	8.0	8.7	8.9
26	124.8	128.4	129.2	85.5	91.7	93.9	8.1	8.7	9.0
27	125.2	128.6	129.2	86.0	92.1	94.2	8.1	8.8	9.0
28	125.5	128.7	129.2	86.5	92.7	94.9	8.1	8.8	9.1

Table 8. Flux (kW) entering molten salt (cone)

Half Angle ($^{\circ}$)

	12PM			10AM			7AM		
	Inlet Radius (mm)								
	650	800	950	650	800	950	650	800	950
26	111.1	118.0	121.6	74.3	81.1	84.8	6.9	7.6	8.1
27	115.1	121.6	124.7	77.2	84.1	87.7	7.2	8.0	8.4
28	118.4	124.5	127.0	79.8	86.7	90.1	7.4	8.2	8.6
29	121.1	126.6	128.9	82.0	88.8	92.1	7.7	8.4	8.8
30	123.1	128.3	130.3	83.8	90.6	93.6	7.8	8.6	8.9
31	124.8	129.6	131.3	85.2	92.0	94.9	8.0	8.7	9.1
32	126.0	130.6	131.9	86.3	93.0	95.8	8.1	8.8	9.1
33	127.0	131.3	132.5	87.2	93.9	96.6	8.2	8.9	9.2
34	127.8	131.8	133.0	87.9	94.5	97.2	8.2	9.0	9.3
35	128.4	132.3	133.3	88.4	95.0	97.6	8.3	9.0	9.3

Reflectance efficiency can be defined as follows:

$$\text{reflectance efficiency} = \frac{\text{Flux entering molten salt}}{\text{Flux Output of FOE}} \quad (28)$$

Table 9 and Table 10 show reflectance efficiency.

Table 9 Flux entering molten salt/output of CPC

Half Angle (°)	12PM			10AM		
	Inlet Radius					
	650	800	950	650	800	950
24	0.938	0.944	0.947	0.934	0.937	0.941
25	0.941	0.944	0.945	0.938	0.938	0.940
26	0.944	0.945	0.945	0.942	0.942	0.942
27	0.946	0.945	0.945	0.945	0.944	0.943
28	0.947	0.945	0.944	0.946	0.945	0.943

Table 10 Flux entering molten salt/output of cone

Half Angle (°)	12PM			10AM		
	Inlet Radius					
	650	800	950	650	800	950
26	0.936	0.939	0.942	0.935	0.936	0.937
27	0.940	0.944	0.948	0.938	0.940	0.942
28	0.944	0.949	0.952	0.941	0.943	0.946
29	0.948	0.952	0.955	0.945	0.947	0.949
30	0.953	0.955	0.958	0.949	0.951	0.953
31	0.956	0.958	0.961	0.953	0.954	0.956
32	0.958	0.961	0.963	0.955	0.956	0.958
33	0.960	0.963	0.964	0.957	0.959	0.960
34	0.962	0.964	0.965	0.960	0.961	0.962
35	0.964	0.965	0.966	0.962	0.963	0.963

Table 9 and 10 shows net useful flux entering molten salt for CPC and cone.

Table 11. Net useful flux (kW) entering molten salt (CPC)

Half Angle ($^{\circ}$)	12PM			10AM			7AM		
	Inlet Radius (mm)								
	650	800	950	650	800	950	650	800	950
24	120.1	123.2	123.4	81.4	86.3	87.2	5.6	5.2	4.1
25	121.6	124.3	123.9	82.4	87.4	88.2	5.6	5.1	3.9
26	122.2	124.5	123.8	82.9	87.8	88.4	5.4	4.9	3.6
27	122.4	124.4	123.4	83.2	87.9	88.4	5.3	4.6	3.2
28	122.5	124.2	123.0	83.5	88.2	88.6	5.1	4.4	2.8

Table 12. Net useful flux (kW) entering molten salt (cone)

Half Angle ($^{\circ}$)	12PM			10AM			7AM		
	Inlet Radius (mm)								
	650	800	950	650	800	950	650	800	950
26	108.5	114.1	116.2	71.7	77.2	79.4	4.3	3.8	2.7
27	112.3	117.5	118.9	74.4	79.9	81.9	4.4	3.8	2.6
28	115.4	120.0	120.8	76.8	82.2	83.9	4.5	3.8	2.4
29	117.9	121.9	122.3	78.8	84.1	85.5	4.5	3.7	2.2
30	119.8	123.3	123.3	80.4	85.5	86.6	4.5	3.6	1.9
31	121.2	124.3	123.8	81.7	86.6	87.4	4.4	3.4	1.6
32	122.3	125.0	124.1	82.6	87.4	88.0	4.3	3.2	1.3
33	123.1	125.4	124.2	83.3	88.0	88.3	4.2	3.0	0.9
34	123.7	125.6	124.2	83.8	88.3	88.4	4.1	2.7	0.5
35	124.0	125.7	124.1	84.1	88.5	88.4	3.9	2.5	0.1

3.5. Summary

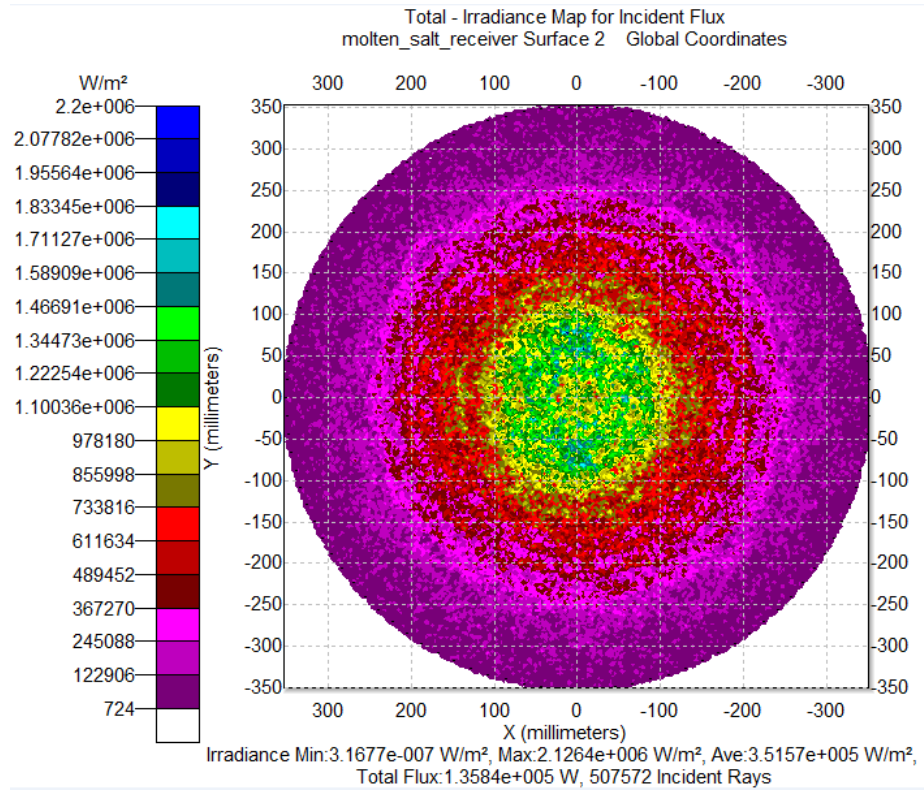
Table 13 shows optimized CPC and cone for CSPonD. Direct absorption molten salt receiver prefers a homogenous flux distribution because of possible salt degradation resulting from hot spots; in this respect the cone is better than a CPC. Figure 46 and Figure 47 show flux distribution at output of FOE for CPC and cone. Reflectivity is

95% for both cases. Cone loss is large because length has not been optimized.

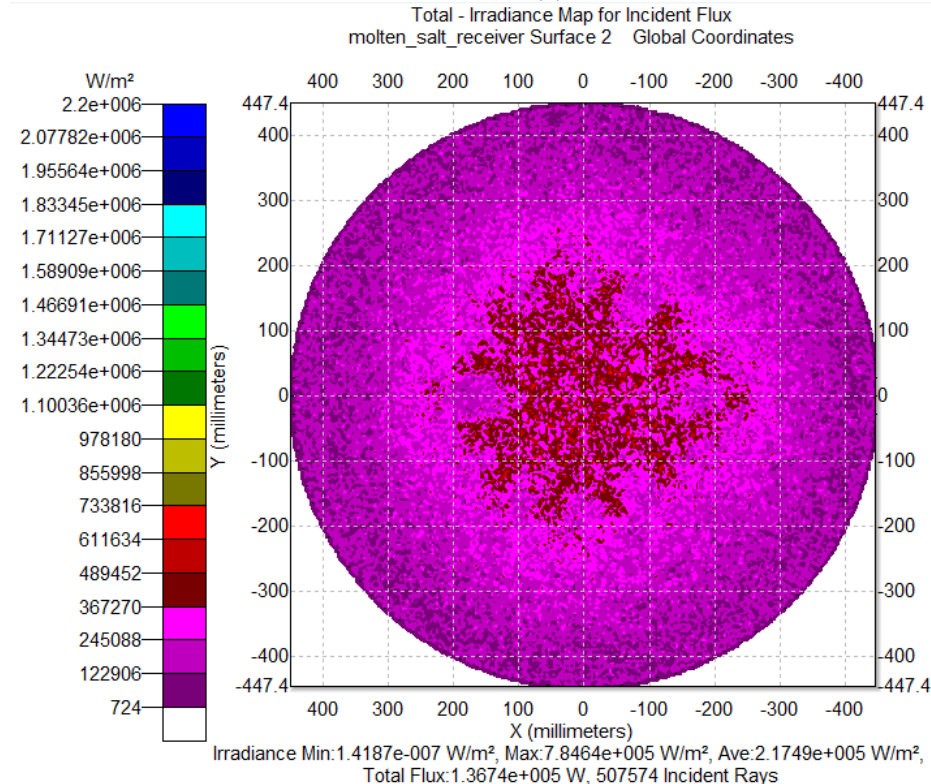
Nonetheless its performance is better than that of the CPC at 10AM and noon.

Table 13. Optimized CPC vs Cone

	CPC		CONE	
Half angle (°)	26		34	
Inlet Radius (m)	0.8		0.8	
Exit Radius (m)	0.35		0.45	
Length (m)	2.36		1.85	
Thermal Loss@600C (W)	3893		6243	
Flux Output (W)	12:00 PM	10:00 AM	12:00 PM	10:00 AM
	135842	97357	136751	98392
Flux entering molten salt (W)	128365	91668	131821	94527
Net useful flux entering molten salt (W)	124472	87775	125578	88284

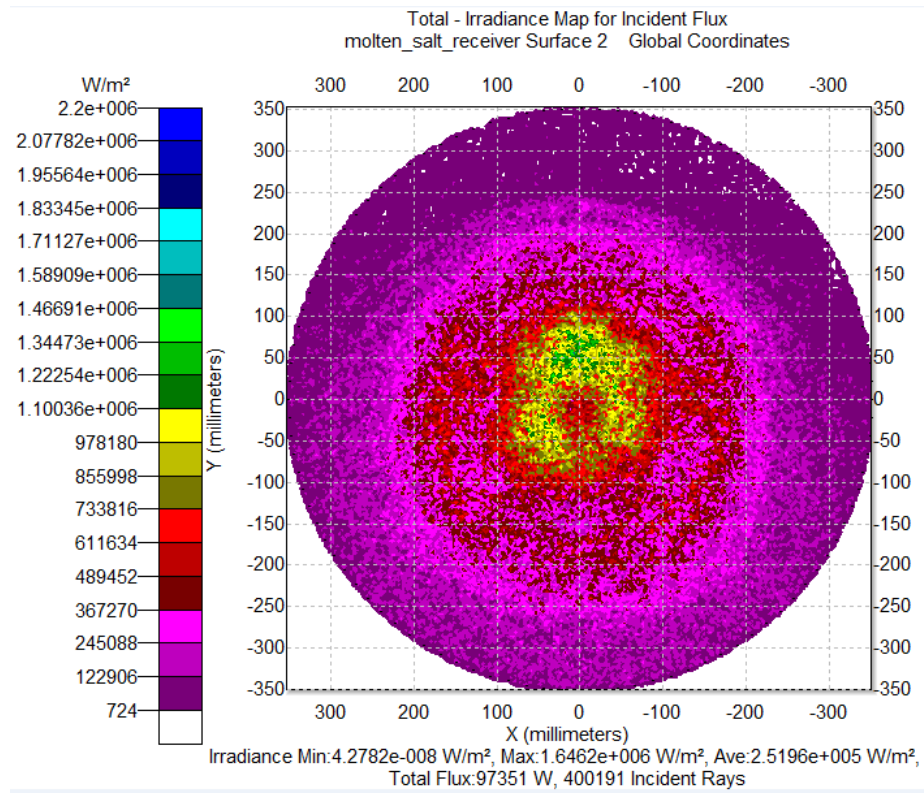


(a)

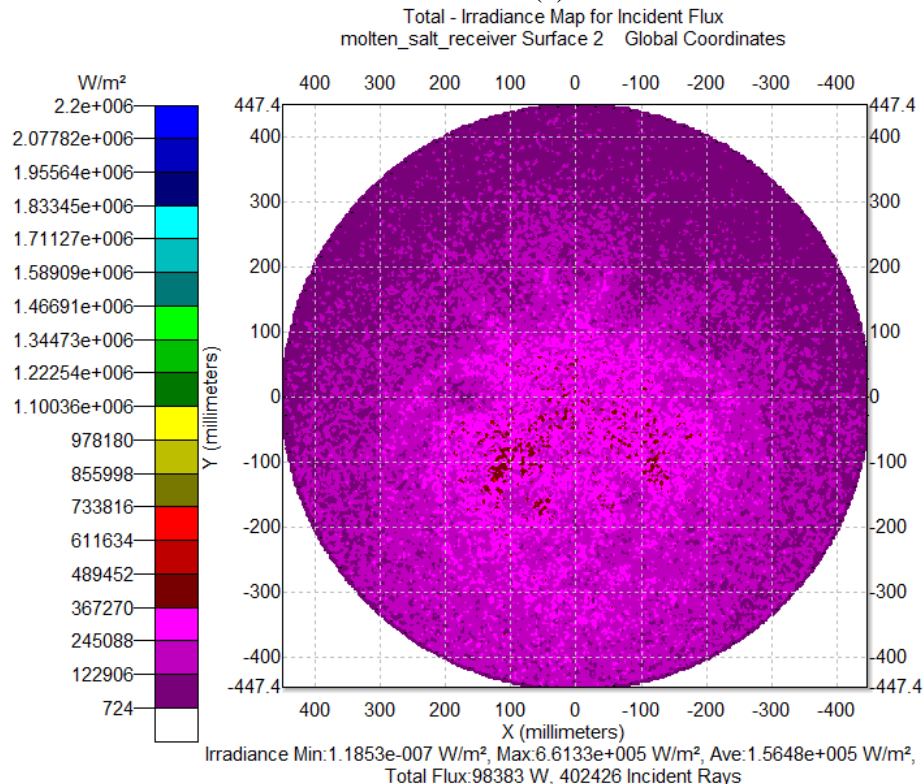


(b)

Figure 46 (a) CPC (b) cone output flux distribution at 12pm



(a)

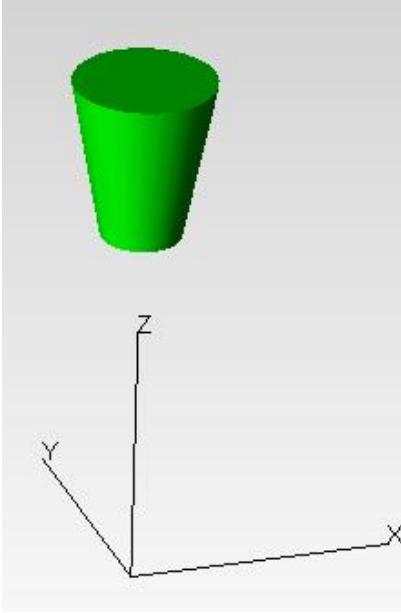
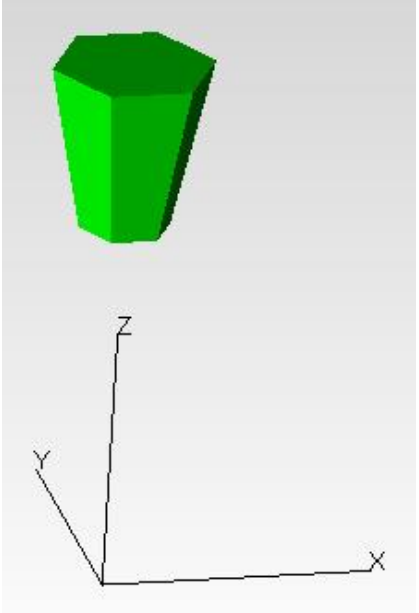


(b)

Figure 47 (a) CPC (b) cone output flux distribution at 10 AM

The cone can be further simplified to a faceted cone. Table 14, Figure 48, Figure 49, Figure 50 and Figure 51 show optical performance comparison between optimized cone and 6 faceted cone.

Table 14 Optimized cone vs 6 Faceted cone optical performance

	CONE	Faceted CONE(hexagonal)	
Geometry			
Top	Radius = 800.00 mm, Area = 2.0106e+06 mm ²	Side = 879.71 mm, Area = 2.0106e+06 mm ²	
Bottom	Radius = 447.35 mm, Area = 6.2871e+05 mm ²	Side = 491.93 mm Area = 6.2871e+05 mm ²	
Length	1.85 m	1.85 m	
	12 pm 10 am	12 pm 10 am	
Flux Inlet (kW)	142.62	103.11	142.64
Flux Output (kW)	136.7	98.38	136.07
Flux entering molten salt (kW)	131.81	94.52	131.18
			93.97

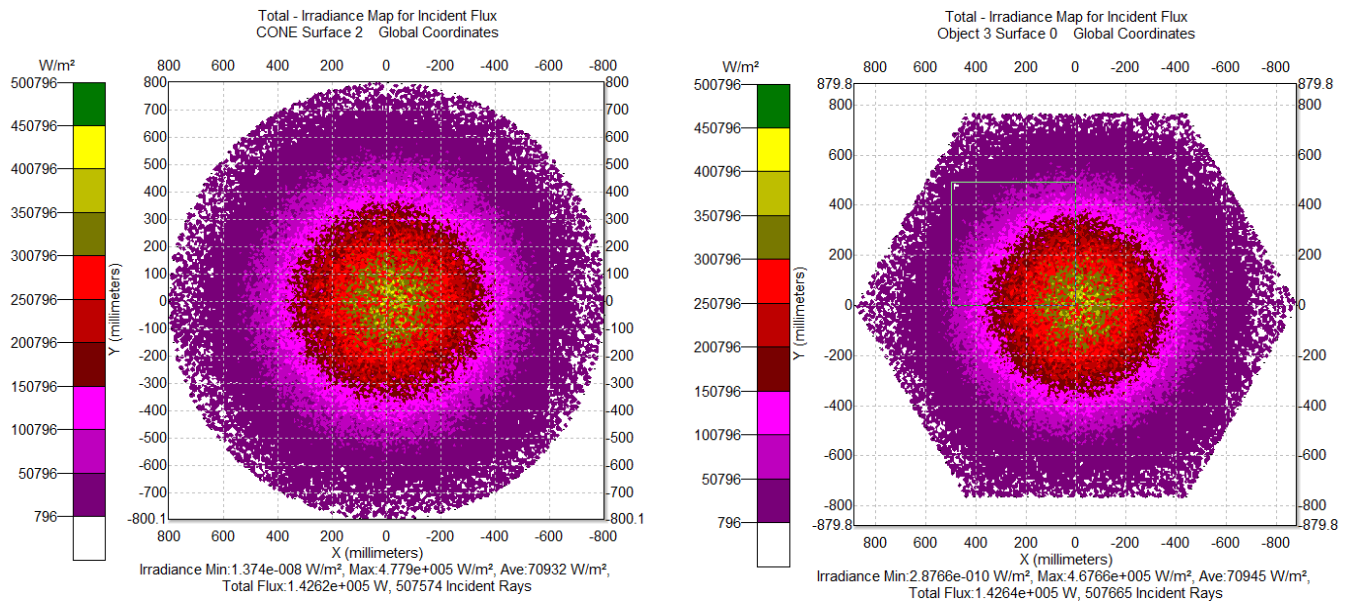


Figure 48 Cone (left) and 6 faceted cone (right) Inlet Flux at 12 pm

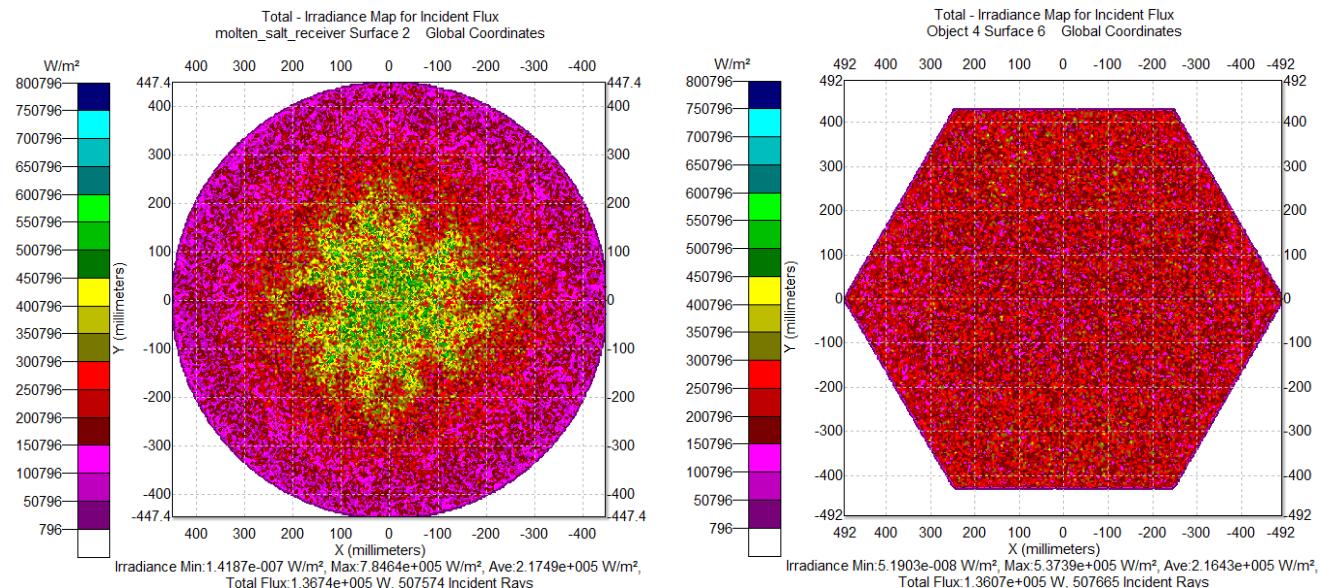


Figure 49 Cone (left) and 6 faceted cone (right) Output Flux at 12 pm⁹

⁹ Note that number of rays at inlet and outlet plane is same, but outlet flux is lower than inlet flux because of absorbed flux at reflective surface of FOE.

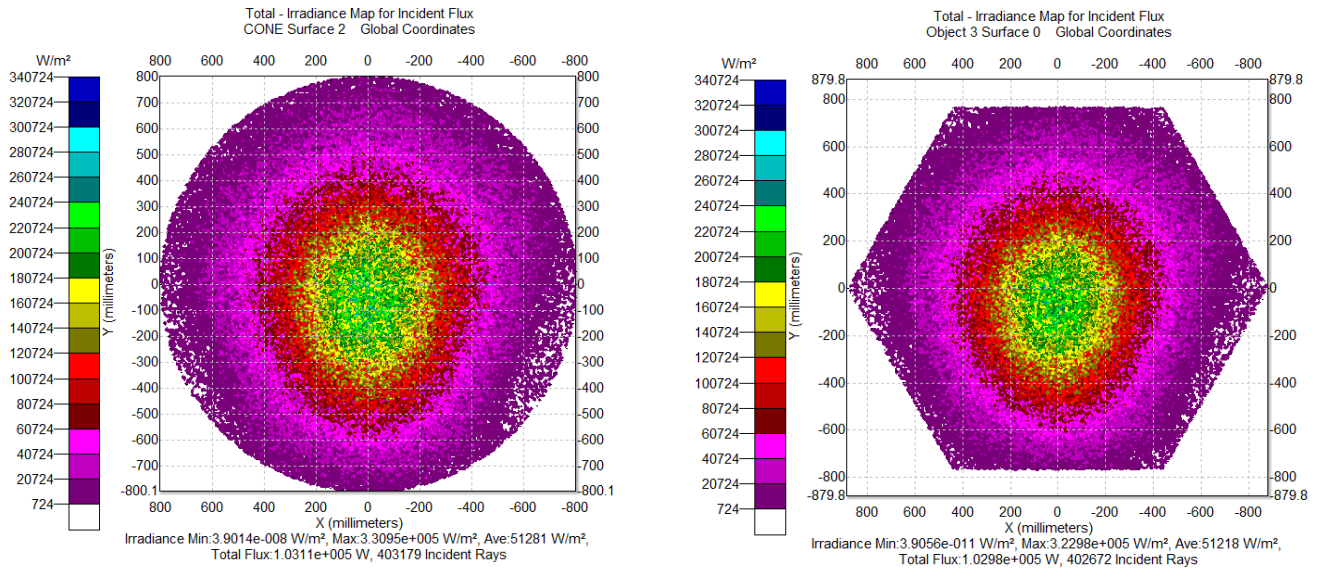


Figure 50 Cone (left) and 6 faceted cone (right) Inlet Flux at 10 am

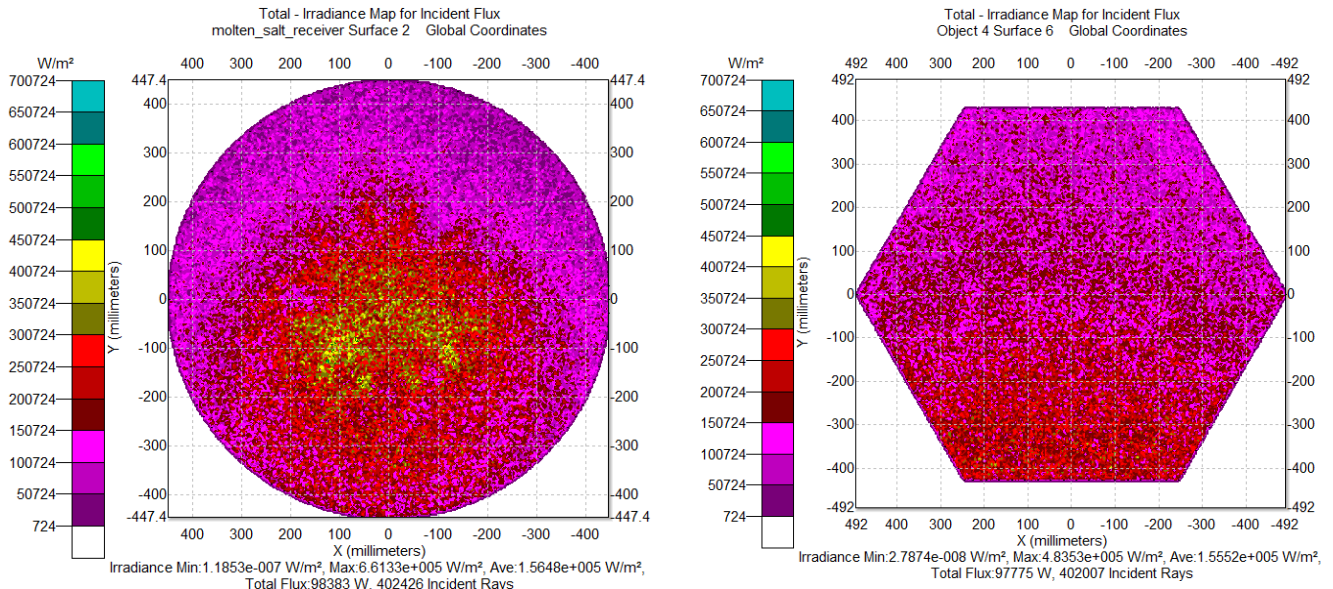


Figure 51 Cone (left) and 6 faceted cone (right) Output Flux at 10 am.

CHAPTER 4

Generalized Shape Optimization

The 2-D CPC is an ideal concentrator for collimated beam radiation whose incident angle (Figure 41) may change over $0 \leq \theta \leq \theta_{acc}$. The BDOE ray distribution is nearly radially symmetric and skewed. BDOE has a angular distribution that is roughly monotonic with radius. As reported in the previous section, our first approach for finding the best FOE was to search for the best CPC design. We found that a cone was as good as a CPC in terms of flux output. Moreover, the cone's output flux distribution was more homogenous than the CPC output flux distribution. However there is no reason to believe that a cone is the best FOE for the BDOE any more than a CPC is.

A variety of FOE design and receiver types have the following common features appropriate for the BDOE geometry.

- I. Reflector is surface and revolution about Z axis
- II. Inlet aperture at top
- III. Outlet aperture at bottom

These features are shown schematically in Figure 52.

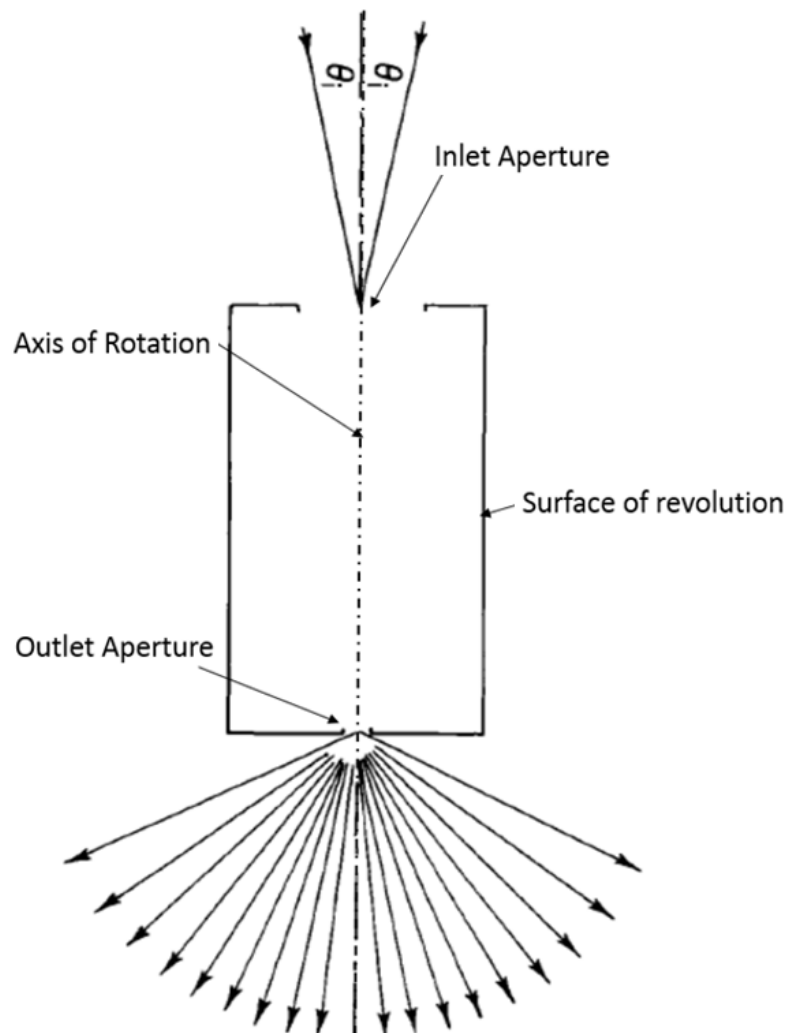


Figure 52 Common feature of FOE Element

In general following parameters are to be optimized:

- I. Inlet Radius (R_{in})
- II. Inlet elevation (Z_{in})
- III. Outlet Radius (R_{out})
- IV. Outlet elevation (Z_{out})
- V. Surface of revolution profile
- VI. Central ray convergence point plane (Z_{CRC})

To find an optimal FOE geometry, an objective function must be defined. The main project objective is to maximize receiver output at a given temperature. This involves tradeoffs between concentration, optical efficiency, and aperture size. Other considerations pertinent, as previously mentioned, to CSPonD, include flux uniformity across the aperture area and near normal incidence of flux at the molten salt surface.

The thermal loss model, which reflects receiver type, area and temperature, is documented in Appendix E.

4.1. Methodology

The TracePro 2D Interactive Optimizer can search over a predefined solution domain. It uses the Downhill Simplex, also known as Nelder-Mead, method for optimization. The Downhill Simplex method is a local optimizer that converges to the local minimum solution (usually) closest to the starting point. During an optimization we have some control of the process and can monitor interim solutions. We can stop the optimizer, change the initial starting parameters, and then re-start the optimization.

Using the Interactive Optimizer, we can sketch a profile in one or two cross-sections. As a starting point, specify variables and a target, and the optimizer will vary the design to best meet the objective.

Figure 53 shows a general setup defined in TracePro 2D Interactive Optimizer; Segments can be defined as lines, splines, etc. A segment point can have two degrees of freedom (range of upper and lower bound for each degree of freedom). When a segment is defined as a spline, a control point can be defined within the segment.

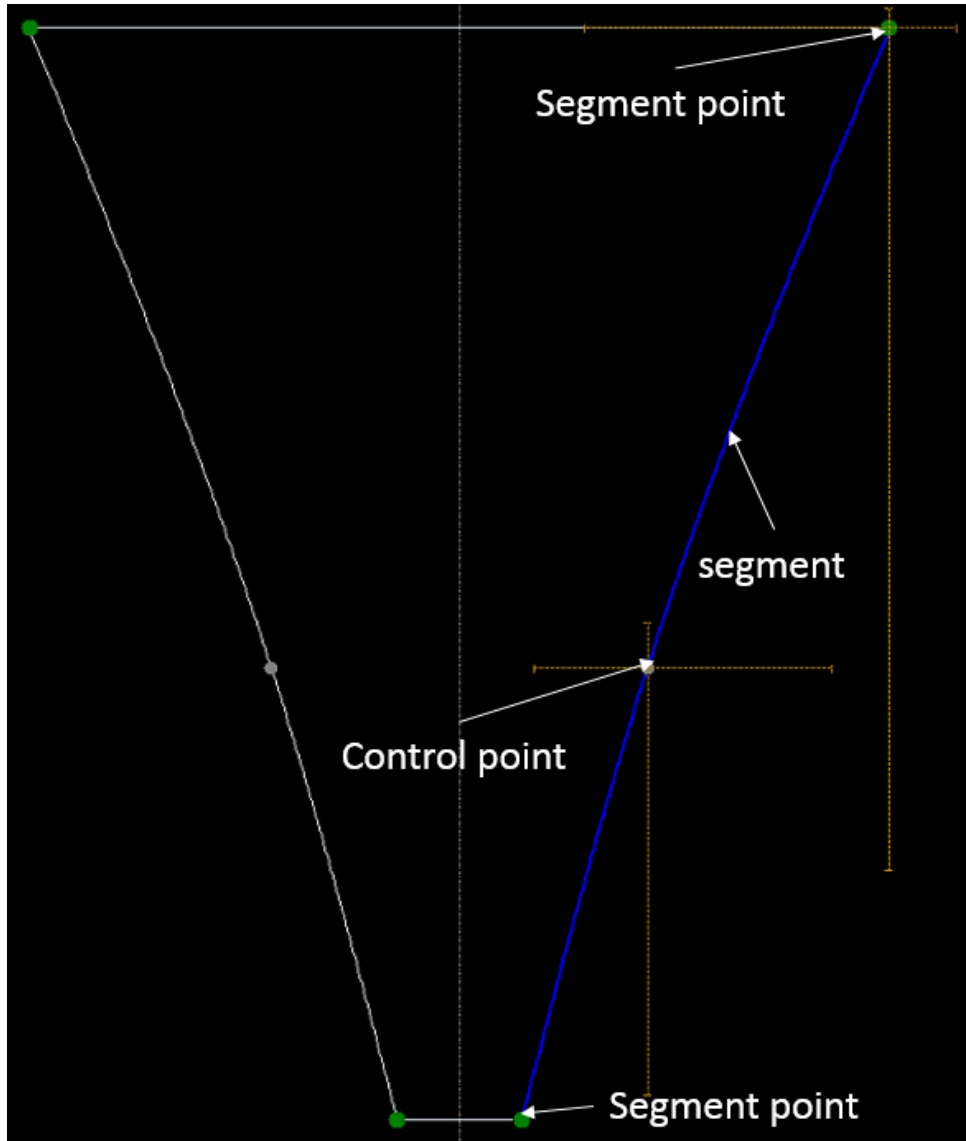


Figure 53. TracePro 2D interactive optimizer general setup¹⁰

4.2. Optimization of cone (CSPonD)

The TracePro 2D Interactive optimizer provides a means to further optimize the cone (crudely optimized in section 3.6) by reducing its output radius (as it has larger radius than optimized CPC, leads to higher thermal losses). Here outlet radius has been fixed to 350 mm, and its elevation has been varied with respect to central ray convergence

¹⁰ When objective function for optimization was high flux BDOE FOE output, it has been found that 2D profile shapes tends to be like simple cone (slightly trumpet like Figure 53).

point plane at (6 m). Table 15 shows different starting points and optimized solutions for inlet radius and elevation.

In this example the FOE reflectivity of cone used here is 80%. The cone shown in Table 13 (Chapter 3) which had a 95% reflectivity would have had a flux of 116 kW entering in the molten salt at 80% reflectivity.

Table 15. Cone optimization for CSPonD receiver with $Z_{CRC} = 6000\text{mm}$ and outlet radius = 350mm¹¹.

Outlet elevation $Z_{out}(\text{mm})$	starting point		optimized		Flux entering molten salt (kW)	Length (mm)
	Inlet radius R_{in} (mm)	Inlet elevation Z_{in} (mm)	Inlet radius R_{in} (mm)	Inlet elevation Z_{in} (mm)		
4150	800	6000	753	6737	102	2587
	900	6000	759	6776	102	2626
	900	6000	755	6778	102	2628
4500	800	6000	764	6819	106	2319
	900	6500	778	6899	106	2399
5000	900	6500	830	7128	112	2128
5500	900	6500	927	7505	118	2005
5600	900	6500	957	7608	119	2008
5650	900	7000	966	7630	120	1980
5700	900	7000	996	7726	120	2026
	800	6500	1017	7785	120	2085
	990	7700	995	7725	120	2025
5750	945	7500	1068	7919	121	2169
	900	7000	945	7536	121	1786
	900	7000	1114	8059	121	2309
5900	900	6500	1294	8500	122	2600
	1000	7000	1285	8495	122	2595
6000	900	7000	1224	8299	123	2299
	1000	7500	1294	8498	123	2498

¹¹ Purpose of this to find best possible CONE, not best profile.

CHAPTER 5

Conclusion And Future Work

5.1. Conclusion

There are two main objectives of this thesis. First, to better understand BDOE performance, a parametric optical model was needed which can predict BDOE output in conjunction with different kinds of receivers. Second a final optical element (FOE) was designed that, coupled with the BDOE, provide high concentration and optical efficiency for various types of receivers

A Matlab script has been developed to create the BDOE optical model represented by a TracePro Scheme file. The Script is parametric, with main parameters being location (Latitude and Longitude), date and time (sun positions), etc. The Script has been written keeping in mind that new features can be added easily. More generally, an extensible method for modelling and analysis of BODE optics was developed. This methodology could be helpful in identifying any current/future problems in the heliostat field easily, whether they result from design problems or flexible implementation issues like canting or optical alignment problems.

A final optical element has been designed for the CSPonD Demo project. CSPonD has a direct absorption molten salt receiver that will result in high FOE surface temperatures. A homogenous flux distribution was required because of possible salt degradation therefore the cone is better than the CPC. A 6-faceted cone is cheap to build and allows for easy replacement of facets. Figure 54 shows the first prototype FOE manufactured for the CSPonD demonstration experiment.



Figure 54 CSPonD demo final FOE assembly design and manufactured¹² FOE.

5.2. Future Work

The Beam-Down solar concentrator is a one-of-a-kind facility in terms of the optical design of the plant and the heliostat field. The ability test several receiver concepts, heliostat designs, reflective surfaces, etc., makes the Beam-Down plant an important test facility. This thesis has mainly looked at methodology to optically model a solar concentrating system using generalized ray tracing software (TracePro) and how to

¹² Mechanical design is done by Dr. Benjamin Grange.

design the FOE for CSPonD. A number of useful extensions could be modeled to more fully explore beam down optics and FOE design.

Validation of BDOE Optical Model:

TracePro optical model should be validated through experiments in BDOE. There could be three main area which need verification 1) geometrical specification like canting angle, canting error etc. 2) optical specification of HS and CR like reflectivity, slope error, spectral response etc. 3) Source has been modeled a simple as solar disc. The circumsolar radiation effect should be checked and quantified in BDOE optical model.

Once TracePro Optical model is thoroughly validated it can be used for analyzing beam down optics. Off-axis aberration and control behavior with spinning-axis heliostat design and correction of off-axis aberration are two of many possible variations of BDOE optics that could be assessed. Other examples include tighter packing of CR facets and a larger (or smaller) central reflector (optimal size).

Various empirical relationship for beam down system can be explored using Curve fitting to the component optical efficiency data points.

Different heliostat canting arrangements should be explored to minimize spillage at CR. Shading and blocking due to CR canting can be studied for different CRC heights (which result into different CR cantings).

FOE Optimization:

When objective function for optimization was high flux BDOE FOE output, it has been found that 2D profile shapes tends to be like simple cone. But more rigorous optimization should be done for finding FOE profile in bigger solution domain with different objective functions (different objective function could be because of different

project requirements like high type rather than high flux or different receiver configuration like vertical cylinder receiver etc.). To more fully optimize FOE design, and its integration with a given beam-down configuration, it will be essential to speed up optimization by finding out which design parameters are most important and/or interactive. Computational improvements should also be explored.

With improved optimization speed and convergence it should be possible to properly optimized multi-segment profiles as well as inlet and outlet radii and elevations. Also the A-, B- and C-ring central-ray convergence heights can be independently optimized.

APPENDIX A

Canting Angle

Inclination angle of heliostat mirrors

Figure 55 shows the heliostat facet layout and their respective IDs as described in TiTech documentation (D-4-2). CC4 is the control mirror which is set at the center panel. Facet size is 45 cm square except CB4 and CF4. CB4 and CF4 are half sized (45 cm *22.5 cm). Inclination angle of facet was measured by difference of height at the points of CH1, CH2, CH3 and CH4. These points are distant by 15 mm from the edge. Here, S1=Ch1-Ch2; S2=Ch3-Ch4; S3=Ch1-Ch3; and S4=Ch2-Ch4. The elevation canting angles are given by

$$\theta_y = \tan^{-1} \left(\frac{S_1 + S_2}{2 * (450 - (15 + 15))} \right) \quad (29)$$

and the azimuth canting angles are given by

$$\theta_x = \tan^{-1} \left(\frac{S_3 + S_4}{2 * (450 - (15 + 15))} \right) \quad (30)$$

Measured values of S1, S2, S3 and S4 are reported for every facet of each heliostat [MES]. By using equation 29 and 30 the canting angle can be calculated.

Ch1 Ch3	Ch2 Ch4												
BB1		BB2		BB3		BB4		BB5		BB6		BB7	
Ch3 Ch3	Ch4 Ch4												

Ch1 Ch3	Ch2 Ch4												
CB1		CB2		CB3		CB4		CB5		CB6		CB7	
Ch3 Ch3	Ch4 Ch4												
Cr1 Ch1	Ch2 Ch2	Ch1 Ch3	Ch2 Ch4										
CF1		CF2		CF3		CF4		CF5		CF6		CF7	
Ch3 Ch3	Ch4 Ch4												

Ch1 Ch3	Ch2 Ch4												
FB1		FB2		FB3		FB4		FB5		FB6		FB7	
Ch3 Ch3	Ch4 Ch4												
Ch1 Ch3	Ch2 Ch4												
FF1		FF2		FF3		FF4		FF5		FF6		FF7	
Ch3 Ch3	Ch4 Ch4												

Figure 55 Identification of heliostat facets.

Proper canting angles are tabulated in the following Table 16:

Table 16. Canting angle (degree) of A, B and C type HS

ID		A		B		C	
TiTech	Used	θ_x	θ_y	θ_x	θ_y	θ_x	θ_y
BB1	1	-1.69	-1.89	-1.38	-1.7	-1.11	-1.5
BB2	2	-1.69	-1.26	-1.38	-1.13	-1.11	-1
BB3	3	-1.69	-0.63	-1.38	-0.57	-1.11	-0.5
BB4	4	-1.69	0	-1.38	0	-1.11	0
BB5	5	-1.69	0.63	-1.38	0.57	-1.11	0.5
BB6	6	-1.69	1.26	-1.38	1.13	-1.11	1
BB7	7	-1.69	1.89	-1.38	1.7	-1.11	1.5
BF1	8	-1.05	-1.89	-0.82	-1.7	-0.61	-1.5
BF2	9	-1.05	-1.26	-0.82	-1.13	-0.61	-1
BF3	10	-1.05	-0.63	-0.82	-0.57	-0.61	-0.5
BF4	11	-1.05	0	-0.82	0	-0.61	0
BF5	12	-1.05	0.63	-0.82	0.57	-0.61	0.5
BF6	13	-1.05	1.26	-0.82	1.13	-0.61	1
BF7	14	-1.05	1.89	-0.82	1.7	-0.61	1.5
CB1	15	-0.32	-1.89	-0.28	-1.7	-0.25	-1.5
CB2	16	-0.32	-1.26	-0.28	-1.13	-0.25	-1
CB3	17	-0.32	-0.63	-0.28	-0.57	-0.25	-0.5
CB4	18	-0.32	0	-0.28	0	-0.25	0
CC4	19	0	0	0	0	0	0
CF4	20	0.32	0	0.28	0	0.25	0
CB5	21	-0.32	0.63	-0.28	0.57	-0.25	0.5
CB6	22	-0.32	1.26	-0.28	1.13	-0.25	1
CB7	23	-0.32	1.89	-0.28	1.7	-0.25	1.5
CF1	24	0.32	-1.89	0.28	-1.7	0.25	-1.5
CF2	25	0.32	-1.26	0.28	-1.13	0.25	-1
CF3	26	0.32	-0.63	0.28	-0.57	0.25	-0.5
CF5	27	0.32	0.63	0.28	0.57	0.25	0.5
CF6	28	0.32	1.26	0.28	1.13	0.25	1
CF7	29	0.32	1.89	0.28	1.7	0.25	1.5
FB1	30	1.05	-1.89	0.82	-1.7	0.61	-1.5
FB2	31	1.05	-1.26	0.82	-1.13	0.61	-1
FB3	32	1.05	-0.63	0.82	-0.57	0.61	-0.5
FB4	33	1.05	0	0.82	0	0.61	0
FB5	34	1.05	0.63	0.82	0.57	0.61	0.5
FB6	35	1.05	1.26	0.82	1.13	0.61	1
FB7	36	1.05	1.89	0.82	1.7	0.61	1.5
FF1	37	1.69	-1.89	1.38	-1.7	1.11	-1.5
FF2	38	1.69	-1.26	1.38	-1.13	1.11	-1
FF3	39	1.69	-0.63	1.38	-0.57	1.11	-0.5
FF4	40	1.69	0	1.38	0	1.11	0
FF5	41	1.69	0.63	1.38	0.57	1.11	0.5
FF6	42	1.69	1.26	1.38	1.13	1.11	1
FF7	43	1.69	1.89	1.38	1.7	1.11	1.5

Each HS has three banks/panels (Front (F), Middle/Center (C), Rear/Back (B)).

Shaft Tilt: According to the BDOE HS design [36] the inclination angles (canting) are modified by the so-called *shaft tilt*, which is different for the A, B, and C-line. The canting angles are given in Table 16 with respect to each bank frame. In addition to these facet canting angles there is additional inclinations of front and back panels frame by *shaft-tilt* angles of A-Line: 1.37° , B-Line: 1.10° , and C-Line: 0.86° as shown in Figure 56.

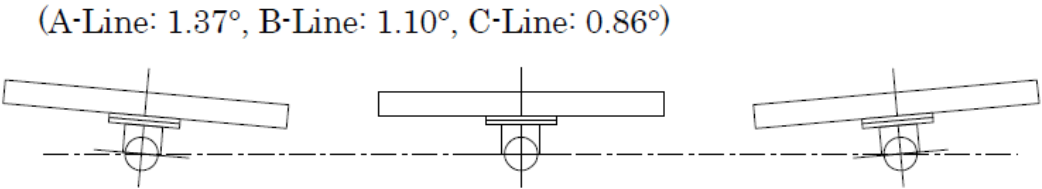


Figure 56 Frame mounting angle (shaft tilt)

When the shaft tilt is accounted for, effective canting angle changes. Therefore flux distribution pattern as well as flux intercept at CRC plane also changes (refer to Figure 57, Figure 58, Figure 59, Figure 60 and Figure 61)¹³.

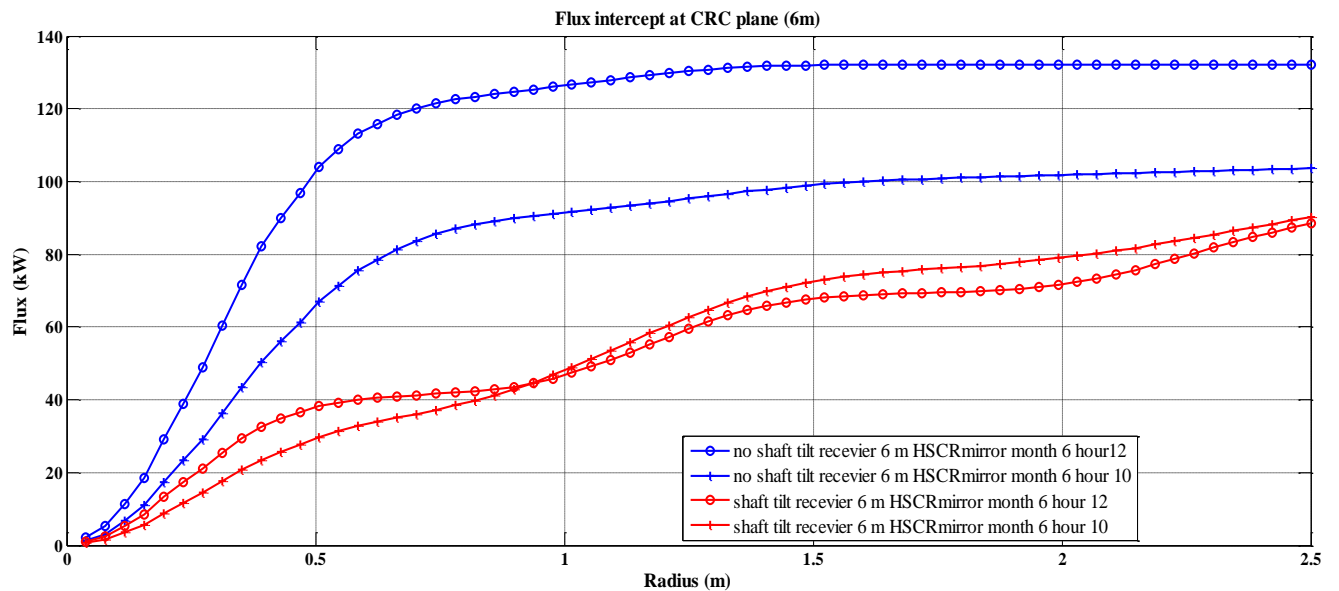


Figure 57 Flux intercept at CRC plane

¹³ This uses HSmirror and CRmirror reflectivity dependent on incident angle as shown in Figure 68. DNI used for 12 PM and 10 AM are respectively 796 and 724.5 W/m^2 . All the calculations in chapter 2, 3 and 4 assume no shaft tilt condition (i.e. shaft tilt= 0 for A, B and C lines).

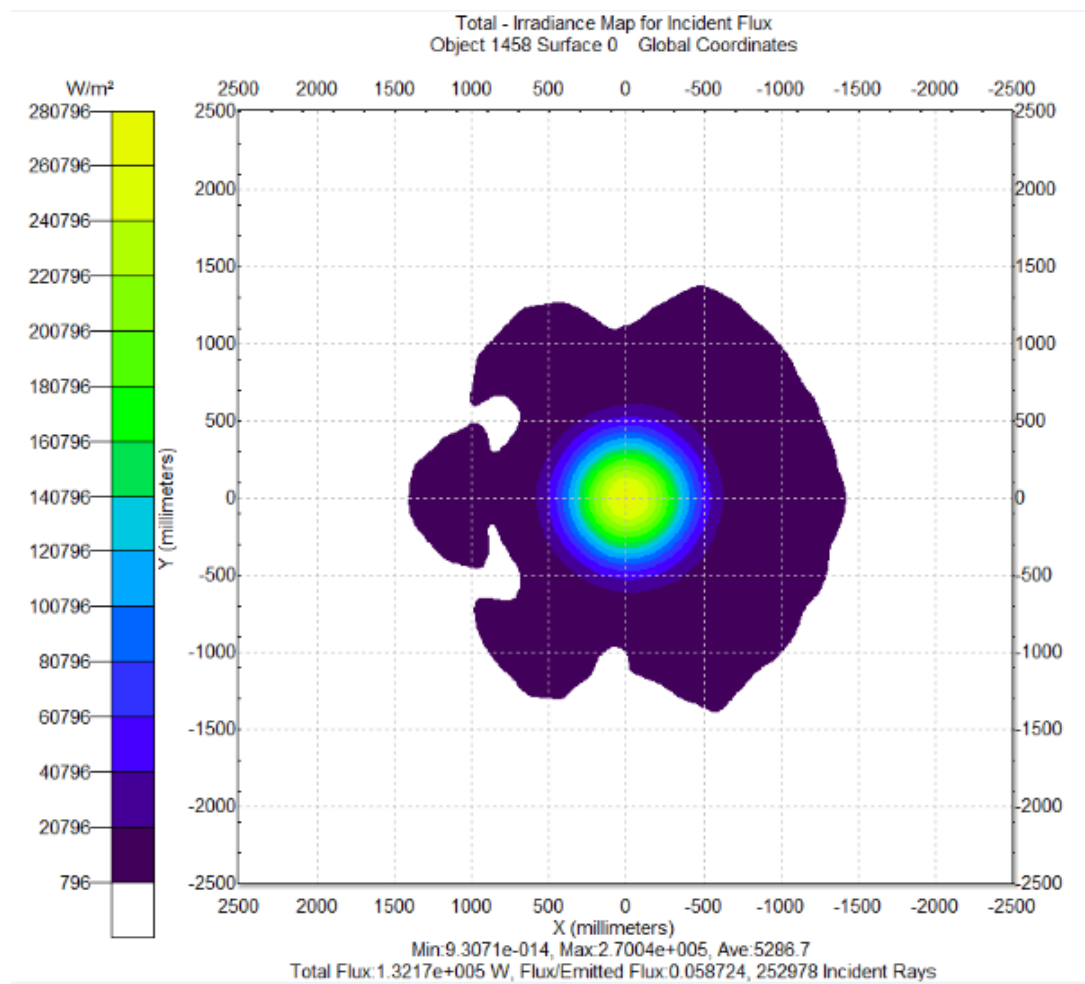


Figure 58 CRC plane flux distribution at 12pm (June) with no shaft tilt.

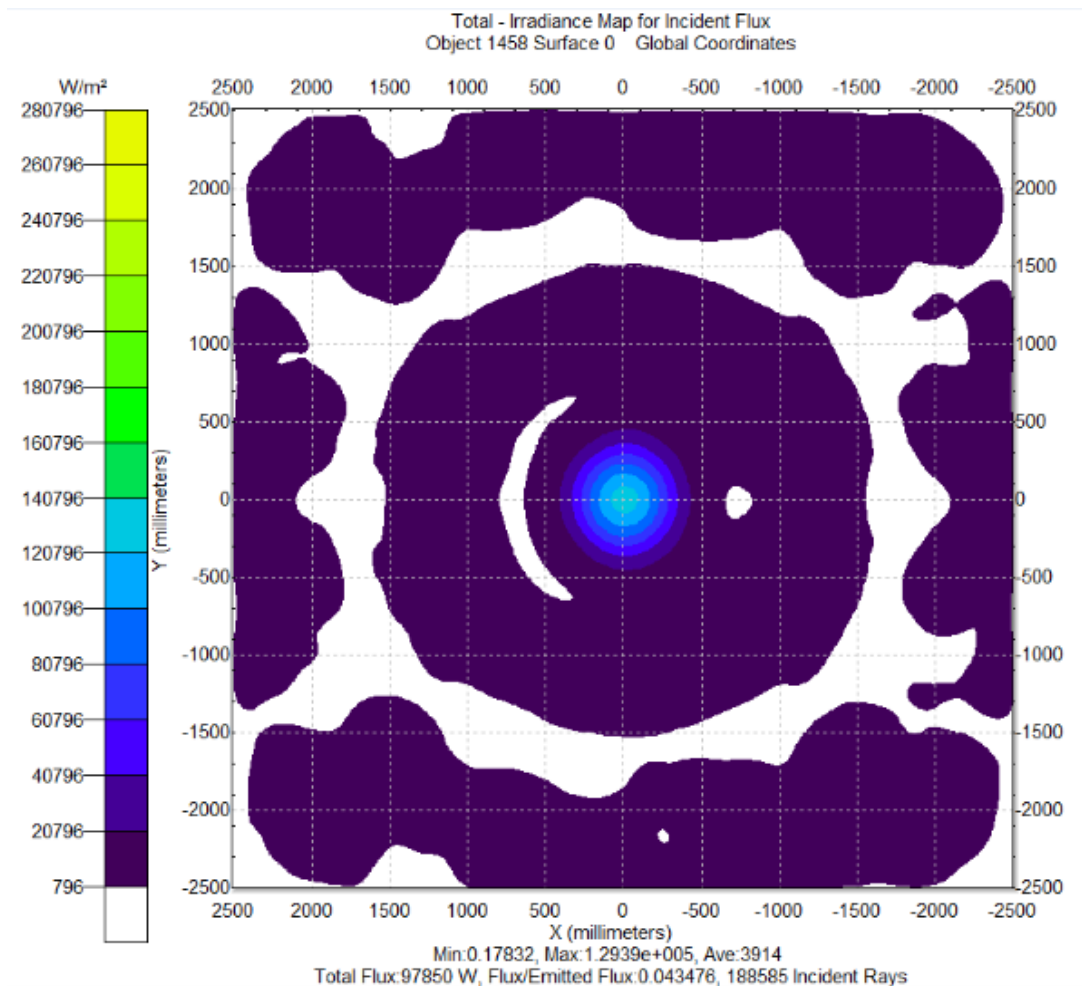


Figure 59 CRC plane flux distribution at 12pm (June) with shaft tilt

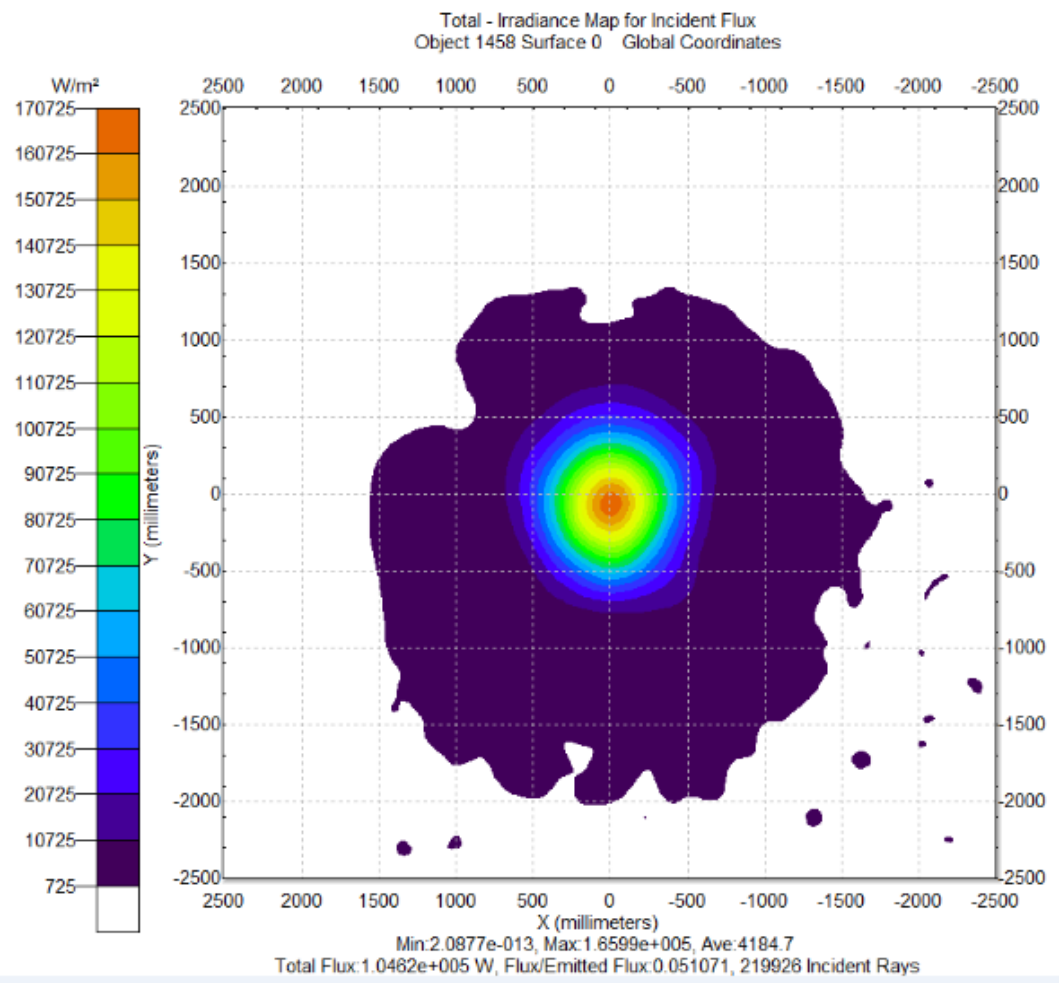


Figure 60 CRC plane flux distribution at 10 AM (June) with no shaft tilt.

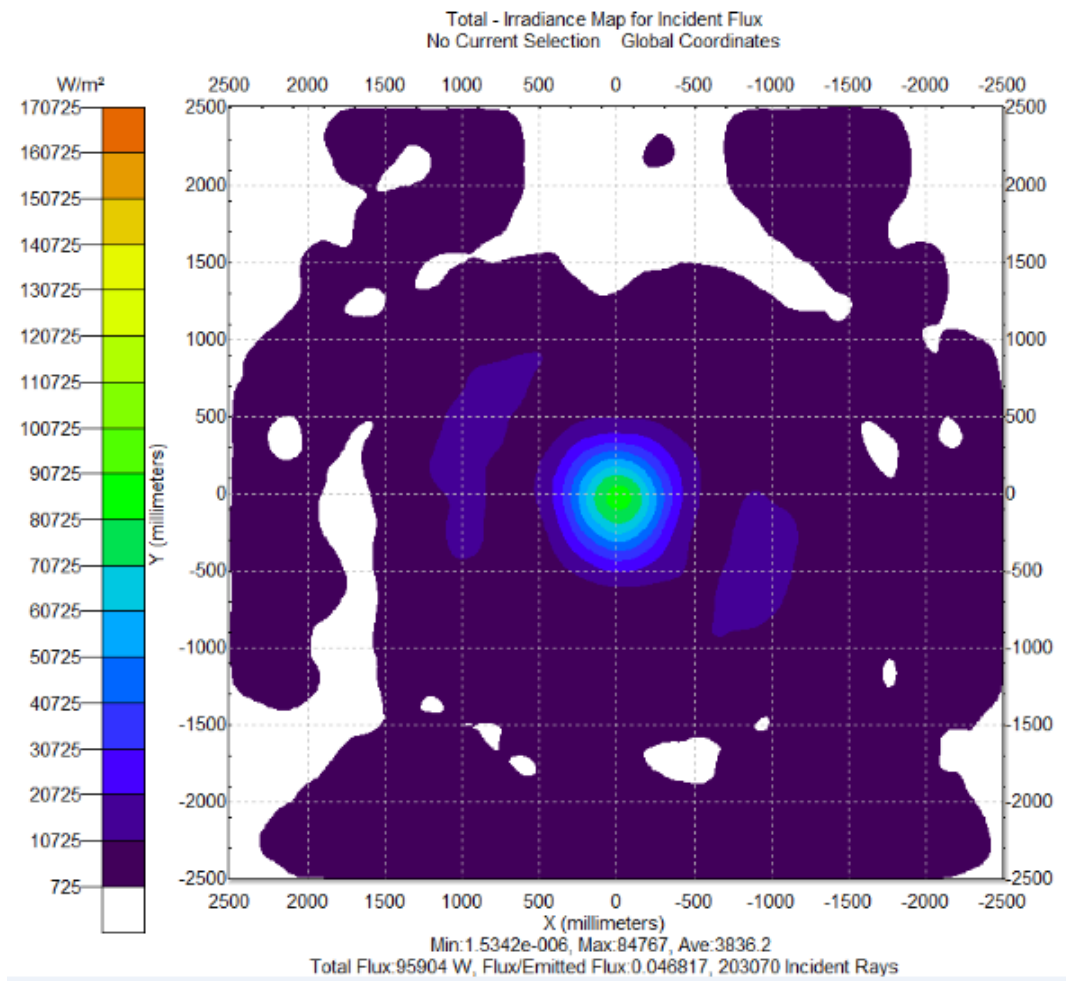


Figure 61 CRC plane flux distribution at 10 AM (June) with shaft tilt

APPENDIX B

Canting Error

For each of 1419 heliostat facets a tilt measurement was made at the time of heliostat installation. These measurements should need to be checked periodically because the canting errors can change over time. The canting error distribution at the time of the MES measurements is nevertheless useful because it gives an idea of the canting error distribution to be expected of faceted heliostats in practice. For the type of facet used in Masdar's BDOE—float glass with a relatively high thickness-to-width ratio of >0.01—it is believed that the HS slope error is dominated by facet canting error.

Mirror Facet gradient angle / Mirror No.& Design DATA

A-Line A1

Panel Frame Gradient Angle		Panel Frame Gradient Angle		Panel Frame Gradient Angle	
1.37		0.00		0.00	
BACK		BB4	1.69 1.90	BB6	1.69 1.25
		BB5	1.69 1.25	BB7	1.69 1.70
		BF4	1.05 1.05	BF6	1.05 1.05
		BF5	1.05 1.05	BF7	1.05 1.05
		CB4	0.00 0.05	CB6	0.00 0.05
		CB5	0.00 0.05	CB7	0.00 0.05
		CF4	1.05 1.05	CF6	1.05 1.05
		CF5	1.05 1.05	CF7	1.05 1.05
		CB1	1.69 1.65	CB2	1.26 1.20
		BF1	1.05 0.95	BF2	1.26 1.20
		CB3	1.69 1.70	CF2	1.26 1.20
		CF3	1.05 1.05	FB3	1.26 1.20
		CB4	0.00 0.00	FB4	1.05 1.05
		CB5	0.00 0.00	FB5	1.05 0.95
		CF4	0.00 0.00	FB6	1.05 1.05
		CF5	0.00 0.00	FB7	1.05 1.05
LINK ARM SIDE		CF1	0.32 0.35	FB1	1.05 1.20
CENTER		CB2	0.32 0.35	FB2	1.26 1.20
ELEVATION		CB3	0.32 0.30	FB3	1.05 1.10
MOTOR SIDE		CB4	0.00 0.05	FB4	1.05 1.00
FRONT		CB5	0.00 0.05	FB5	1.05 0.95
		CF1	0.32 0.25	FB1	1.69 1.25
		CF2	0.32 0.20	FB2	1.26 1.20
		FB1	1.05 1.20	FB3	1.26 1.20
		FB2	1.26 1.20	FB4	1.05 1.05
		FB3	1.05 1.10	FB5	1.05 1.05
		FB4	1.05 1.00	FB6	1.05 1.05
		FB5	1.05 0.95	FB7	1.05 1.05
		FF1	1.69 1.25	FF2	1.26 1.20
		FF3	1.69 1.75	FF4	1.69 1.65
		FF5	1.69 1.65	FF6	1.69 1.75
		FF7	1.69 1.70		

Figure 62. Heliostat A1 facet tilt measurement (handwritten numbers) along with required values

Panel Frame Gradient Angl			Panel Frame Gradient Angl		
1.37			0.00		
0.00 0.00	0.63 0.65	1.26 / 1.25	0.00 0.00	0.32 0.25	1.89 / 1.90
BB4 / 1.69 1.90	BB5 / 1.69 1.75	BB6 / 1.69 1.25	CB4 / 0.00 0.00	CB5 / 0.63 0.65	CB6 / 0.32 0.25
BB7 / 1.69 1.70	BF4 / 1.05 1.05	BF5 / 1.05 1.05	CC4 / 0.00 0.05	CF4 / 0.63 0.65	CF5 / 0.32 0.35
BACK					ELEVATION MOTOR SIDE
0.00 0.05	0.63 0.65	1.26 / 1.25	0.00 0.05	0.32 0.25	0.32 0.40
BB4 / 1.69 1.90	BB5 / 1.69 1.75	BB6 / 1.69 1.25	CB4 / 0.00 0.00	CB5 / 0.63 0.65	CB6 / 0.32 0.25
BB7 / 1.69 1.70	BF4 / 1.05 1.05	BF5 / 1.05 1.05	CC4 / 0.00 0.05	CF4 / 0.63 0.65	CF5 / 0.32 0.40

Figure 63. Close-up of left top corner in Figure 62

The required and measured values of azimuth canting and elevation canting were carefully transferred to an Excel file (canting error.xls).

Canting angle errors were calculated by subtracting the measured value from the canting angle designed values (Table 16). Signed errors are represented in Figure 64 as cumulative distributions and summarized in Table 17.

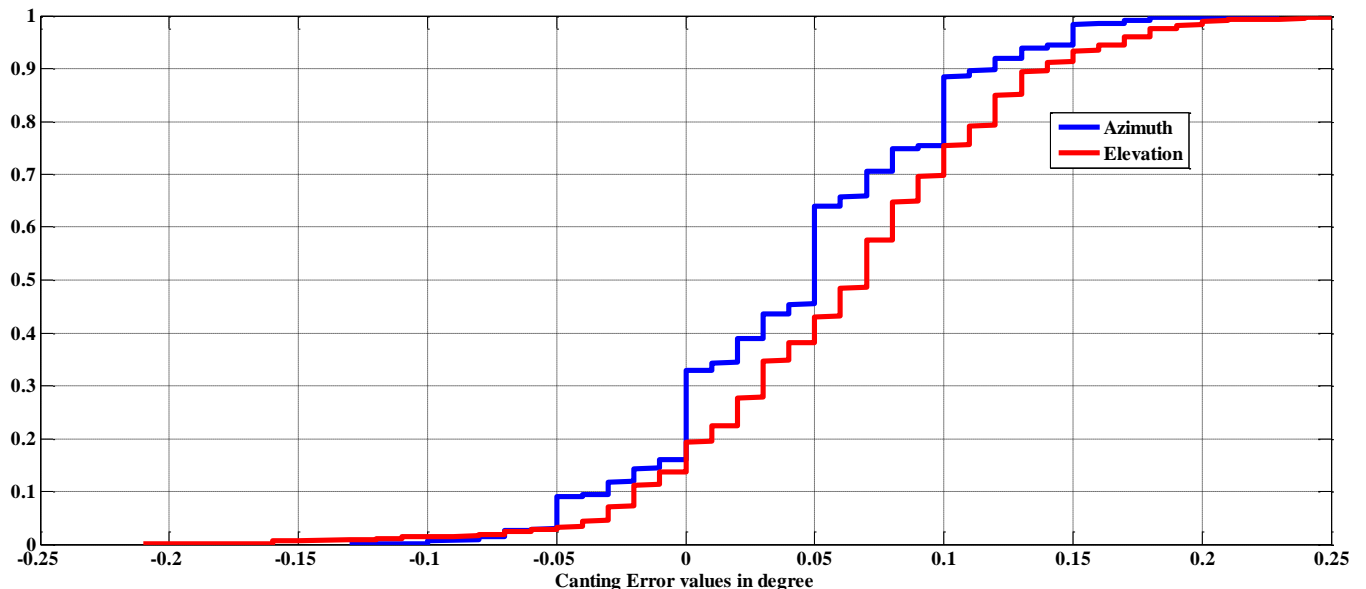


Figure 64 Cumulative distribution of canting error values in degrees N=1419

Table 17 Mean , standard deviation and Median of canting error

	Mean (degree)	Stdev (degree)	Median (degree)
Azimuth	0.0431	0.0578	0.0500
Elevation	0.0622	0.0648	0.0700

APPENDIX C

Reflectivity Measurements and Models

Measurement device used by TiTech was GM-268 of Konica Minolta .It can measure reflectivity for incident angles of 20° , 60° and 85° . Table 18 reports the statistics of measurement (refer Table 19 and Table 20 for detail).

Table 18 Summary of HS and CR reflectivity

Item	Incident angle	Reflectivity
CR	20	93.4-93.7 (average)
		2.25-2.33(stdev)
CR	60	88.9-89.3 (average)
		1.71-1.91(stdev)
HS	20	75.1 (average)
		3.80(stdev)
HS	60	59.0 (average)
		3.53(stdev)

CR average reflectivity range has been mentioned because, it has been measured for 5 points as shown in Figure 66 (refer TiTech document D-3-2 for detail).

Table 19. Measured reflectivity of CR; each value is average of the five points shown in Figure 66.

	1		2		3		4		5	
	20	60	20	60	20	60	20	60	20	60
a1	93.1	87.3	94.4	88.8	92.3	86	93.6	88	93	86.8
a1.5	90.8	87.6	90.5	87.9	90.4	88.2	90.4	87.8	89.6	86.9
a2	92.2	87.7	92.4	87.6	93.2	87.5	93	87.6	92.7	87.4
a3	91.4	86.6	91	85.8	92.8	86.6	92.2	86.5	91.9	86.4
a3.5	90.9	87.7	89.8	85.6	89.6	87.6	89.7	86.6	90.4	88.1

a4	92.1	87.6	92.1	87.4	93	87.4	92.3	86.9	91.8	86.4
a5	95.6	92.1	95.9	92.1	95.9	92.2	95.1	92	95.1	92
a5.5	90.9	87.8	91.2	87.9	90.2	88.4	90.2	88	90.3	87.9
a6	94.9	91.4	95.9	92.3	95.9	92.3	94.7	91.7	95	91.9
b1	96.2	88.5	96.1	89.1	95.9	89.6	96.4	89.4	96.5	89.2
b2	95.7	90.2	94.5	89.5	95.3	91	95.4	90.7	95.1	90.7
b3	95.9	91	95.3	90	95.3	90.8	95.1	90.4	95.6	90.8
b4	95.7	90.5	95.5	90.3	95.3	91.1	95.7	91	95.7	91.2
b5	96	91.1	96.1	91	95.8	91	95.7	91.1	95.7	91.2
b6	95.8	90.6	95.5	90.3	95	90.5	95.2	90.6	95.2	90.7
b7	95.6	90.3	95.3	90.2	95.2	90.5	95	90.4	95.2	91
b8	92.7	88.8	92.3	88	93.4	88.1	93	87.1	92.7	86.7
b9	91.1	86.5	92	87.5	93.1	87.5	91.7	86.7	92.4	87.1
b10	93.2	88.4	94.1	89.4	94.1	88.6	94.1	88.2	94	88.2
b11	94.3	89.6	94	88.8	94.4	88.5	93.4	87.8	93.7	87.8
b12	96.3	91.6	95.9	91.6	96.5	91.7	96.1	91.9	96.2	91.8
b13	96.2	91.6	96.2	91.6	96.2	91.5	96	91.6	95.2	90.6
b14	95.4	88.1	96.2	88.9	96.2	89.8	96	89	96.1	89.4
b15	96.1	88.9	95.9	88.4	96.3	89.5	96.3	89.4	95.9	89
c1	95.5	91.7	95	91	95.2	91.5	94.4	91.6	94.8	91.7
c1.5	91.6	88.9	91.9	89.3	91.6	89.6	90.1	88.8	91	89.3
c2	95.1	91.2	94.6	90.3	95.6	91.8	94.2	90.7	95	91.3
c2.5	92.7	88.7	92.9	88.8	92.8	89	92	89.1	92.2	89.2
c3	94.6	90.4	95.5	91.5	95.8	92.1	94.2	91	95	91.8
c3.5	92.5	88.6	93	88.7	92.1	88	91.4	88.2	91.8	88.3
c4	96.3	88.7	96.5	88.5	96.2	88.7	96.4	89.1	96.3	88.8
c5	96.3	88	96.4	88.7	96.1	88.8	96.2	88.9	96.4	89
c5.5	90.6	87.3	90.6	87.6	90.2	88.1	89.2	86.7	89.8	88
c6	95.5	87.5	95.5	87.3	96.4	89.1	95.3	87.7	95.5	88.2
c6.5	90.7	87.1	90.7	86.7	90.4	87.6	90.1	87.9	90	87.9
c7	95.9	87.9	96.2	88.5	95.9	88.6	95.9	88.7	96.1	88.9
c7.5	90.9	87	90	86.6	89.7	87.9	89.1	86.3	89.5	87.1
c8	91.4	87.7	90.1	85.6	92.6	87.3	91.5	86.3	91.2	86.1
c9	94.8	90.7	93.4	87.9	95.5	91.5	93.2	90.3	94.4	91.3
c9.5	90.3	87	89.6	85.1	90.2	87.5	89.7	87.4	90.2	88.1
c10	94.4	90.3	94.9	90.8	94.7	89.9	94.7	91.5	94.3	91.1
c10.5	90.9	88.3	91.1	88.4	90.9	88.9	90.2	88.6	90.5	88.7
c11	95	91	95.5	91.4	92.8	89.4	93.3	90.3	94.9	91.4
c11.5	87.8	82.3	89	85.3	90.2	87.1	90.1	88.6	90	87.8
c12	94.7	91	95.1	91.2	94.9	91.4	94	91.2	94.2	91

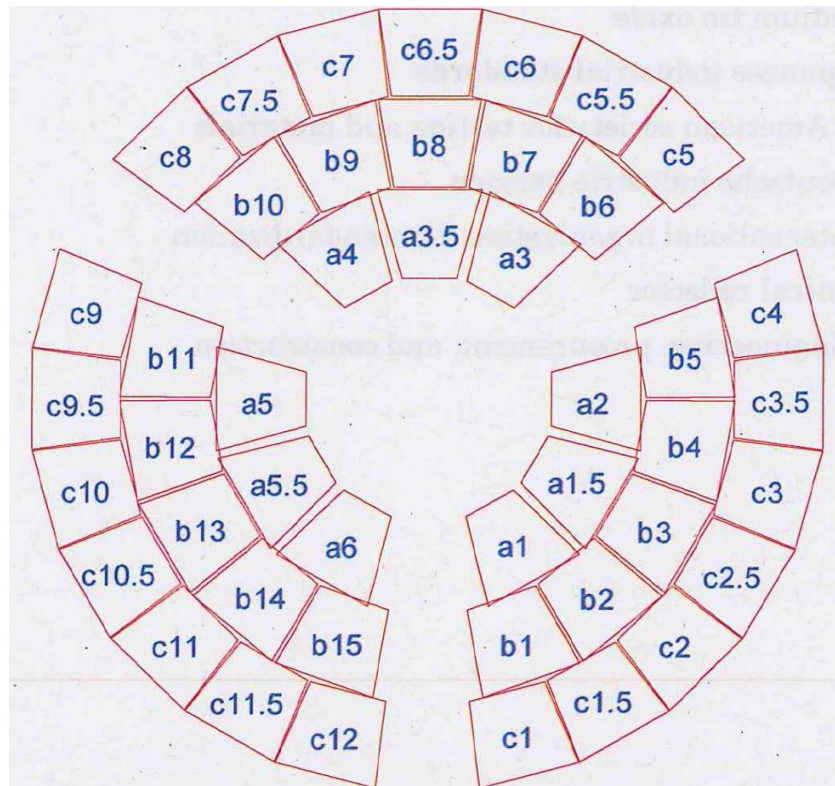


Figure 65. Central reflector identification numbers. Non-integer facets are the inactive facets for which there is currently no heliostat

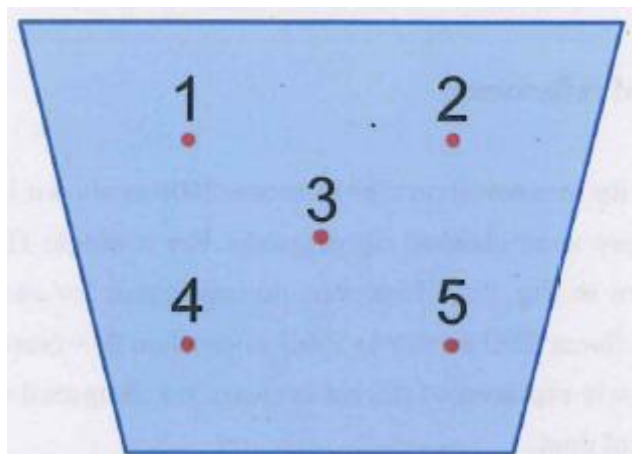


Figure 66. CR facet reflectance measurement positions

Table 20. Reflectivity of HS at two incidence angles

	20°	60°
A1	67.9	52.4
A2	78.2	61
A3	80.7	64.4
A4	72.4	56.4
A5	78.6	62.2

A6	72	56.1
B1	74.9	59.2
B2	70.7	55.6
B3	74.8	58.2
B4	73.8	57.8
B5	78.6	62.6
B6	78.7	62.6
B7	73.8	57.4
B8	73.4	56.9
B9	72.8	56.9
B10	75.8	59.3
B11	80.1	63.7
B12	80.3	64
B13	79.8	63.7
B14	70	54.6
B15	69.2	54.2
C1	72.5	57
C2	70.5	54.8
C3	70.8	55.2
C4	80.1	64
C5	80	63.7
C6	72.8	56.5
C7	76.1	59.5
C8	73.3	57
C9	78.1	62.2
C10	79.9	63.5
C11	74.6	58.3
C12	71.9	56.1

Incident angle was calculated using equation 31, *projected area* is calculated using equation 19.

$$\text{Incident angle} = \cos^{-1}(\text{projected area}) \quad (31)$$

Figure 67 shows HS mirror incident angle for all hours of daylight in each of the 12months using dates listed in Table 2. Note that 90 percent of the HS mirror incident angle is from 8.63 to 57.37 degree.

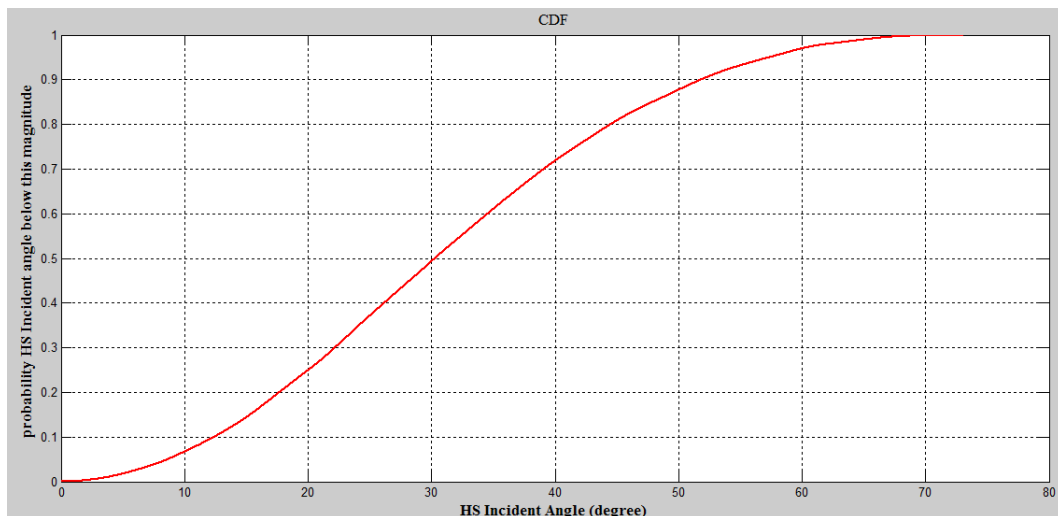


Figure 67 HS mirror Incident angle of BDOE for entire year (N = 221364)

TracePro Reflective Property Definition:

In TracePro, reflectivity can be defined as a function of incident angle, for example HSmirror and CRmirror properties are shown in Figure 68. Figure 69 shows response of HS mirror property uses linear interpolation.

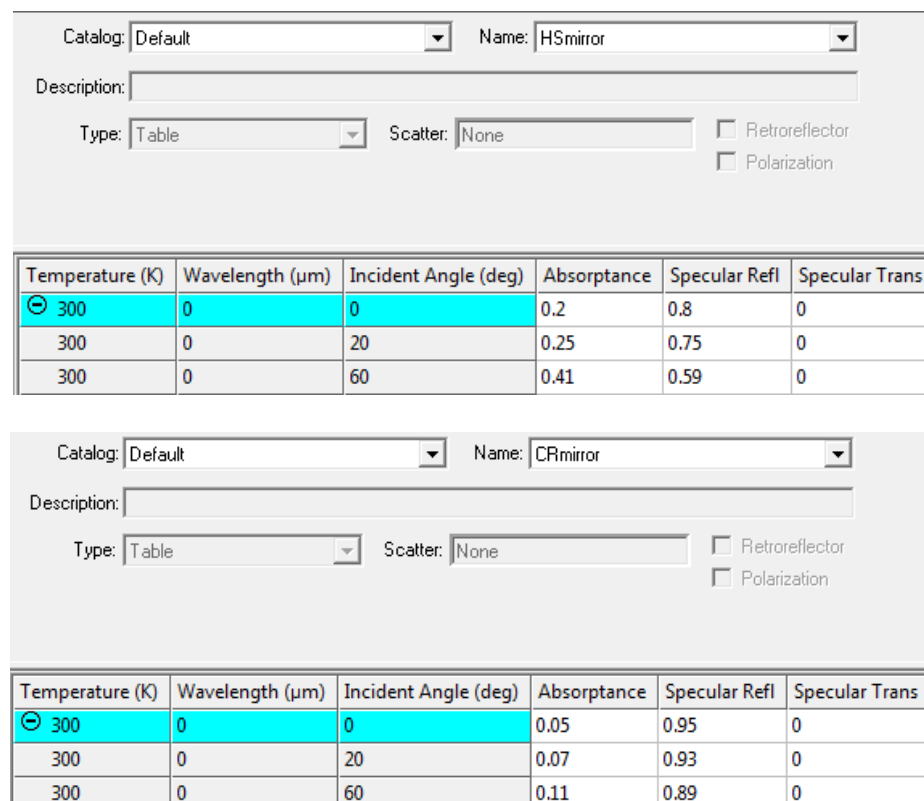


Figure 68 HS and CR mirror reflectance definition example

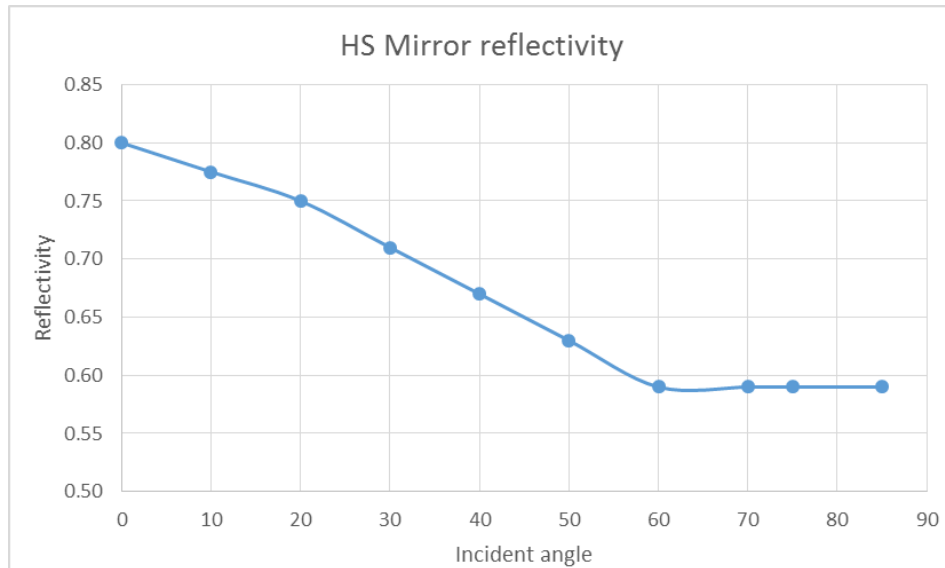


Figure 69 TracePro response to HSmirror reflectivity property¹⁴

Although above property is used for generating Figure 33's HS mirror reflectivity, we are aware that it's rather simple and pessimistic model. Reflectivity can be modeled more rigorously using the following:

In reality heliostat mirror is made of back silver glass, which can also be modeled in TracePro more realistically.

For example: Glass Schott B270 property shown in Figure 70.

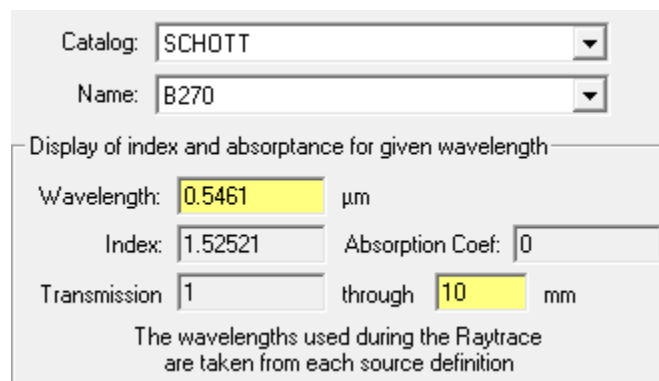


Figure 70 SCHOTT B270 optical property

¹⁴ HS mirror reflectivity shown in Figure 33 uses Figure 69 reflective property definition.

Back silver property can be defined in TracePro more realistically as combination of specular reflectance and bidirectional reflectance distribution function. For example TracePro library has Figure 71 as Mirror in its catalog.

Temperature (K)	Wavelength (μm)	Incident Angle (deg)	Absorptance	Specular Refl	Specular Trans
0	0	0	0.05	0.948675946342446	0
	Integrated BRDF	BRDF A	BRDF B	BRDF g	Integrated BTDF
	0.00132405365755438	0.0001	0.015	2	0
					BTDF A
					BTDF B
					BTDF g

Figure 71 back silver reflectivity example

By combining SCHOTT B270 glass and back silvering, Figure 72 shows TracePro reflectivity response with respect to incident angle. This is just to show the methodology to model complex reflectivity property. Further work is required to calibrate the reflectivity property definition by better measurements of HS facet reflectances.

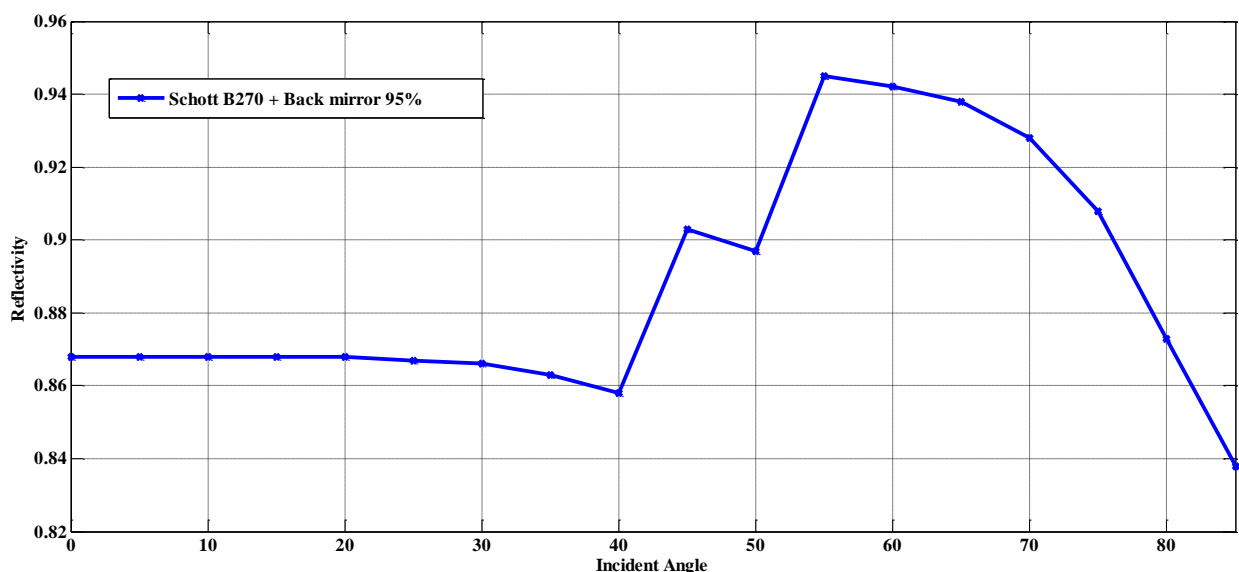
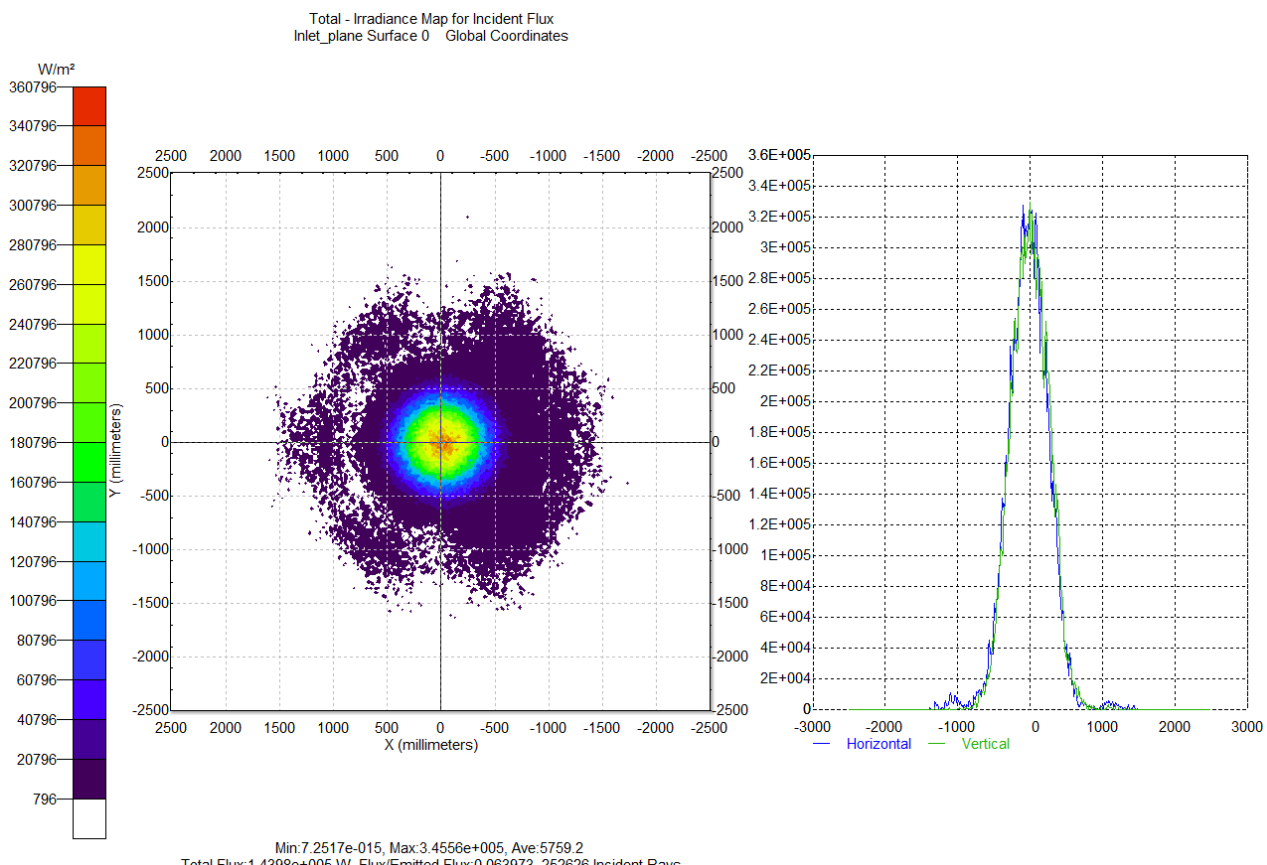


Figure 72 Reflectivity response in Tracepro of Schott B270 + back silver 95%

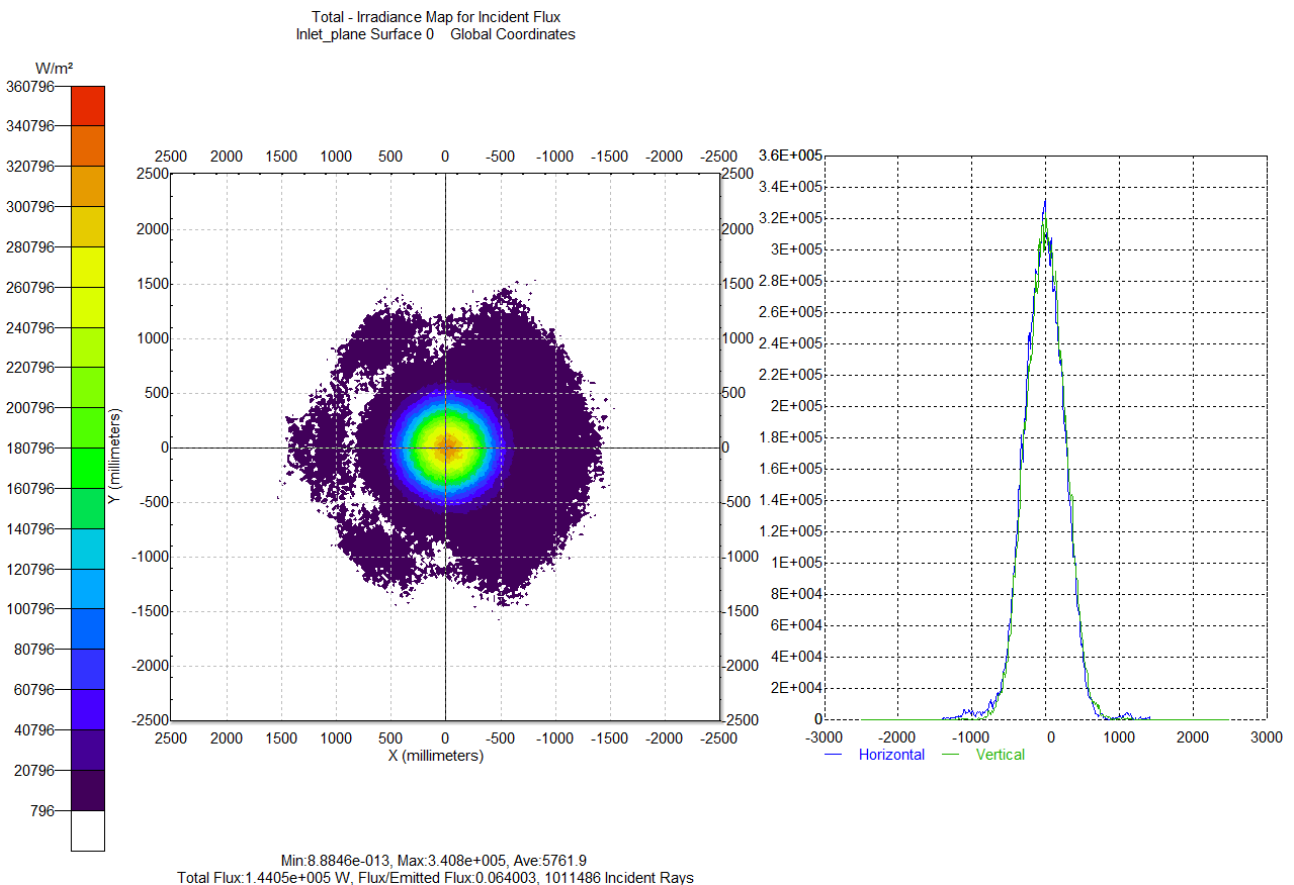
APPENDIX D

Raytrace-number of rays

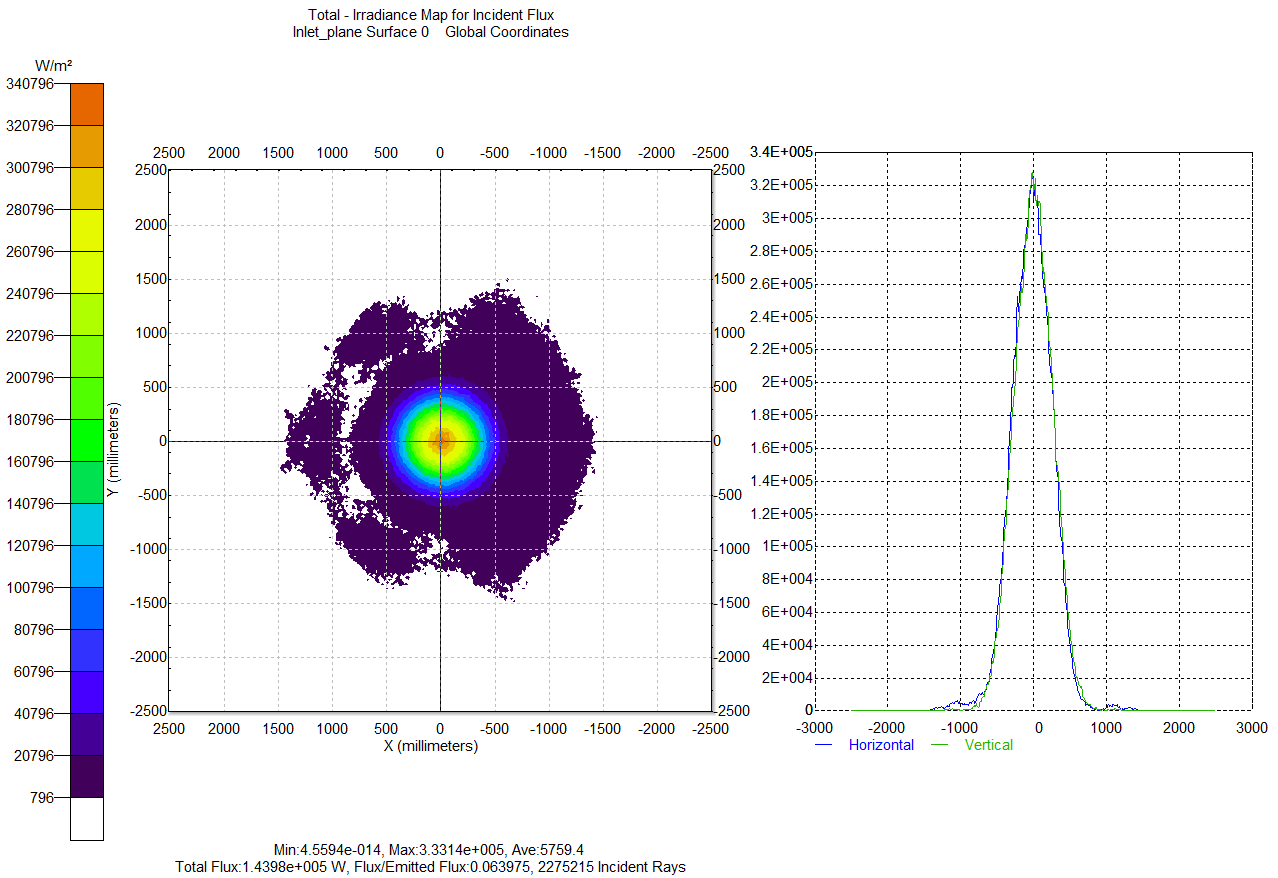
TracePro is a ray tracing software package [21] which performs Monte Carlo ray tracing. By definition, ray tracing introduces noise which translates to uncertainty of results. One way to reduce noise is to trace a very large number of rays. To estimate the effect of noise we simulate a representative BDOE configuration and sun position with different numbers of rays. Target height is kept at 6m, time is 21/06/2011 12:24:04 PM, UTC=+4hr (Solar Time 12 PM) and heliostat and CR canting errors are zero.



No of rays in target plane is 252626, total flux 143.9 kW, max flux=345.56 kW/m²
Figure 73 Flux distribution in target plane at 6m height with full BDOE (3 million rays)



No of rays in target plane is 1011486, total flux 144.05 kW,max flux=340.08 kW/m²
Figure 74 Flux distribution in target plane at 6m height with full BDOE (12 million rays)



No of rays in target plane is 2275215, total flux 143.98 kW, max flux=333.14 kW/m²
Figure 75 Flux distribution in target plane at 6m height with full BDOE (27 million rays)

Figure 73, Figure 74 and Figure 75 show that maximum flux at 6 m target plane is reduced by 3.59% while changing number of rays traced from 3 to 27 million. Left irradiance maps show that peak flux density is reduced as the number of rays is increased. Right profile graphs show that by increasing the number of rays the noise level is reduced. For optimization purposes 3 million rays are sufficient, but not for every case e.g. assessment of hot spots might require more rays.

APPENDIX E

Thermal Loss Model

The overall heat loss coefficient U_L is an important parameter in determining the performance of the solar receiver, this section formulates the equations needed to evaluate it. There are three main loss mechanisms associated with the receiver of a concentrated solar plant: convective loss, radiative loss, and conductive loss. A simple thermal loss model was employed to estimate heat loss within 10-20%.

In the following analysis a receiver temperature 600°C (873K) was assumed (for molten salt at 550°C (823K)). The absorptivity of the receiver in the solar spectrum was assumed to be $\alpha_s = 95\%$ and the long wave emissivity, $\epsilon = 0.1$. The molten salt emissivity was unknown. Therefore, 90% and 10% cases were considered in the calculations.

Forced Convection from the receiver surface may be estimated using Nusselt number correlations for horizontal plates according to the magnitude of Reynolds number, Re_L , and Prandtl number, Pr . Pr for air = 0.69 and $Re_L = u_e L / \nu$, where u_e is the wind speed in m/s, L is the characteristic length of the exposed hot surface (receiver diameter) in m and ν is the kinematic viscosity of air = 16.1×10^{-6} m²/s and all fluid properties were calculated at an average temperature of 700 K. The average forced convection Nusselt number on the receiver surface, \overline{Nu}_{forced} , can be found as follows [37]:

$$\overline{Nu}_{forced} = 0.664 Re_L^{\frac{1}{2}} Pr^{\frac{1}{3}}; 10^3 < Re_L \leq 5 \times 10^5; Pr > 0.5 \quad (32)$$

Natural Convection can be significant at large temperature differences. Therefore, a mixed flow regime is expected. The Grashof number is given by [37]:

$$Gr_L = \frac{\beta \Delta T g L^3}{\nu^2} \quad (33)$$

where ΔT is the temperature difference between the MPT (salt surface T) and the ambient fluid (ambient air) in K, g is the gravitational acceleration in m/s², and ν is the kinematic viscosity of the fluid in m²/s.

The Nusselt number for laminar and turbulent flows are given by [37]:

$$\overline{Nu}_{natural} = 0.54 (Gr_L Pr)^{1/4}, \quad 10^5 < (Gr_L Pr) < 2 \times 10^7 \text{ Laminar} \quad (34)$$

$$\overline{Nu}_{natural} = 0.14 (Gr_L Pr)^{1/3}, 2 \times 10^7 < (Gr_L Pr) < 3 \times 10^{10} \text{ Turbulent} \quad (35)$$

For mixed convection, natural and forced convection Nusselt numbers are combined using [37]:

$$\overline{Nu}^{7/2} = \overline{Nu}_{forced}^{7/2} + \overline{Nu}_{natural}^{7/2} \quad (36)$$

The convection heat transfer coefficient (in W/m²K) is given by $\bar{h}_c = \frac{k \overline{Nu}}{L}$, where k is the conductivity of air = 0.02705 W/m K at 313 K and 1 atmospheric pressure.

Radiative heat loss is given by the following equation:

$$\dot{Q}_{rad} = A \epsilon \sigma (T_{mp}^4 - T_{sky}^4) \quad (37)$$

Where \dot{Q}_{rad} is the radiative heat loss in W, T_{mp} is the MPT in K and T_{sky} is the effective sky temperature in K. Hence the radiative heat transfer coefficient relative to air temperature is given by:

$$h_r = \frac{\dot{Q}_{rad}/A}{(T_{mp} - T_{sky})} = \epsilon\sigma(T_{mp}^2 + T_{sky}^2)(T_{mp} + T_{sky}) \quad (38)$$

Conductive losses are assumed to be negligible, and the conduction loss coefficient would not be changing with L in any case.

Hence the overall heat loss coefficient is given by:

$$U_L = h_r + h_c \quad (39)$$

Bibliography

- [1] M. Kaltschmitt, W. Streicher, and a. Wiese, *Renewable Energy: Technology, Economics and Environment*. New York: Springer, 2007.
- [2] H. Lund, “Renewable energy strategies for sustainable development,” *Energy*, vol. 32, no. 6, pp. 912–919, 2007.
- [3] A. Gil, M. Medrano, I. Martorell, A. Lázaro, P. Dolado, B. Zalba, and L. F. Cabeza, “State of the art on high temperature thermal energy storage for power generation. Part 1 - Concepts, materials and modellization,” *Renew. Sustain. Energy Rev.*, vol. 14, no. 1, pp. 31–55, 2010.
- [4] O. Goebel, “Shams One 100 MW CSP Plant in Abu Dhabi - Update on Project Status,” *SolarPaces Conf.*, pp. 1–5, 2010.
- [5] L. Sargent, “Assessment of Parabolic Trough and Power Tower Solar Technology Cost and Performance Forecasts Assessment of Parabolic Trough and Power Tower Solar Technology Cost and Performance Forecasts,” *Rep. No. NREL/SR-550-34440*, p. 47, 2003.
- [6] Janet L. Sawin, *Ren 21, Renewable 2014 Global Status Report*. Paris, France: REN21 Secretariat, 2014.
- [7] T. R. Mancini, J. a. Gary, G. J. Kolb, and C. K. Ho, “Power Tower Technology Roadmap and Cost Reduction Plan.,” SAND2011-2419, 2011.
- [8] Y. Tamura, H. Kaneko, H. Hasuike, H. Wada, M. Yuasa, and S. Abu-Zaid, “Demonstration Experiment on 100kW Pilot Plant of Tokyo Tech Beam-Down Solar Concentration System,” *Proc. 15th Int. Symp. Conc. Sol. Power Chem. Energy Technol.*, pp. 1–7, 2009.
- [9] A. Segal and M. Epstein, “The optics of the solar tower reflector,” *Sol. Energy*, vol. 69, pp. 229–241, 2001.
- [10] A. Segal and M. Epstein, “Comparative Performances of ‘Tower-Top’ and ‘Tower-Reflector’ Central Solar Receivers,” *Sol. Energy*, vol. 65, no. 4, pp. 207–226, 1999.

- [11] A. Rabl, “Tower reflector for solar power plant,” *Sol. Energy*, vol. 18, no. 3, pp. 269–271, 1976.
- [12] A. H. Slocum, D. S. Codd, J. Buongiorno, C. Forsberg, T. McKrell, J. C. Nave, C. N. Papanicolas, A. Ghobeity, C. J. Noone, S. Passerini, F. Rojas, and A. Mitsos, “Concentrated solar power on demand,” *Sol. Energy*, vol. 85, no. 7, pp. 1519–1529, 2011.
- [13] W. T. Welford, *High Collection Nonimaging Optics*. Academic Press, Inc, 1989.
- [14] A. Segal and M. Epstein, “Practical Considerations in Designing Large Scale ‘Beam Down’ Optical Systems,” *J. Sol. Energy Eng.*, vol. 130, no. February, p. 011009, 2008.
- [15] A. Segal and M. Epstein, “Solar ground reformer,” *Sol. Energy*, vol. 75, pp. 479–490, 2003.
- [16] H. Hasuike, Y. Yoshizawa, A. Suzuki, and Y. Tamaura, “Study on design of molten salt solar receivers for beam-down solar concentrator,” *Sol. Energy*, vol. 80, pp. 1255–1262, 2006.
- [17] MES, “Heliostat Assembly Drawing.” MES, 2008.
- [18] M. Mokhtar, S. a. Meyers, P. R. Armstrong, and M. Chiesa, “Performance of a 100 kW th Concentrated Solar Beam-Down Optical Experiment,” *J. Sol. Energy Eng.*, vol. 136, p. 041007, 2014.
- [19] R. Buck and E. Teufel, “Comparison and Optimization of Heliostat Canting Methods,” *J. Sol. Energy Eng.*, vol. 131, no. February, p. 011001, 2009.
- [20] W. Contributors, “TracePro,” *Wikipedia, The Free Encyclopedia*. [Online]. Available: <https://en.wikipedia.org/w/index.php?title=TracePro&oldid=598896485>. [Accessed: 13-Jul-2015].
- [21] R. Dovesi, V. R. Saunders, C. Roetti, R. Orlando, F. Pascale, B. Civalleri, K. Doll, N. M. Harrison, I. J. Bush, P. D. Arco, M. Llunel, and M. Caus, *TracePro75 User’s Manual*. Lambda Research Corporation, 2014.
- [22] T. Wendelin, “SolTRACE: A New Optical Modeling Tool for Concentrating Solar Optics,” NREL/TP-5500-59163, 2003.
- [23] W. Contributors, “Scheme (programming language),” *Wikipedia, The Free Encyclopedia*. [Online]. Available: [https://en.wikipedia.org/w/index.php?title=Scheme_\(programming_language\)&oldid=671525247](https://en.wikipedia.org/w/index.php?title=Scheme_(programming_language)&oldid=671525247). [Accessed: 14-Jul-2015].
- [24] J. A. Duffie and W. A. Beckman, *Solar Engineering of Thermal Processes*. 2013.

- [25] I. Reda and A. Andreas, “Solar position algorithm for solar radiation applications,” *Sol. Energy*, vol. 76, pp. 577–589, 2004.
- [26] R. E. Fischer, B. Tadic-Galeb, and P. R. Yoder, *Optical System Design*. McGraw-Hill, 2008.
- [27] I. Reda and A. Andreas, “Solar position algorithm for solar radiation applications,” *Sol. Energy*, vol. 76, no. 5, pp. 577–589, 2004.
- [28] M. B. Mokhtar, “The Beam-Down Solar Thermal Concentrator : Experimental Characterization and Modeling,” Abu Dhabi, 2011.
- [29] A. Rabl, *Active Solar Collectors and Their Applications*. Oxford University Press, 1985.
- [30] A. Segal and M. Epstein, “Optimized working temperatures of a solar central receiver,” *Sol. Energy*, vol. 75, pp. 503–510, 2003.
- [31] J. J. O’Gallagher, *Nonimaging Optics in Solar Energy: Synthesis Lectures on Energy and the Environment: Technology, Science, and Society*. Morgan & Claypool, 2008.
- [32] A. Rabl, “Comparison of solar concentrators,” *Sol. Energy*, vol. 18, pp. 93–111, 1976.
- [33] D. Jenkins and R. Winston, “Integral design method for nonimaging concentrators,” *J. Opt. Soc. Am. A*, vol. 13, no. 10, p. 2106, 1996.
- [34] A. Parretta and A. Antonini, “Optics of Solar Concentrators . Part II : Models of Light Collection of 3D-CPCs under Direct and Collimated Beams,” vol. 3, no. 5, pp. 72–102, 2013.
- [35] A. Steinfeld, “Cone Compared to CPC as secondary concentrator in Tandem with a paraboloidal dish primary,” vol. 114, pp. 201–202, 1992.
- [36] MES, “Inspection Plan Beam Down Solar Concentration System,” HJR001, 2009.
- [37] A. F. Mills, *Heat Transfer*, 2nd ed. Prentice Hall, 2013.